

UNIVERSITI MALAYA

ORIGINAL LITERARY WORK DECLARATION

Name of Candidate: **Marlinda binti Ab Rahman (I.C/Passport No: 870522-29-5678)**

Registration/Matric No: **SGR100101**

Name of Degree: **Master of Science**

Title of Project ~~Paper/Research Report~~/Dissertation/Thesis ("this Work"):

**EFFICIENT PREPARATION OF GRAPHENE/ZINC OXIDE
NANOCOMPOSITES**

Field of Study: **Advanced Materials**

I do solemnly and sincerely declare that:

- (1) I am the sole author/writer of this Work;
- (2) This Work is original;
- (3) Any use of any work in which copyright exists was done by way of fair dealing and for permitted purposes and any excerpt or extract from, or reference to or reproduction of any copyright work has been disclosed expressly and sufficiently and the title of the Work and its authorship have been acknowledged in this Work;
- (4) I do not have any actual knowledge nor ought I reasonably to know that the making of this work constitutes an infringement of any copyright work;
- (5) I hereby assign all and every rights in the copyright to this Work to the University of Malaya ("UM"), who henceforth shall be owner of the copyright in this Work and that any reproduction or use in any form or by any means whatsoever is prohibited without the written consent of UM having been first had and obtained;
- (6) I am fully aware that if in the course of making this Work I have infringed any copyright whether intentionally or otherwise, I may be subject to legal action or any other action as may be determined by UM.

Candidate's Signature:

Date:

Subscribed and solemnly declared before,

Witness's Signature:

Date:

Name:

Designation:

ABSTRACT

In the present work, the objective is to prepare graphene-based nanocomposites which aimed at producing graphene in large scale with inorganic materials (zinc oxide, ZnO) homogeneously distributed on the graphene planes. The graphene/zinc oxide nanocomposites were efficiently prepared by a simple hydrothermal method. Two different types of graphene starting materials were used in the synthesis process: graphene oxide (GO) and functionalized graphene oxide (FGO). These two materials resulted in nanocomposite with different morphologies of ZnO decorated on graphene sheets.

The GO was prepared by simplified Hummer's method, followed by mixing with zinc seed precursor (zinc acetate dehydrate ($\text{Zn}(\text{CH}_3\text{COO})_2 \cdot 2\text{H}_2\text{O}$)) under reflux stirring method. The reduction of zinc oxide nanorod-like on the surface of GO sheets was finally obtained by hydrothermal method. The GO is heavily oxygenated graphene with carbonyl, hydroxyl and epoxy groups on the basal plane and also the carboxylic groups attached to the edges of carbon sheets. These functional groups served as an anchor and at the same time provided a suitable condition for the formation of ZnO nanorods attached to the surfaces and edges of the GO sheets. The graphene/ZnO nanoflower-like was prepared by using the same method by replacing GO with FGO. In this case, the FGO appeared as substrate for the in situ formation of nanoflower-like ZnO. The FGO also served as stabilizer and at once reacted as reducing agent for zinc oxide nanoflower under alkaline medium.

These results indicate that the graphene starting materials served as an important controlling factor for the morphology of ZnO decorated on graphene surface.

ABSTRAK

Dalam kajian ini, objektif adalah untuk menyediakan *graphene* berasaskan nano-komposit yang bertujuan untuk menghasilkan *graphene* dalam skala yang besar dengan bahan organik (zink oksida, ZnO) secara seragam terbentuk pada lembaran *graphene*. Nano-komposit zink oksida/*graphene* disediakan dengan efisien menggunakan kaedah hidroterma mudah. Dua jenis bahan asas yang berlainan telah digunakan dalam proses sintesis *graphene* iaitu *graphene* oksida (GO) dan *functionalized graphene* oksida (FGO). Bahan-bahan ini menghasilkan nano-komposit ZnO dengan morfologi yang berbeza di atas permukaan *graphene*.

GO telah disediakan menggunakan kaedah Hummer yang telah dipermudahkan, kemudian dicampurkan dengan zink asetat dihidrat ($\text{Zn}(\text{CH}_3\text{COO})_2 \cdot 2\text{H}_2\text{O}$) menggunakan kaedah refluks. Pembentukan zink oksida seperti nanorod pada permukaan GO akhirnya diperoleh melalui kaedah hidroterma. GO mengandungi banyak oksigen *graphene* dengan kumpulan karbonil, hidroksil dan epoksi pada satah basal dan juga kumpulan karboksilik pada tepi lembaran karbon. Kumpulan berfungsi ini sebagai pengikat dan pada masa yang sama menyediakan satu keadaan yang sesuai untuk pembentukan ZnO nanorods di atas permukaan dan tepi lembaran GO. *Graphene* / ZnO nano-*flower* telah disediakan dengan menggunakan kaedah yang sama dengan menggantikan GO dengan FGO. Dalam kajian ini, FGO digunakan sebagai substrat dalam pembentukan situ ZnO nano-*flower* dan sebagai penstabil, sekali gus bertindak balas sebagai ejen penurunan untuk zink oksida nano-*flower* dalam medium beralkali. Keputusan ini menunjukkan bahawa bahan asas iaitu *graphene* menjadi faktor yang sangat penting bagi mengawal morfologi ZnO yang terbentuk pada permukaan *graphene*.

ACKNOWLEDGMENT

I am grateful to Allah, our Lord and Cherisher for granting me chance and the ability to successfully complete this dissertation. Indeed, without His Help and Will, nothing is accomplished.

First and foremost, I would like to express my sincere thanks to my beloved parents, Mr. Ab Rahman Mohamad and Umi Kethom Abd Rahman, and also my families, especially to Mdm. Mardianah Ab Rahman for their supportive, understanding and unconditional love within my studies. I could not get to where I stand now without their support.

I would like to express my deepest gratitude to my supervisor, Dr. Huang Nay Ming for his continuous support, encouragement and also guidance of this research. My thanks go to my co-supervisor Prof. Dato' Dr. Muhamad Rasat Muhamad who led me towards an exciting area of research study. I am also grateful to my head department, Prof. Datin Dr. Saadah Abdul Rahman for providing me opportunities during my studies at department of physics, University of Malaya.

Special thanks go to my colleagues, lab members and staff at Low Dimensional Material Research Centre (LDMRC), Department of Physics, who helped me throughout my research and study at University of Malaya. Many thanks go to Dr. Vijay Kumar Shankarayya Wadi for his helpful discussion and my colleagues, Miss Betty Chang Yea Sze, Mdm. Norazriena Yusoff, Mdm. Mazlinda Zainy, Miss Fadilah Abd Wahab and Mr. An'amt Mohd Nor for helping and assisting me in my experiments since the first time I am in solid state laboratory.

I wish to express my sincere thanks to staff at Department of Engineering, Nottingham University who helped me run FESEM test for my samples. Many thanks go to staff at Chemist Department, University of Malaya for assisting me run UV-visible test for my samples.

Finally, I am gratefully to acknowledge the financial support and laboratory facilities from High Impact Research Grant (UM.C/625/1/HIR/030) from the University of Malaya, the High Impact Research Grant (UM.C/625/1/HIR/MOHE/05) from the Ministry of Higher Education Malaysia, and the Postgraduate Research Grant (UM.C/241/9) from the University of Malaya. Moreover, I would like to convey thanks to Ministry of Higher Education Malaysia for providing me with MyMaster fund.

LIST OF PUBLICATIONS

1. **Marlinda, A. R.**, Huang, N. M., Muhamad, M. R., An'amt, M. N., Chang, B. Y. S., Yusoff, N., et al. (2012). Highly efficient preparation of ZnO nanorods decorated reduced graphene oxide nanocomposites. *Materials Letters*, 80(0), 9-12.
2. Chang, B. Y. S., Huang, N. M., An'amt, M. N., **Marlinda, A. R.**, Norazriena Y., Muhamad M. R., et al. (2012). Facile hydrothermal preparation of titanium dioxide decorated reduced graphene oxide nanocomposite. *International Journal of Nanomedicine*, 7(1), 3379-3387.
3. Viay Kumar, S., Huang, N. M., Lim, H. N., **Marlinda, A.R.**, Harrison, I., & Chia, C. H. (2013). One-step size-controlled synthesis of functional graphene oxide/silver nanocomposites at room temperature. *Chemical Engineering Journal*, 219(0), 217-224.

TABLE OF CONTENTS

<u>CONTENT</u>	<u>PAGE</u>
ORIGINAL LITERARY WORK DECLARATION	ii
ABSTRACT	iii
ABSTRAK	v
ACKNOWLEDGEMENT	v
LIST OF PUBLICATIONS	vii
TABLE OF CONTENTS	viii
LIST OF TABLES	xii
LIST OF FIGURES	xiii
LIST OF ABBREVIATIONS	xvii
 CHAPTER 1: INTRODUCTIONS	
1.1 Introduction to carbon materials	1
1.2 Crystal structure of Graphene and Graphite	4
<i>1.2.1 Structure of graphene's honeycomb lattice</i>	4
<i>1.2.2 Structure of graphite- graphene stacking</i>	5
1.3 Preparation of Graphene	5
<i>1.3.1 Top – Down Approach: Micromechanical cleavage</i>	5
<i>1.3.2 Bottom – Up Approach: Growing Graphene on SiC</i>	6
1.4 Motivation/goal of the research	6
1.5 Scope of dissertation	7

CHAPTER 2: LITERATURE REVIEW

2.1 Properties of zinc oxide (ZnO)	9
2.2 Properties of Graphene	10
2.3 Graphene synthesis	12
2.4 Graphene-based composite material synthesis	17
2.5 Hydrothermal method	20

CHAPTER 3: EXPERIMENTAL METHODS

3.1 Introduction	22
3.2 Materials	23
3.2 Sample preparation	23
3.2.1 <i>Synthesis of graphene oxide (GO)</i>	25
3.2.2 <i>Synthesis of functionalized graphene oxide (FGO)</i>	28
3.2.3 <i>Preparation of nanorod-like reduced Graphene/Zinc Oxide (rG/ZnO) nanocomposite</i>	30
3.2.4 <i>Preparation of flower-like reduced Functionalized Graphene/Zinc Oxide (rFG/ZnO) nanocomposite</i>	32
3.3 Characterizations and Analytical procedures	33
3.3.1 <i>Phase and crystalline structures via X-ray Diffraction (XRD)</i>	34
3.3.2 <i>High resolution surface images obtained by using Field emission scanning electron microscopy (FESEM)</i>	37
3.3.3 <i>High resolution transmission electron microscope (HRTEM)</i>	38
3.3.4 <i>Composition obtained by X-ray Photoelectron spectroscopy (XPS)</i>	41
3.3.5 <i>Structural characteristics determined by Raman spectroscopy</i>	43
3.3.6 <i>Optical absorption properties by Ultra violet visible spectroscopy (UV-vis)</i>	48

3.3.7 Photoluminescence spectroscopy (PL)	50
3.3.8 Thermal behavior properties determined by Thermogravimetric analysis (TGA)	53
CHAPTER 4: RESULTS AND DISCUSSIONS	
4.1 Introduction and Overview	57
4.2 Nanorod-like Graphene/zinc Oxide Nanocomposite	58
4.2.1 Field emission scanning electron microscope (FESEM)	58
4.2.2 High Resolution Transmission Electron Microscope (HRTEM)	59
4.2.3 X-ray diffraction (XRD)	62
4.2.4 Ultraviolet-Visible Spectroscopy (UV-vis)	64
4.2.5 Thermogravimetric analysis (TGA)	66
4.2.6 Mechanism for the synthesis process of nanorod-like graphene/ZnO nanocomposite (G/ZnO)	68
4.3 Flower-like functionalized graphene/zinc oxide (FG/ZnO) nanocomposite	70
4.3.1 Parameter	70
4.3.2 Experiment results	71
4.3.2.1 X-Ray Diffractometer (XRD)	72
4.3.2.2 X-Ray Photoelectron Spectra (XPS)	73
4.3.2.3 Field Emission Scanning Electron Microscope (FESEM)	76
4.3.2.4 Transmission Electron Microscope (TEM)	81
4.3.2.5 High Resolution Transmission Electron Microscope (HRTEM)	82
4.3.2.6 Raman Spectroscopy	84
4.3.2.7 Fourier transform infrared spectroscopy (FTIR)	85
4.3.2.8 Ultraviolet visible spectroscopy	86

<i>4.3.2.9 Photoluminescence spectra</i>	89
<i>4.3.3 Mechanism for the synthesis of functionalized graphene oxide (FGO)</i>	90
<i>4.3.4 Mechanism for the synthesis of nanoflower-like functionalized graphene/ZnO nanocomposite (FG/ZnO)</i>	92
CHAPTER 5: CONCLUSION AND SUGGESTIONS FOR FUTURE RESEARCH	
5.1 Conclusion	94
5.2 Suggestions for future research	96
REFERENCES	97

LIST OF TABLES

<u>Table caption</u>	<u>Page</u>
Table 3.1: Table displays the volume of GO and DI water needed to prepare GO solution at different concentration.	30
Table 3.2: Table displays the constant parameters for synthesis of the graphene/zinc oxide nanocomposites.	31

LIST OF FIGURES

<u>Figure caption</u>	<u>Page</u>
Figure 1.1: Graphitic allotrope structure of 0D-fullerenes (a), 1D-carbon (b), 2D-graphene (c) and 3D-graphite (stacking of graphene layer) (d) (Castro Neto, 2006a).	1
Figure 1.2: TEM image of a graphene sheet illustrating the crystalline lattice (bond length ~0.14 nm) (Dato et al. 2009).	5
Figure 2.1: Figure show the electronic band structure of single-layer graphene (Rao, 2009)	12
Figure 2.2: Diagram representation of the timeline in the research of graphene with some relevant findings.	16
Figure 2.3: Diagram representation of the application based on graphene since it is first discovered.	19
Figure 3.1: Image of the autoclave.	24
Figure 3.2: Image of the synthesis process of GO via the simplified Hummers method (SHM).	26
Figure 3.3: The real image of Centrifuge CR21GIII; Hitachi, Japan.	27
Figure 3.4: Images of GO solution after washing processes.	28
Figure 3.5: Image of synthesis process to prepare FGO.	29
Figure 3.6: The synthesis process of graphene/ZnO nanocomposite by hydrothermal treatment.	32
Figure 3.7: Figure shows the angle of reflection is equal to the angle of incidence ("X-ray Diffraction,").	35
Figure 3.8: Real image of Philips D5000 X-Ray Diffractometer.	36

Figure 3.9: Real image of FEI Quanta 400F FESEM.	37
Figure 3.10: The schematic outline of TEM ("Basic principle of transmission electron microscope,").	39
Figure 3.11: Figure shows bright and dark strips deduced from HRTEM image.	41
Figure 3.12: The schematic principle of X-ray photoelectron spectroscopy ("Material Surface Analysis with X-Ray Photoelectron Spectroscopy (XPS)," May 10, 2011).	42
Figure 3.13: Rough schematic of XPS physics - "Photoelectric Effect. XPS spectral lines are identified by the shell from which the electron was ejected (1s, 2s, 2p, etc.) (Bvcrist., 10 June 2010).	43
Figure 3.14: Schematic diagram of Raman spectroscopy ("Technology Methods," 2011).	45
Figure 3.15: Energy level diagram show the states involved in Raman signal(Moxfyre, 18 September 2009).	46
Figure 3.16: Figure shows laser beams that were spotted on the top surface of sample.	47
Figure 3.17: Real image of Renishaw inVia Raman microscope.	47
Figure 3.18: Basic components of UV-visible spectroscopy.	48
Figure 3.19: The schematic diagram of device operation (Clark, 2006).	49
Figure 3.20: Real image of UltraViolet (UV-vis) spectroscopy (Evolution 300, Thermo Fisher Scientific, Pittsburgh, PA).	50
Figure 3.21: Typical experimental set-up for PL measurements ("Molecular Fluorescence Spectroscopy,").	52
Figure 3.22: Real image of Renishaw inVia PL microscope with laser excited at 325 nm.	53

Figure 3.23: The schematic principle of TGA measurement (Skoog).	54
Figure 3.24: TG curve of weight (%) versus temperature (°C).	55
Figure 4.1: FESEM micrographs of pure ZnO (a), and ZnO/rGO composites with different concentrations of GO by 0.2 mg/ml (b), 0.6 mg/ml (c) and 1.0 mg/ml (d).	58
Figure 4. 2: Images (a) and (b) show the rod-like shape of ZnO at different magnification.	60
Figure 4.3: HRTEM of rod-like graphene/ZnO-1.0 nanocomposite (a) and image of high magnification (b).	61
Figure 4.4: XRD patterns of graphite flake (a) and GO (b).	63
Figure 4.5: XRD pattern of pure ZnO (a), ZnO/graphene with 0.2 mg/ml GO (b), 0.6 mg/ml GO (c) and 1.0 mg/ml GO (d).	64
Figure 4.6: UV-vis spectra of GO and reduced GO after hydrothermal treatment.	65
Figure 4.7: UV-vis spectra of (a) pure ZnO and composites with different concentrations of GO at (b) 0.2 mg/ml, (c) 0.6 mg/ml and (d) 1.0 mg/ml.	66
Figure 4.8: TG curves of (a) pure ZnO, and composites with different concentrations of GO at (b) 0.2 mg/ml, (c) 0.6 mg/ml and (d) 1.0 mg/ml.	68
Figure 4.9: Schematic for the formation process of graphene/ZnO nanorod-like composite starting with GO in deionized water (a), after added zinc ions complex (b) and after hydrothermal treatment (c).	69
Figure 4.10: Figure shows the FG (a), star-like ZnO (b) and FG/ZnO-1.0 nanocomposite that dispersed in the deionized water straight away after hydrothermal treatment.	71
Figure 4.11: XRD patterns of FGO (a), ZnO (b) and FG/ZnO-1.0 nanocomposite (c).	73

Figure 4.12: Figure shows XPS of graphene oxide (GO) as-prepared by simplified Hummer's method.	74
Figure 4.13: XPS of functionalized graphene (FG) after hydrothermal treatment.	75
Figure 4.14: XPS of FG/ZnO-1.0 nanocomposite.	76
Figure 4.15 (a-d): FESEM images of ZnO synthesized at different pH values.	77
Figure 4.16: Figure shows the mapping analysis of pure needle-like ZnO at pH 9.	78
Figure 4.17 (a-d): FESEM images of nanoflower-like FG/ZnO-1.0 nanocomposite with 10 000 (a), 20 000 (b), 40 000 (c) and 80 000 (d) magnification power.	80
Figure 4.18: TEM images of FGO and rFG/ZnO-1.0 nanocomposite.	82
Figure 4.19: HRTEM image of flower-like FG/ZnO nanocomposite (a) and HRTEM of nanocomposite at higher magnification (b).	83
Figure 4.20: Raman spectra of FGO, FG, ZnO and nanocomposites.	84
Figure 4.21: FTIR of GO, FGO and FG samples.	86
Figure 4.22: UV-Vis spectra of FGO and FG after hydrothermal reduction.	87
Figure 4.23: UV-visible spectra of FGO, FG, pure ZnO and composites.	88
Figure 4.24: PL spectra of as-prepared samples under 325 nm UV irradiation: pure ZnO (a); FG/ZnO-1.0 flower-like nanocomposite (b).	89
Figure 4.25: Schematic for the preparation of functionalized graphene oxide (FGO).	91
Figure 4.26: Schematic for the preparation of the nanoflower-like functionalized graphene/ZnO nanocomposite.	92

LIST OF ABBREVIATIONS

GO	Graphene oxide
FGO	Functionalized graphene oxide
rGO	Reduced graphene oxide
FG	Functionalized graphene
CVD	Chemical vapor deposition
DIW	Deionized water
HSA	Hemispherical analyzer
XRD	X-ray diffraction
XPS	X-ray photoelectron spectroscopy
TEM	Transmission electron microscopy
TGA	Thermogravimetry analysis
PL	Photoluminescence
HRTEM	High resolution transmission electron microscopy
FESEM	Field emission scanning electron microscopy
UV-vis	Ultraviolet visible spectroscopy
UV	Ultraviolet
NRs	Nanorods
NWs	Nanowires
SLG	Single layer graphene
SHM	Simplified Hummers method
CCD	Charge-coupled device
PMT	Photomultiplier tube
T_i	Initial temperature
T_f	Final temperature
FETs	Field-effect transistors

CHAPTER 1

INTRODUCTION

1.1 Introduction to carbon materials

Carbon is the elementary constituent of graphene and graphite. It is arguably one of the most flexible and robust elements in the whole periodic table. It is the 6th element of the periodic table. Its atom is built from 6 protons, A neutrons, and 6 electrons, where $A = 6$ and 7 yield stable isotopes ^{12}C and ^{13}C , respectively, and $A = 8$ characterizes the radioactive isotope ^{14}C . It is responsible for all organic chemistry, and hence it presents in all living organisms on Earth, and it is also behind countless numbers of different chemical structures. Even in materials that are made out of pure carbon, one can find a plethora of crystalline structures: fullerenes or buckyballs, carbon nanotubes, graphite, diamond and graphene, which had become an interesting topic to study recently. All these materials can be characterized by their dimensionality and the nature of the chemical bonding (sp^2 or sp^3) that keeps the atoms together. The main motif behind these structures is the hexagonal benzene ring.

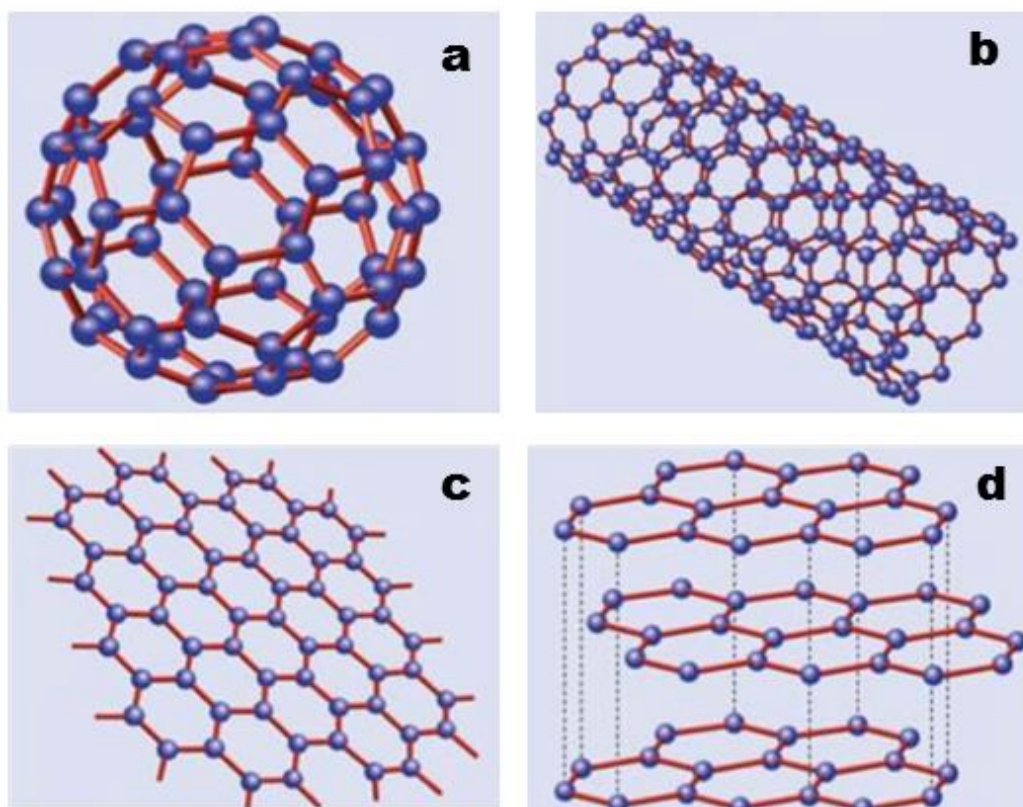


Figure 1.1: Graphitic allotrope structure of 0D-fullerenes (a), 1D-carbon (b), 2D-graphene (c) and 3D-graphite (stacking of graphene layer) (d) (Castro Neto, 2006a).

The 0D-Fullerenes are quasi-spherical molecules that can be obtained from graphene by adding pentagons to the hexagonal structure. Their radius depends on how many hexagons are replaced by pentagons. The 0D graphitic allotrope (fullerenes) has been discovered in 1985 by Robert Curl, Harold Kroto, and Richard Smalley (Kroto, Heath, O'Brien, Curl, & Smalley, 1985). Its most prominent representative is the C₆₀ molecule which has the appearance of a football and is also called “buckyball”. It consists of a graphene sheet, where some hexagons are replaced by pentagons, which cause a crumbling of the sheet and the final formation of a graphene sphere [Fig. 1.1(a)]. Its existence had been predicted before, in 1970, by the Japanese theoretician Eiji Ozawa (Osawa, Kroto, Fowler, & Wasserman, 1993).

The 1D-Carbon nanotubes are one-dimensional crystal that can be obtained by taking a graphene strip and rolling it along a certain direction. The discovery of carbon

nanotubes is most often attributed to Sumio Iijima and his 1991 publication in *Nature*. Recently, doubts about this attribution have been evoked because it seems that carbon nanotubes have a longer history in the community of material scientists. Indeed, a publication by the Soviet scientists Radushkevich and Lukyanovich in 1952 contained a transmission electron microscope image showing carbon nanotubes. Depending on the rolling direction, carbon nanotubes can be either metallic or insulating.

Graphene is a two-dimensional structure that is comprised of a regular hexagonal array of benzene rings (see Figure 1.1 (c)). Hence, graphene is a unique example of an atomically thin membrane. Like any other membrane, distortions of the two-dimensional structure in a three-dimensional renders better stability either thermodynamically or chemically, and hence graphene has a strong tendency to distort, forming scrolls, folds, blisters, wrinkles, creases, etc. However, when supported by a substrate or a scaffold a graphene crystal can be stabilized and its properties can be measured experimentally. From an experimental point of view, graphene is a new allotope and accessible to physical measurements only since 2004.

The graphene has received intense interest in the fields such as physics, chemistry, biology and materials science due to its exceptional electrical (large mobility of charge carriers, $200\,000\text{ cm}^2\text{V}^{-1}\text{s}^{-1}$), mechanical (Young's modulus of $\sim 1\text{TPa}$), thermal (thermal conductivity of $\sim 5000\text{ Wm}^{-1}\text{K}^{-1}$) and optical properties (transmittance $\sim 97\%$), as well as its unique two-dimensional (2D) structure and large surface area ($2630\text{ m}^2\text{g}^{-1}$). These excellent properties support graphene as an ideal building block in nanocomposites. In 2006, Ruoff's group reported the first graphene-based nanocomposite, a graphene-polystyrene nanocomposite, which has attracted tremendous attention and was followed by further development of a new class of graphene-based inorganic nanocomposites. Recently, graphene–inorganic nanocomposites have opened up an exciting new field in the science and technology of graphene.

The graphite is essentially a stack of graphene layers whose properties depend on the stacking order, that is, on the relative orientation of the graphene planes to each other. The interaction between the graphene layers is weak because the distance between the layers is large, and thus graphite can be easily cleaved. In fact, this is the reason why one can draw with a pencil. It was discovered in a mine near Borrowdale in Cumbria, England in the 16th century, and its use for marking and graphical purposes was almost immediately noticed. Indeed, the nearby farmers used graphite blocks from the mine for marking their sheep. Due to its softness and dark color, graphite was considered during a long time as some particular type of lead. The notion that graphite was formed from carbon atoms was discovered by the Swedish-German pharmacist Carl Wilhelm Scheele in the middle of the 18th century. But it was the German chemist Abraham Gottlob Werner in 1789 who coined the material by its current name “graphite”, thus emphasising its main use for graphical purposes. Graphite may be viewed as a stacking of graphene sheets [Figure 1.1 (d)] that stick together due to the van der Waals interaction, which is much weaker than the inplane covalent bonds. This physical property explains the graphic utility of the material: when one writes with a piece of graphite, i.e. when it is scratched over a sufficiently rough surface, such as a piece of paper, thin stacks of graphene sheets are exfoliated from bulk graphite and now stick to the surface. This is possible due to the above-mentioned weak van der Waals interaction between the graphene sheets.

1.2 Crystal structure of Graphene and Graphite

1.2.1 Structure of graphene’s honeycomb lattice

The carbon atoms in the graphene densely pack in a honeycomb lattice due to their sp^2 hybridisation. The TEM image shows the arrangement of carbon that illustrating the crystalline lattice.

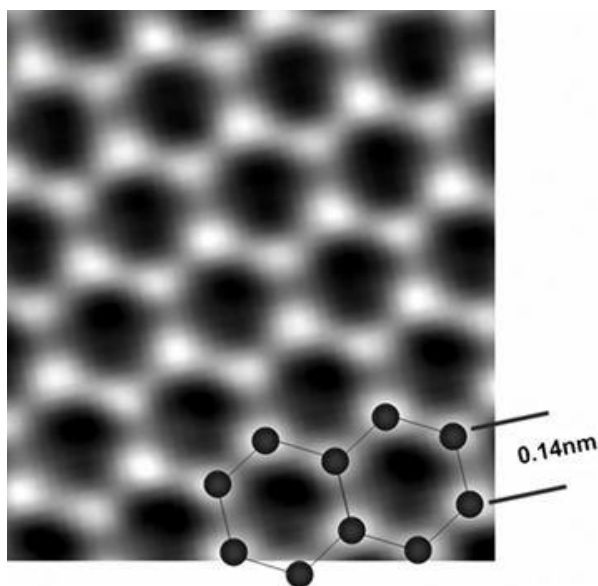


Figure 1.2: TEM image of a graphene sheet illustrating the crystalline lattice (bond length ~ 0.14 nm) (Dato et al. 2009).

1.2.2 Structure of graphite- graphene stacking

The graphite consists of stacked graphene layers. Each layer distinguishes crystal (ordered) graphite, with two different basic stacking orders, from turbostratic graphite with a certain amount of disorder in the stacking.

1.3 Preparation of Graphene

1.3.1 Top – Down Approach: Micromechanical cleavage

Graphene layers can be made by mechanical cleavage that highly oriented the flakes of graphite through a scotch tape method. This method was pioneered by Geim and Novoselov in 2004, it is an approach to fabricate the high quality single sheets of graphene (Geim & Novoselov, 2007). Later, Stankovich et al. proposed a method to produce graphene oxide from graphite oxide through sonication. It consists in the dispersing graphite oxide in liquid medium which is hydrazine hydrate solvent then it was sonicated (Stankovich et al., 2007; Watcharotone et al., 2007). Non exfoliated graphite is eventually isolated from graphene by centrifugation. Unfortunately, the

quality of graphene produced by this method is low compared to e.g. scotch-tape graphene due to incomplete removal of various functional groups by existing reduction methods.

1.3.2 Bottom – Up Approach: Growing Graphene on SiC

Another alternative of obtaining graphene had been developed by Atlanta group, led by Walt de Heer and Claire Berger (Berger et al., 2004; de Heer et al., 2007). It consists of exposing an epitaxially grown hexagonal (4H or 6H-) SiC crystal to high temperature ($>1100\text{ }^{\circ}\text{C}$) to reduce it to graphene. This process produces epitaxial graphene with dimensions dependent upon the size of the SiC substrate chosen. The surface of the SiC used for graphene formation, silicon- or carbon-terminated, highly influences the thickness, mobility and carrier density of the graphene produced. This method then contributed to the identification of the important of graphene properties and gave great interest to researchers engaged in further study for semiconductor industries. Vázquez de Parga et al. also reported the synthesis of single-layer graphene on a (0001) plane of ruthenium single crystal (Vázquez de Parga et al., 2008).

1.4 Motivation/goal of the research

This dissertation focuses on synthesis and characterizations of the graphene/ZnO as a nanocomposite. The first objective of the research is to investigate the effect of concentrations of graphene oxide as a starting material for the nanocomposite synthesis on the growth of rod-like ZnO nanoparticles that formed on the graphene sheets. Secondly, the research is conducted to investigate the optimum parameters for the nanocomposite synthesized. By using the optimum parameters obtained, the third objective is to synthesis the flower-like ZnO nanocomposites with the functionalized

graphene oxide as the starting material. The main objective of this research is to study the properties of the nanocomposites that formed.

The graphene/ZnO nanocomposites were synthesized by using a simple hydrothermal method. There are various characterization techniques were carried out to study the structure of these material such as Field Emission Scanning Electron Microscopy (FESEM) and X-ray Diffraction pattern (XRD). The compositions of element in the nanocomposites were ensured by using X-ray Photoelectron Spectroscopy (XPS). The atomic arrangement of the structure was performed by using the High Resolution Transmission Electron Microscopy (HRTEM). The optical properties of the nanocomposites were characterized through Ultraviolet Visible Spectroscopy (UV-Vis) and Photoluminescence (PL) Spectroscopy. Thermal stability of the nanocomposites was obtained by using Thermogravimetric Analysis (TGA).

1.5 Scope of dissertation

Chapter 2 provides background information of the dissertation and discusses the properties of ZnO and graphene materials. The previous works on the synthesis of nanocomposites are being discussed. The methodologies that were used to synthesis graphene based nanocomposite are covered in this chapter. The chosen method which is hydrothermal method briefly introduced in this chapter.

Chapter 3 presents the procedures used to prepare starting material by using simplified Hummers method. This chapter also provides the step to synthesis functionalized graphene oxide from the graphene oxide. Then, this part demonstrates the details of the synthesis process of graphene/ZnO nanocomposites with graphene oxide (GO) as starting material. It is followed by the synthesis of ions zinc complex and then the combination of graphene oxide and ions zinc complex in order to prepare graphene/ZnO nanocomposites. Then, the synthesis for the preparing nanocomposites

by using functionalized graphene oxide is explained. Here, the details of the simple hydrothermal method and its advantages are also explained in this chapter. This chapter also introduces the characterization tools and its basic working principle that was used during the course of current research.

Chapter 4 describes the results of the synthesis and their characteristics. The investigations of the structural, morphological and optical characteristics are reported in this chapter. The effect of using graphene oxide (GO) and functionalized graphene oxide (FGO) as the starting material are investigated in this chapter.

Chapter 5 provides a summary of the dissertation and concludes the objectives of this research. The objectives are successfully achieved and correlated with the results and discussions that had been presented in chapter 4. Thus, this chapter presents the general conclusion on the findings. At the end of this chapter, suggestions for future work are manifested.

CHAPTER 2

LITERATURE REVIEW

In this chapter, the background and special properties of zinc oxide, graphene and the techniques to synthesis graphene from graphite flakes since it was first discovered are described. Furthermore, the synthesis of graphene-based composite nanomaterial is also introduced in this chapter. Finally, a simple technique based on hydrothermal method is proposed to synthesis graphene and graphene/ZnO nanocomposites. Moreover, the advantages of hydrothermal method are explained at the end of this chapter.

2.1 Properties of Zinc oxide (ZnO)

ZnO is a promising transparent semiconductor material that has received a great attention due to its wide band gap (3.37 eV) and large excitation binding energy (60 meV). Due to the reason that wide band gap makes ZnO a potential material for photonic application in UV spectral range, while the high excitation of binding energy allows the ZnO become an efficient excitation emission at room temperature. In addition, ZnO is highly sensitive toward various type of gaseous such as acetylene, ethanol and carbon monoxide, this makes it practically suitable for sensing application. Moreover, ZnO is suitable for biomedical application since it is chemically stable and environmental friendly.

ZnO is nearly insoluble in water and alcohol. However, it acting as an amphoteric oxide, ZnO can be solved in (degraded by) not only most acids to give soluble salts but also bases to give soluble zincates. Although ZnO has the boiling point of 2360 °C, but ZnO decomposes into zinc vapor and oxygen at around 1975 °C.

Consequently, ZnO is a versatile material that has wide group of growth morphologies, it can be in the form of powders, thin films, single-crystal, nano-sized structure such as nanoparticles, nanorods (NRs), nanowires (NWs), nanobelts, nanorings, nanocombs and nanocages. With these novel properties, it has broad attention due to the distinguished performance in the field of electronics, optics and photonics. With the large surface to volume ratio, it also increases the level of emission of intrinsic or extrinsic defect in the visible range that contributes to UV excitation emission.

Nowadays, the hybridization of a carbon material with the ZnO offers a magnificent way to obtain more interesting properties such as energy storage properties (Jinping Liu et al., 2009), optoelectronic properties (Potts, Dreyer, Bielawski, & Ruoff, 2011) and photocatalytic activity (Y. Guo, Wang, He, Qiu, & Cao, 2009). Besides, high biocompatibility and fast electron transfer kinetics make ZnO layer immobilize and modify biomolecules as a biomimic membrane (Mofor, 2007). It also can be used as anticorrosive coating materials for various metals.

2.2 Properties of Graphene

This section aims to introduce the attractive properties single-, bi- or few-layer graphene. Before introducing the properties of single graphene, it is important to understand the structure of graphene. The introduction to structure of graphene was explained in previous chapter. A single layer graphene is defined as a single two-dimensional material with carbon atom sheets densely packed in a honeycomb crystal lattice. Bi-layer and few layer graphene have two and three up to ten layers of two-dimensional carbon atom sheets respectively. The graphene structures consisting more than ten layers of two-dimensional sheets are considered as thick graphene sheet.

The simplest way to characterize the thickness of graphene layer is through employing microscopic and spectroscopy techniques. Transmission electron microscopy (TEM) is a characterization tool which provides information on morphology and numbers of layers. For single-layer graphene exhibits one dark line where bi- or few-layer graphene exhibit folded edge with double dark lines.

Raman spectroscopy is another way to investigate different thickness of graphene layer. The numbers of graphene layer can be examined from the intensity, shape and portion of G and 2D bands. The intensity of the G band increases with the increasing number of layers. The down-shift of the G band also indicates the increasing number of graphene layers. While the 2D band, the changes in shape, width and position was observed with increasing number of layers. The width of the 2D band can distinguish the single-, bi- and few-layer of graphenes. Single-layer graphene (SLG) is unique in electronic structure, as it shows band-overlap in two conical points (K and K_{\perp}) in the Brillouin zone (Figure 2.1). Thus, SLG is expected to show some unusual properties, as compared with metals and semiconductors and typical of a semi-metal.

Single-layer graphene shows room-temperature ambipolar characteristics, while few-layer graphene shows no energy gap. The structure becomes increasingly metallic the more layers it contains. Graphene shows very high surface area, having good gas adsorption property and hydrogen uptake up to 3 wt% H_2 .

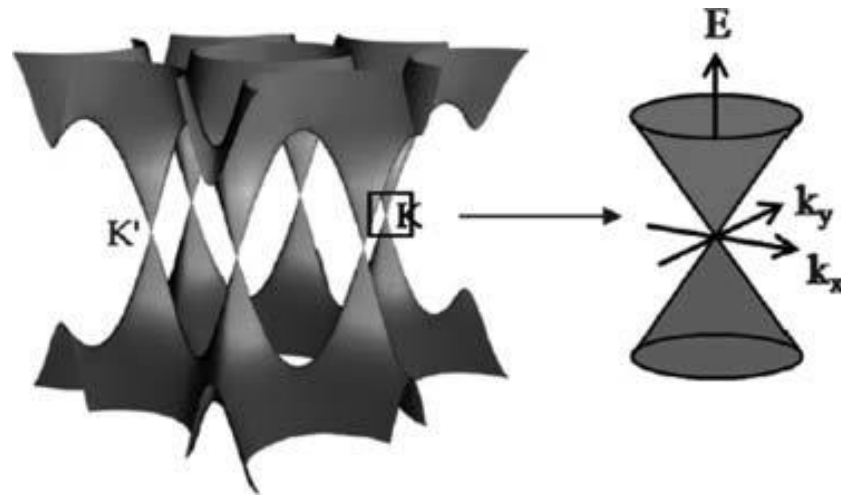


Figure 2.1: The electronic band structure of single-layer graphene (Rao, 2009)

Recent achievements in graphene growth by thermal CVD onto Ni thin film has confirmed reproducibility of good quality graphene on a centimeter scale substrate and successful transfer to many other substrates including Si, glass and PDMS. Although graphene has shown exceptional electrical, optoelectric, and chemical properties and thus, has excellent potential be used as transparent electrode, field effect transistor, sensors and energy applications, synthesis of graphene films on arbitrary substrates with desired energy band gap still remains to be achieved. It is expected that after complete development of graphene films, on a large scale, with desired electrical properties, graphene may become more attractive than silicon-based electronics and thus provide future electric devices with higher speed, chemical stability, environmental friendliness, and better functionality.

2.3 Graphene synthesis

Graphene can be made via several approaches such as micromechanical cleavage of graphite flakes, epitaxial growth via high-temperature treatment of silicon carbide and chemical vapour deposition (CVD) of hydrocarbon on a substrate such as nickel or copper. The micromechanical cleavage of highly oriented pyrolytic graphite or

natural graphite flakes using a Scotch tape. It is the first method to be used to produce graphene at the beginning of this research. It is suitable for fundamental research due to the high structural and electronic quality of the graphene produced. This technique allows reliable and easy preparation but suffers from a low yield (Novoselov et al., 2004). Next, the epitaxial growth of graphene on SiC (Berger, et al., 2004) and metal single-crystal substrates such as Ru and Pt (Berger et al., 2006) at high temperature and in ultrahigh vacuum condition is introduced. It can grow large-size and high-quality graphene, but it requires high-vacuum conditions, high-cost fabrication systems and facing difficulty in transferring the graphene from the substrates as well as low yield. Whereas, the thermal- or plasma-enhanced chemical vapor deposition (CVD) of graphene from the decomposition of hydrocarbons at high temperatures on metal substrates (such as Ni, Cu, Pt) or metal oxide (Al_2O_3 , MgO) particles allows for fast, uniform, large-area, high-quality graphene production. However, it gives a few disadvantages such as high-cost and relatively low yield.

Recently, single- and bi- layer graphenes have been obtained by gas phase using a substrate free, atmospheric pressure microwave plasma reactor (Dato, Radmilovic, Lee, Phillips, & Frenklach, 2008). The single-layer graphene also is reported to be formed by sonication in the water with addition of hydrazine as chemical reduction of graphitic oxide (Gilje, Han, Wang, Wang, & Kaner, 2007). The graphene has also been obtained by thermal exfoliation followed by solubilization and centrifugation of the expandable graphite (X. Li, Wang, Zhang, Lee, & Dai, 2008). Nowadays, the chemical exfoliation and reduction of graphene oxide (GO) has now been demonstrated as a primary approach for the graphene synthesis. It involves oxidation, intercalation, exfoliation and/or reduction of graphene derivatives (S. Park & Ruoff, 2009; Z.-S. Wu et al., 2010), such as graphite, graphite oxide, expandable graphite, CNTs, graphite fluoride and graphite intercalation of compounds. . It is due to the great advantages

which is low-cost strategy and can yield large quantity of graphene especially from GO with high processability.

In this study, we report the chemical exfoliation for the synthesis of graphene oxide which is by using simplified Hummers method (SHM). Consequently, it was reduced to graphene nanocomposite by using simple hydrothermal technique. The Hummers method was found by Hummers and Offeman as alternate oxidation method by reacting graphite flakes with a mixture of potassium permanganate (KMnO_4) and concentrated sulfuric acid (H_2SO_4). In simplified Hummers method, we increased the amount of KMnO_4 , and performed the reaction in a 9:1 mixture of $\text{H}_2\text{SO}_4/\text{H}_3\text{PO}_4$ to improve the efficiency of the oxidation process. This improved method provides a greater amount of hydrophilic oxidized graphene material as compared to Hummers method. This new method also does not generate toxic gas and the temperature is easily controlled. This improved synthesis of GO may be important for large-scale production of GO.

The most common source of graphite used for chemical reaction including oxidation is graphite flakes that naturally occurring material which is purified to remove heteroatomic contaminated (Wissler, 2006). By using the flakes of graphite as a starting material offers a variety of strong chemical oxidants for the synthesis of graphene oxide.

The most important chemical transformation of graphene oxide is its reduction of GO to graphene-like materials. This reduction method can be achieved chemically through the use of strong reduction agent (such as hydrazine), hydrothermal, or electrochemical reaction. The resulting product is very similar to pristine graphene and has been used in a wide range of materials with engineering applications. In addition, to its reduction, however, graphene oxide is a useful platform for the fabrication of

functionalized graphene platelets that can potentially confer improved mechanical, thermal and electronic properties. Both small molecules and polymers have been covalently attached to graphene oxide's highly reactive oxygen functionalities, or non-covalently attached on the graphitic surfaces of chemical modified graphene sheets, for potential use such as polymer composites, paper-like materials, sensors, photovoltaic applications, and drug-delivery systems.

There are so much work remains to be done, however, in developing reliable characterization methods that will aid in unambiguous structural identification as well as synthetic procedures that lead to relatively uniform products. Finally, the development of reduction methods that minimize residual oxygen functionality will be of great value for large-scale synthetic preparations of graphene (Billoski, 1992).

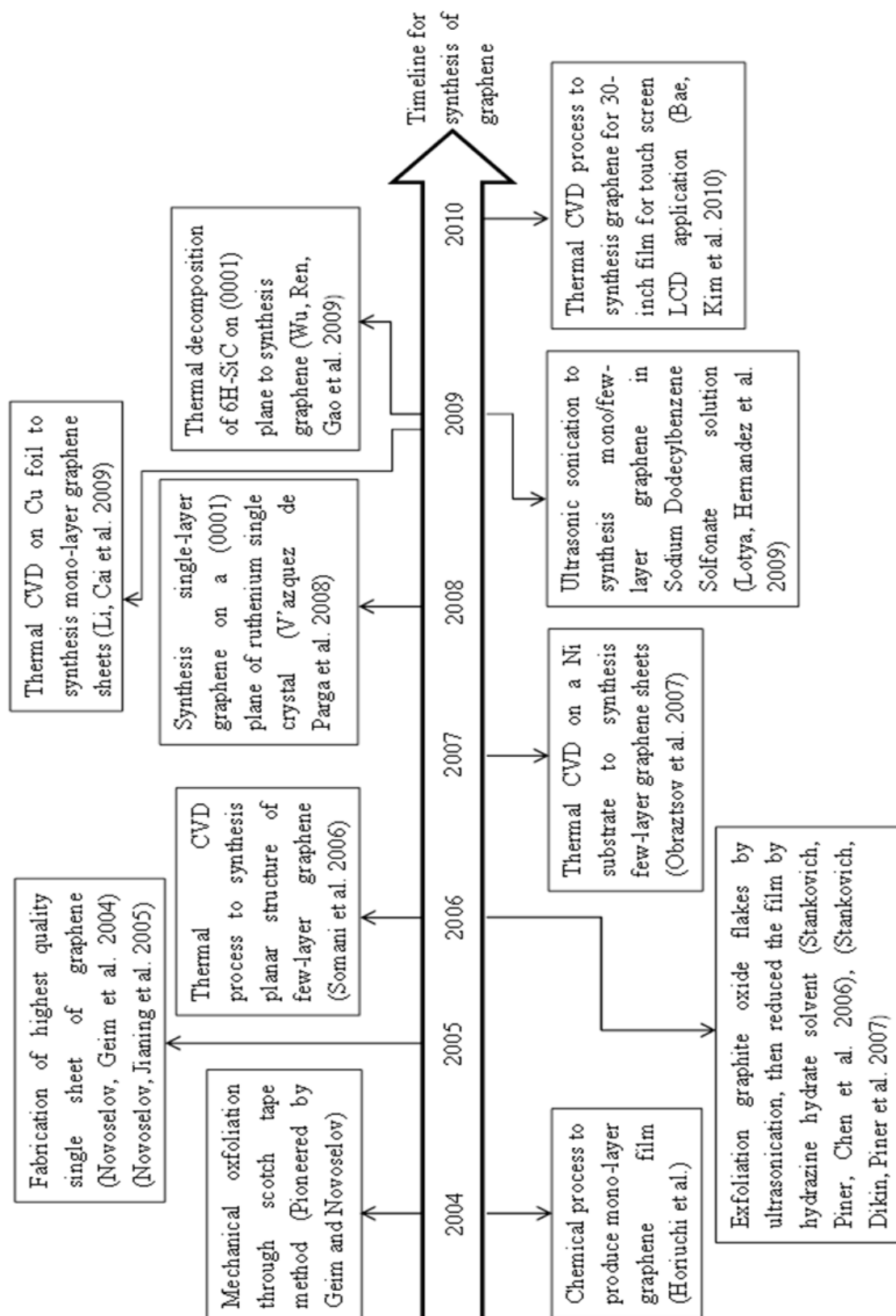


Figure 2.2: Diagram representation of the timeline in the research of graphene with some relevant findings. This information is accurate to the knowledge of the author.

2.4 Graphene-based composite material synthesis

As an environmental friendly approach to gain more exciting performance in variety application, the hybridization of graphene using semiconductor oxides typically TiO_2 or ZnO has been applied to synthesis graphene-based nanocomposite materials. This step can be used to fabricate high quality of graphene based nanocomposite without adding any stabilizer agent. Recently, reduced graphene oxide (RGO) was respectively modified with tin dioxide (SnO_2) and titanium dioxide (TiO_2) via a direct redox reaction between the graphene oxide (GO) and reactive cations Sn^{2+} and Ti^{3+} to form RGO- SnO_2 and RGO- TiO_2 composites (J. Zhang, Xiong, & Zhao, 2011). Characterization data of the composite showed that the excellent photocatalytic performance of the composite materials was associated with the good electrical conductivity and effective charge separation because of the presence of RGO. Other than that, Hybridization between lithium metal oxide and reduced graphene oxide via solvothermal treatment (Han, Kim, Jo, & Hwang, 2012) observed improvement of the electrode performance and photocatalytic activity upon the composite formation. This improvement also performed by TiO_2 nanoparticles decorated graphene that exhibited high photocatalysis performance (D. H. Wang et al., 2009). MnO_2 /graphene, SnO_2 /graphene and ZnO /graphene hybrids or composites have been demonstrated to reveal special features in new hybrids that can be widely utilized in supercapacitors (S. Chen, Zhu, Wu, Han, & Wang, 2010). Compared to other carbon matrices such as graphite (G. X. Wang et al., 2001), carbon black (J. Park, Eom, & Kwon, 2009), and carbon nanotubes (Z. P. Guo, Zhao, Liu, & Dou, 2005), graphene sheets preserve the high electrical conductivity of the overall electrode.

Various methods such as thermal decomposition, covalent coupling, electrochemical route and sol-gel process have been used to obtain these composites and

explore their new properties. William et al. (Williams & Kamat, 2009) and Akhavan et al (Akhavan, 2011) fabricated graphene-ZnO or graphene-TiO₂ composites by UV-assisted photocatalytic reduction in ethanol solution. Wu et al. (J. Wu, Shen, Jiang, Wang, & Chen, 2010) used the general solvothermal approach for the preparation of sandwich-like graphene/ZnO in ethylene glycol medium.

Overall, the synthesis graphene/metal oxides are highlighting the unique structure of composites that have significant improvement in their electrochemical properties such as high capacity, high rate capability and excellent cycling stability. In all synthesis mentioned above, carbon material/ZnO systems exhibit excellent physical and chemical properties. Therefore, the fabricating graphene/ZnO via simple, efficient and low cost method is crucial for applications related to environmental issues. To the best of our knowledge, little research on the fabrication of graphene/ZnO and functionalized graphene/ZnO nanocomposites in a water system has been reported so far. So, this investigation opens a novel and insightful way to develop sensing applications.

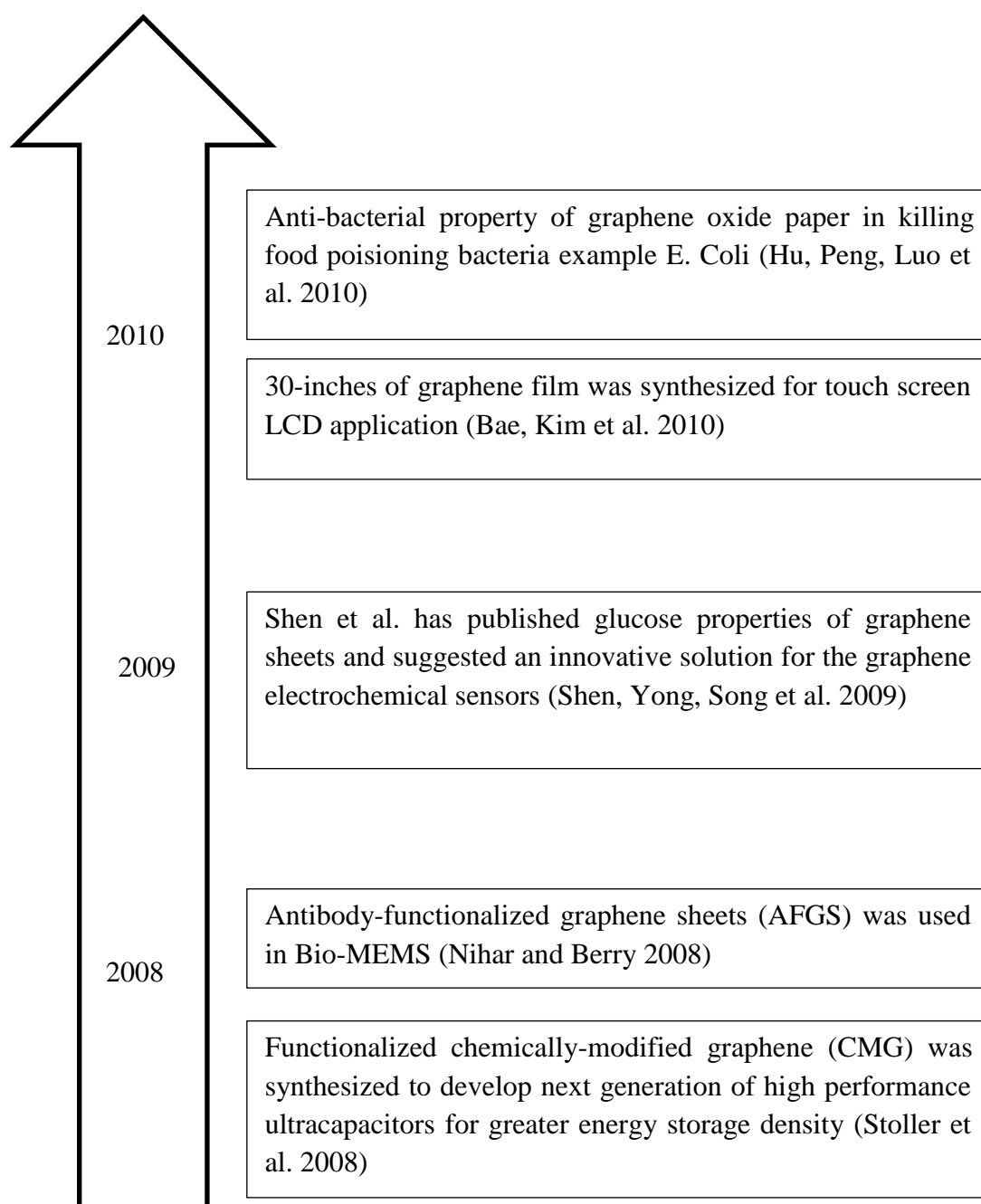
Timeline for the applications of graphene

Figure 2.3: Diagram representation of the application based on graphene since it is first discovered. This information is accurate to the knowledge of the author.

2.5 Hydrothermal method

The hydrothermal technique was first discovered by the German Chemist, Robert Bunsen when he reacted chemical in aqueous solution in thick-walled glass tube at temperature above 200 °C and pressure above 100 bars. He finally obtained crystals of barium carbonate and strontium carbonate under these conditions. Based on the history, the hydrothermal synthesis can be defined as a method of synthesizing single crystals which depends on the solubility of mineral in high-temperature of aqueous solution at high pressure. It is also can be defined as a synthesis method for growing single crystals from an aqueous solution in autoclave (a thick-walled steel vessel) at high temperature and pressure. Water at elevated temperatures plays an important role in precursor material transformation. Sometime this technique known as solvothermal method when the media used is solvent with the same general principal of the method. The syntheses are usually conducted at autogeneous pressure at specific temperature and composition of the hydrothermal solution. The upper limit of the temperature can extend over 1000 °C and 500 MPa pressure (Roy, 1994). However, hydrothermal with mild conditions are commonly used where the temperature less than 350 °C at pressure less than approximately 50 MPa.

The intensive research has led to a better understanding of hydrothermal chemistry which significantly reduced the time reaction, temperature and pressure for hydrothermal crystallization of material (Byrappa & Yoshimura, 2001; Roy, 1994). Because of this, it makes hydrothermal synthesis more economical processes that can be engineered using cost-effective and proven pressure reactor technology and methodologies. Besides, the hydrothermal synthesis offers many other advantages over conventional and non-conventional synthesis method. The hydrothermal synthesis has ability to prepare crystal powder directly from the solution regulates the rate and

uniform of nucleation, growth and aging. As a result, it improves the controlling of size, crystallite morphology and significantly reduces the aggregation level which is not possible in many other synthesis process (Riman, Suchanek, & Lencka, 2002). Furthermore, the hydrothermal crystallization can be monitored in-situ using a range of techniques (Riman, et al., 2002; Sunagawa, Tsukamoto, Maiwa, & Onuma, 1995) which allow the determination of crystal growth mechanism and a better controlling process. Another advantage of hydrothermal synthesis is the as-synthesized powder exceeds the purity of the starting materials. This occurs since the hydrothermal crystallization is a self-purifying process. During the process, the growing crystals/crystallites tend to reject impurities present in the growth environment. Subsequently, the impurities are removed from the system together with the crystallizing solution during washed process. The hydrothermal synthesis also can take place in wide variety of aqueous and solvent mixture-based systems. In general, this process allows for automation operation such as charging, transportation, and mixing and product separation. In addition, hydrothermal method is environmental friendly synthesis compared to many other synthesis which attribute to energy conservation at low temperature, absence of milling, able to recycle waste and safe disposal of waste that cannot be recycled (Yoshimura, Suchanek, & Byrappa, 2000). Moreover, the materials obtained through hydrothermal synthesis often exhibit differences in point of defects compared to material prepared by high-temperature synthesis method.

CHAPTER 3

EXPERIMENTAL METHODS

3.1 Introduction

This chapter presents experimental and characterization techniques which have been employed in this work. The nanocomposite samples were produced by using hydrothermal method with different concentration of initial GO or FGO. The other parameters were used as constants throughout the entire experiment. Thus, the effects of different concentrations towards the different types of nanocomposites are studied.

The content of this chapter is divided into two main sections. The first section introduces the hydrothermal route and procedures for the sample preparation. The second part presents experimental methods employed. The morphological, structural and composition for each sample were characterized by using X-Ray Diffraction (XRD), Fourier transform infrared spectroscopy (FTIR), Field Emission Scanning Electron Microscope (FESEM), Raman Spectroscopy, Thermogravimetric analysis (TGA), High Resolution Transmission Electron Microscope (HRTEM) and X-ray Photoelectron Spectroscopy (XPS). The optical properties were studied by using UV-Visible Spectroscopy (UV-Vis) and Photoluminescence Spectroscopy (PL). These analytical methods and experimental results were used to discuss in the following chapter.

3.2 Materials

The raw materials were used in this research are graphite flake (3061, Asbury Graphite Mill Inc.), zinc acetate dihydrate (99.9%), potassium permanganate (KMnO_4) and sodium hydroxide (NaOH) were purchased from R&M Chemicals, N-(trimethoxysilylpropyl) ethylenediamine triacetic acid sodium salt aqueous solution (45%) was supplied by Gelest Inc., ammonia solution ($\text{NH}_3 \cdot \text{H}_2\text{O}$, 25%) was purchased from Riedel-de Haën and sulfuric acid (H_2SO_4 , 98%), phosphoric acid (H_3PO_4), Hydrochloric acid (HCl) and hydrogen peroxide (H_2O_2 , 30%) aqueous solution were purchased from System. All chemical were used as received without further purification.

3.2 Sample preparation

Hydrothermal process was carried out by using autoclave. The autoclave is made as follow. The outer and the lid of autoclave are made by metal, while the inner is made by Teflon as a capsule where the reaction takes place during the route. It also has the lid that is made of Teflon with thickness of 0.5 cm. The dimension of metal cylinder autoclave is 5.5 cm in outer diameter, 4.2 in inner diameter and 9.0 cm height. The thickness of the Teflon is 0.5 cm with the maximum tube capacity of 50 ml. Figure 3.1 shows the image of autoclave. In our experiment, the Teflon lid form a permanent water-tight seal when the metal lid expands as temperature is raised. Firstly, 20 ml of graphene oxide solution and zinc ions were poured into the Teflon tube. After sealing by using Teflon tape, the autoclave was tight up with outer metal lid. After that, the sealed autoclave was put in the furnace at 180 °C with a heating rate of 5°C/min for 24 hours. After the hydrothermal treatment was finished, the autoclave was cooled to room temperature before the sample is collected. The collected precipitation was filtered and

underwent washing process with ethanol and deionized water for several time. Finally, the precipitation was dried in oven for 24 hours. Figure 3.1 shows the image of the autoclave that was used to synthesis the samples. The body of autoclave is made of stainless steel while the inner side was made of Teflon-lined (white colour) where the synthesis process took place.



Figure 3.1: Image of the autoclave.

3.2.1 *Synthesis of graphene oxide (GO)*

The preparation of graphene oxide (GO) was carried out by using simplified Hummers method (SHM) in which 3.0 g graphite flake was added into 360 ml of concentrated H_2SO_4 and 40 ml of H_3PO_4 under magnetic stirring. The ratio of the concentrated H_2SO_4 to H_3PO_4 is 9 to 1. Then, 18 g of KMnO_4 was added gradually into the solution. After the KMnO_4 was added, the solution turned green which displays the reaction of KMnO_4 with the acidic solution. The reaction mixture was continued for three days. After three days of reaction, the mixture was poured into 400ml of cold deionized water with 27 ml of 30% H_2O_2 . This action was performed in an ice bath since the addition of concentrated H_2SO_4 medium into the mixture of deionized water and H_2O_2 released large amount of heat. Then, the mixture was stirred for about 10 minutes until the color of the mixture changed to brilliant yellow. Finally, the mixture was washed with 1 M of HCl and deionized water for several times to remove metal ions and acid by using high speed of centrifugation. Figure 3.2 displays the synthesis process of simplified Hummers method (SHM).

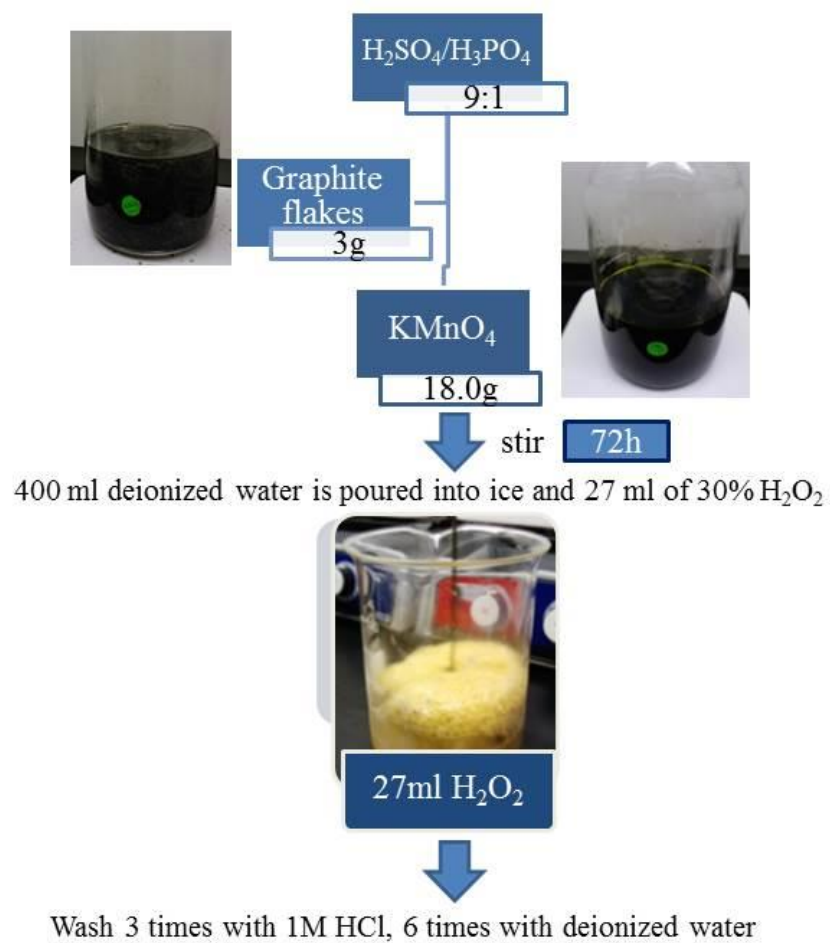


Figure 3.2: Image of the synthesis process of GO via the simplified Hummers method (SHM).



Figure 3.3: The real image of Centrifuge CR21GIII; Hitachi, Japan.

After underwent the washing process, the GO solution is displayed as Figure 3.4. The GO solution appeared in clear brownish colour. Dry GO can be determined by heating GO solution at 50 °C for three days. The concentration of GO solution also can be determined by drying process.

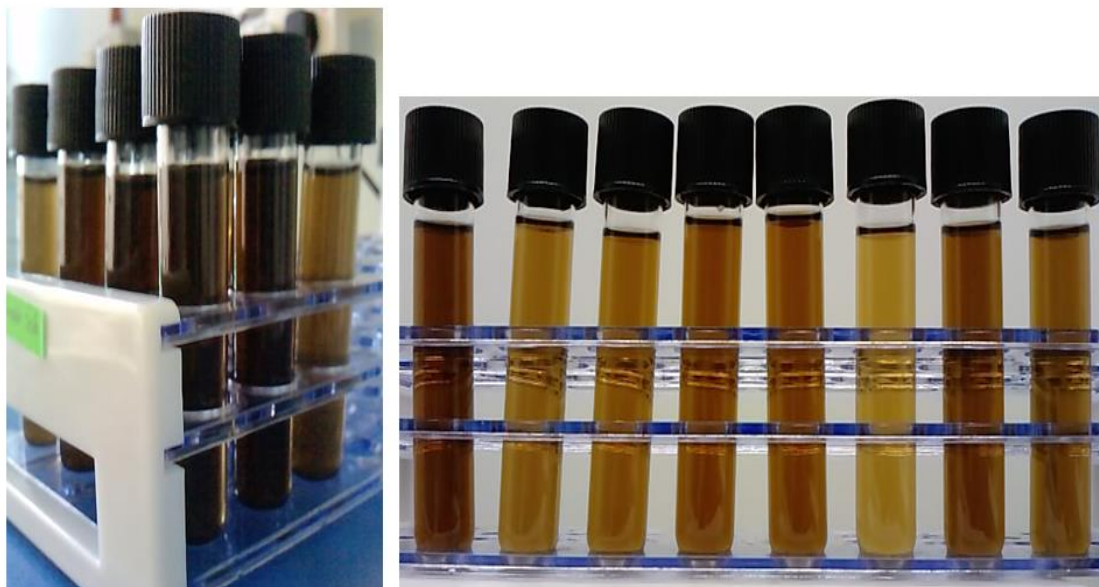


Figure 3.4: Images of GO solution after washing processes.

3.2.2 Synthesis of functionalized graphene oxide (FGO)

The synthesis of functionalized graphene oxide (FGO) was carried out by dispersed 200 mg of dry GO from previous yield in 300 ml absolute ethanol. The mixture was undergone sonication for 1 hour. Then, the mixture was continued to be stirred in reflux stirring at temperature $(60 \pm 5)^\circ\text{C}$. 1 to 1.24 ml of N-(trimethoxysilylpropyl) ethylenediamine triacetic acid sodium salt was dissolved into 15 ml of distilled water. Next, the N-(trimethoxysilylpropyl) ethylenediamine triacetic acid sodium salt solution was then added gradually into GO mixture, and then reflux stirring was continued for next 16 to 18 hours. Then, 100 to 200 ml of methanol was added to the mixture before it was left for a while until it settled down at the bottom of flask. The product was then filtered and washed with acetone and distilled water (60 ml: 40 ml) to remove the long chain Si-O polymer from N-(trimethoxysilylpropyl) ethylenediamine triacetic acid sodium salt. The washing process was continued by using ethanol in order to remove unexpected ions. Finally, the black product was harvested by pursing centrifugation and drying at 80°C for 12 hours. This step is important to ensure Silicon

oxide (SiO) from N-(trimethoxysilylpropyl) ethylenediamine triacetic acid sodium salt chemically bonded to GO sheets. The final product obtained with large number of functional group attached to GO sheets to make it possible for further reaction to take place.

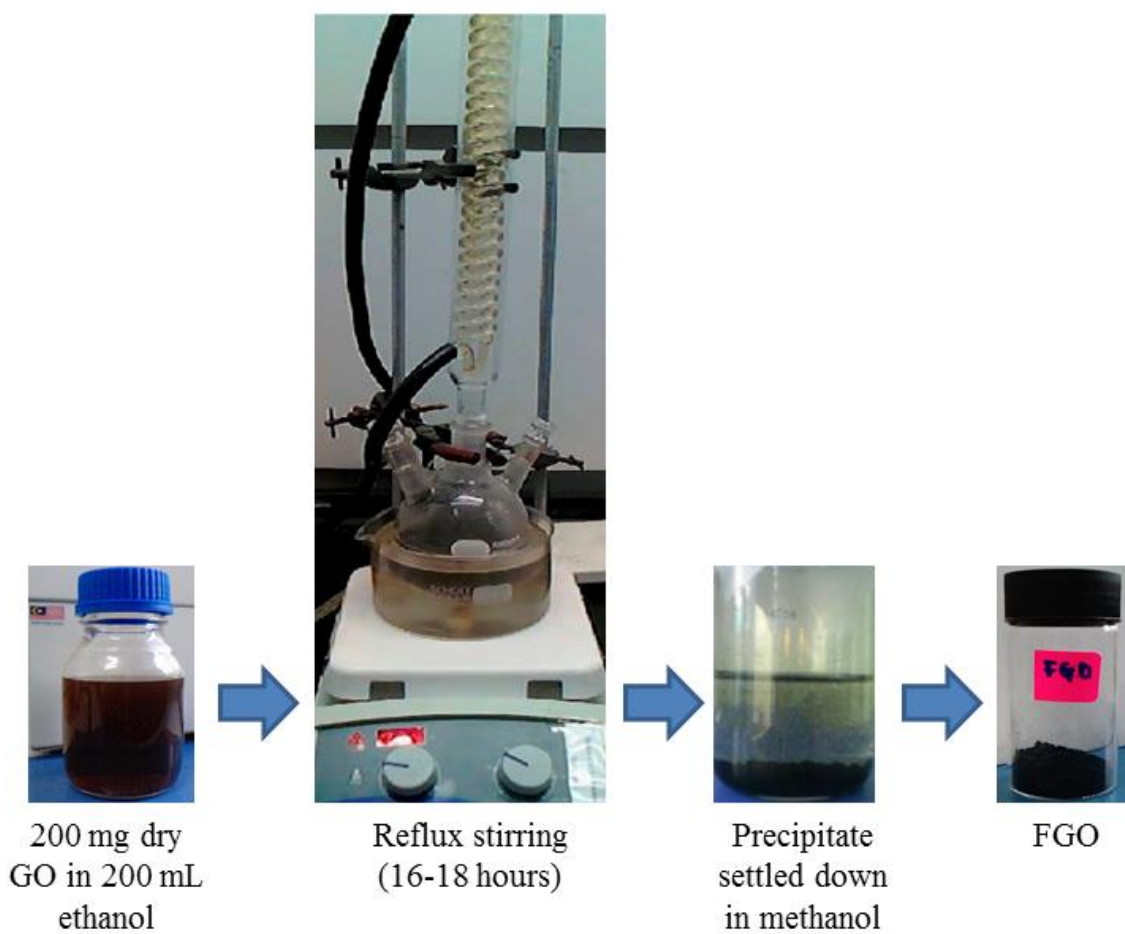


Figure 3.5: Image of synthesis process to prepare FGO.

3.2.3 Preparation of nanorod-like reduced Graphene/Zinc Oxide (rG/ZnO) nanocomposite

ZnO sol was synthesized from zinc acetate dihydrate ($\text{Zn}(\text{CH}_3\text{COO})_2 \cdot 2\text{H}_2\text{O}$). 2.75 g of $\text{Zn}(\text{CH}_3\text{COO})_2 \cdot 2\text{H}_2\text{O}$ and 1 g NaOH were dissolved into 25 ml of 25% of ammonia solution ($\text{NH}_3 \cdot \text{H}_2\text{O}$). Then, deionized water was added until 125 ml of solution was achieved to maintain the concentration of zinc ions at 0.1 mole (M). The nanocomposite was prepared by mixing 2 ml of zinc ions complex into 18 ml of GO solution at different concentrations (as shown in table 3.1). Then, the mixture was stirred by reflux stirring at maintain temperature (60 ± 2) °C. The reaction was continued by adding 1.0 ml of 0.1 M NaOH gradually to increase the pH condition of the mixture (~10). The mixture was continued stir for 1 hour until it became cloudy and dark brown of agglomeration was present. Next, the mixture was put into a Teflon-lined autoclave and underwent hydrothermal treatment for 24 hour at 180 °C (shown in Figure 3.5). The product was rinsed with deionized water and ethanol several times, and the final product was obtained after dried at 60 °C.

Table 3.1: Table displays the volume of GO and DI water needed to prepare GO solution at different concentration.

Sample	GO concentration (mg/ml)	Volume of GO used (ml)	DI water added (ml)	Volume of 0.1 M zinc ions used (ml)
A	0.0	0.0	18.0	2.0
B	0.2	1.6	16.4	2.0
C	0.6	4.8	13.2	2.0
D	1.0	8.0	10.0	2.0

Other parameters were kept constant throughout the synthesis process as tabulated in Table 3.2. The effects of varying the concentration of graphene oxide solution were studied.

Table 3.2: Table displays the constant parameters for the synthesis of graphene/zinc oxide nanocomposites.

Parameters	Set values
1. Sonication	40% W (30 minutes)
2. Temperature for reflux stirring	60 ± 2 °C
3. pH condition	~10
4. Hydrothermal temperature	180 ± 5 °C
5. Hydrothermal period	24 hours
6. Drying temperature	60 ± 2 °C
7. Drying period	24 hours

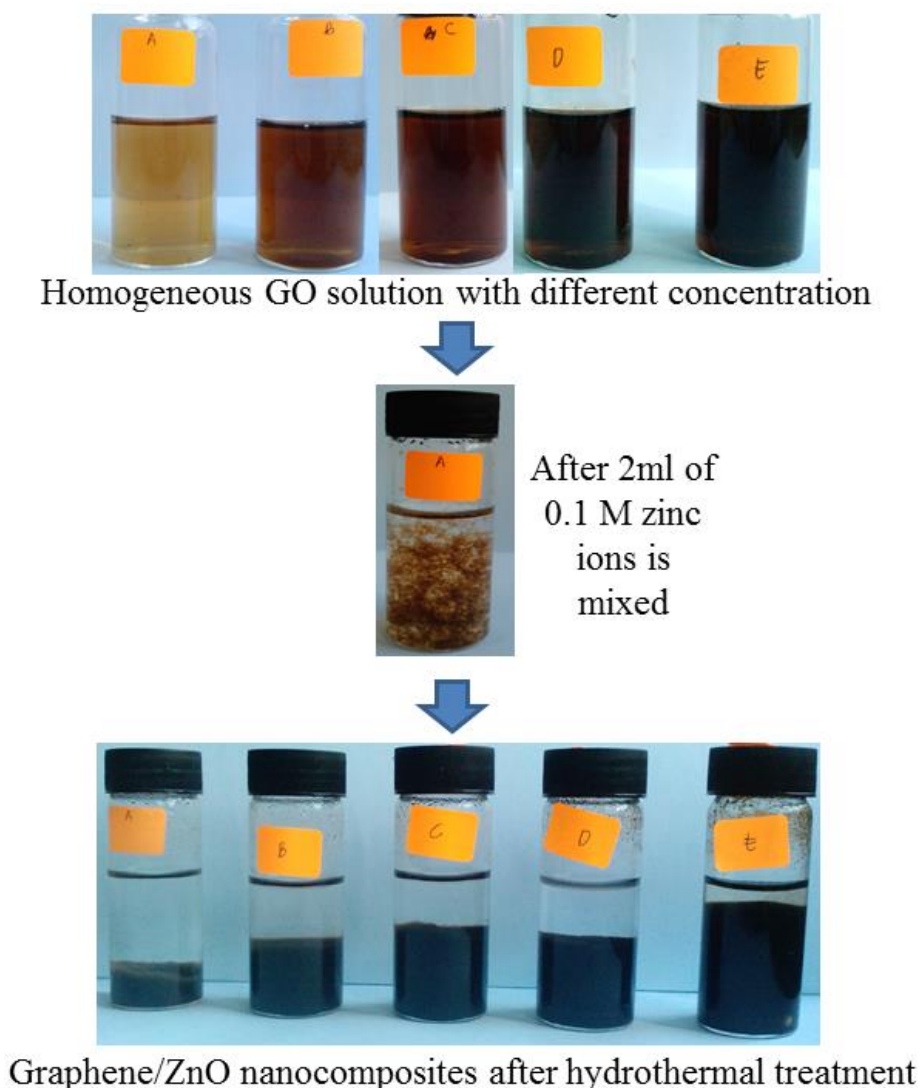


Figure 3.6: The synthesis process of graphene/ZnO nanocomposite by hydrothermal treatment.

From the final product that were obtained as shown in Figure 3.6, it shows that the concentration of GO solution used in the initial step increased, the amount of nanocomposite produced also increased.

3.2.4 Preparation of flower-like reduced Functionalized Graphene/Zinc Oxide (rFG/ZnO) nanocomposite

The rFG/ZnO nanocomposite with desirable nanostructures was synthesized via hydrothermal route. Firstly, 2 ml of 0.1 M $\text{ZnAc.NH}_3\text{.H}_2\text{O}$ was mixed into

functionalized graphene oxide (FGO) solution with concentration of 1.0 mg/ml by a mild sonication for 30 minutes. The mixture was stirred under reflux stirring at temperature 60 °C for 1 hour. Then, the mixture was transferred into autoclaves and treated at temperature 180 °C for 24 hours. Next, the precipitates were washed with distilled water and ethanol for several times, followed by drying process at 60 °C for 24 hours. The product was obtained in powder formed.

3.3 Characterizations and Analytical procedures

This section describes characterization and analytical procedures carried out to characterize the samples. These characterization methods include X-Ray Diffraction (XRD) (Philips D5000 X-Ray Diffractometer) to determine the crystallinity of the nanocomposite. The Field Emission Scanning Electron Microscope (FESEM) (FEI Quanta 400F FESEM) and Transmission Electron Microscope (TEM) (CM12, Philips) were performed to study the surface morphology and structural properties of the samples. The TEM was operated at 100 kV which allowed the image of graphene sheets and nanoparticles to be gathered. The compositions of the samples were characterized using X-ray Photoelectron Spectroscopy (XPS). The XPS was performed by using synchrotron light at beamline no. 3.2 of Siam Photon Laboratory, Synchrotron Light Research Institute, Thailand. The XPS was operated in the conditions of maximum photon energy 600 eV and kinetic energy step of 0.1 eV. The structural characteristics of the samples were obtained by a Renishaw inVia Raman microscope with laser excited at 514 nm. Ultraviolet-Visible (UV-vis) spectroscopy and photoluminescence (PL) were used for optical properties measurement. Fourier transformed infrared spectra were recorded on a Thermo Nicolet iS10 spectrophotometer (Washington, USA) by the KBr method. The UV-vis (Evolution 300, Thermo Fisher Scientific, Pittsburgh, PA) was used to characterize the graphene/ZnO nanocomposites. However, the Shimadzu

UV-VIS spectrophotometer was used to characterize optical properties of functional graphene/ZnO nanocomposite. The photoluminescence curves were obtained by using Renishaw inVia PL microscope with laser excited at 325 nm. Thermogravimetric analysis (TGA) (Q500, TA Instruments, New Castle, DE) was performed to study thermal behaviors of nanocomposites. The atomic arrangements of samples were obtained via High Resolution Transmission Electron Microscope (HRTEM) (JEOL JEM 2100F).

3.3.1 Phase and crystalline structures via X-ray Diffraction (XRD)

The phase and crystalline structure of the samples obtained by hydrothermal route were investigated by X-ray diffraction patterns. These patterns were carried out using a Philips D5000 X-Ray Diffractometer. Copper (Cu) $K\alpha$ radiation with a wavelength of 1.4506 Å and rate scan degree of 0.02 degrees⁻¹ was used in this diffraction analysis. The wavelength attributed to Cu $K\alpha$ is comparable to atomic distance in crystal and ideally suited for probing the structural arrangement of atoms in wide range of materials. Hence, the energetic x-rays not only penetrate deep into materials but also providing the information of their crystalline structures. The crystalline has noticeable sharp peak characteristic, while broad peak (look like a hump) is characteristic for amorphous structure. When x-rays, electrons and neutrons rays with the short wavelength close to interatomic distance are applied to crystals, thus diffraction phenomena occur on the lattice planes in the crystals. When the photons of incident x-rays collide with above electrons, some photons are deflected away from the incident x-rays direction as shown in figure below. If the wavelength of scattered x-rays does not change by the collision, such process is known as an elastic scattering. The scattered x-rays are able to carry the information relating to electron distribution in crystals. The identification of unknown material has been performed with a powder

XRD. The powder can be the aggregation of fine grains with a single crystal structure and each of fine grain is randomly oriented. When x-rays is directed to the powder, the diffraction intensity is assumed to be the sum of x-rays deflected from all fine grains. Hence, the diffraction peak is attributed to the Miller indices of the powder is observed.

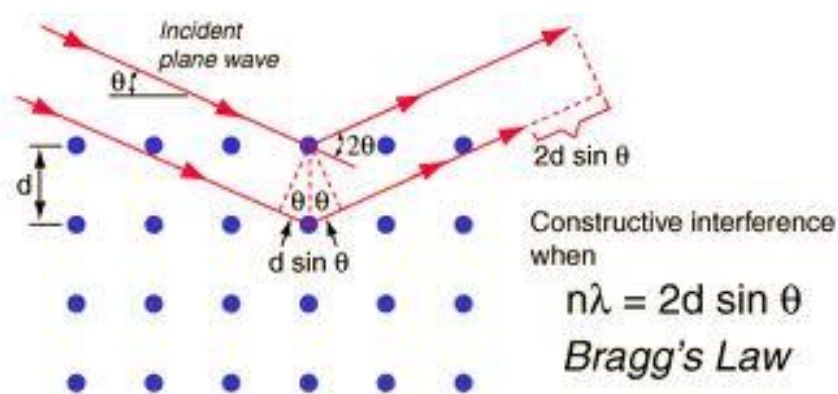


Figure 3.7: Figure shows the angle of reflection is equal to the angle of incidence ("X-ray Diffraction,").



Figure 3.8: Real image of Philips D5000 X-Ray Diffractometer.

3.3.2 High resolution surface images obtained by using Field emission scanning electron microscope (FESEM)

FESEM is the abbreviation of Field Emission Scanning Electron Microscope. A FESEM is microscope that works with electrons (particles with a negative charge) instead of light. These electrons are liberated by a field emission source. The object is scanned by electrons according to a zig-zag pattern.



Figure 3.9: Real image of FEI Quanta 400F FESEM.

A FESEM is used to visualize very small topographic details on the surface or entire or fractioned objects. Researchers apply this technique to observe structures that may be as small as 1 nanometer (= billion of a millimeter). The FESEM may be employed for example to study organelles and DNA material in cells, synthetic polymers, and coatings on microchips. The microscope that has served as an example for the virtual FESEM is a JEOL 6330 that is coupled to a special freeze-fracturing

device (Oxford Ato). Electrons are liberated from a field emission source and accelerated in a high electrical field gradient. Within the high vacuum column these so-called primary electrons are focused and deflected by electronic lenses to produce a narrow scan beam that bombards the object. As a result secondary electrons are emitted from each spot on the object. The angle and velocity of these secondary electrons relates to the surface structure of the object. A detector catches the secondary electrons and produces an electronic signal. This signal is amplified and transformed to a video scan-image that can be seen on a monitor or to a digital image that can be saved and processed further.

The powder samples were dispersed in 99% concentrated ethanol and sonicated for 5 to 10 minutes to form homogeneous solution. Then the solutions were put on silicon dioxide substrate by drop cast technique. The samples were dried in the fume hood for 10 to 15 minutes to make sure it fully dried before the test.

3.3.3 High Resolution Transmission electron microscope (HRTEM)

The high resolution transmission electron microscope is a tool used to characterize the microstructure of materials at very high spatial resolution. The low resolution of TEM is best about 0.2 nm (10^{-9} m), which is about 1000 times better than ordinary light microscope. This high spatial resolution make HRTEM is possible to gather information about the morphology, crystal structure and its defects, crystal phases and composition of the materials. The HRTEM contains four components involving electron source, electromagnetic lens system, sample holder and imaging system as shown in a schematic outline of HRTEM (Figure 3.10).

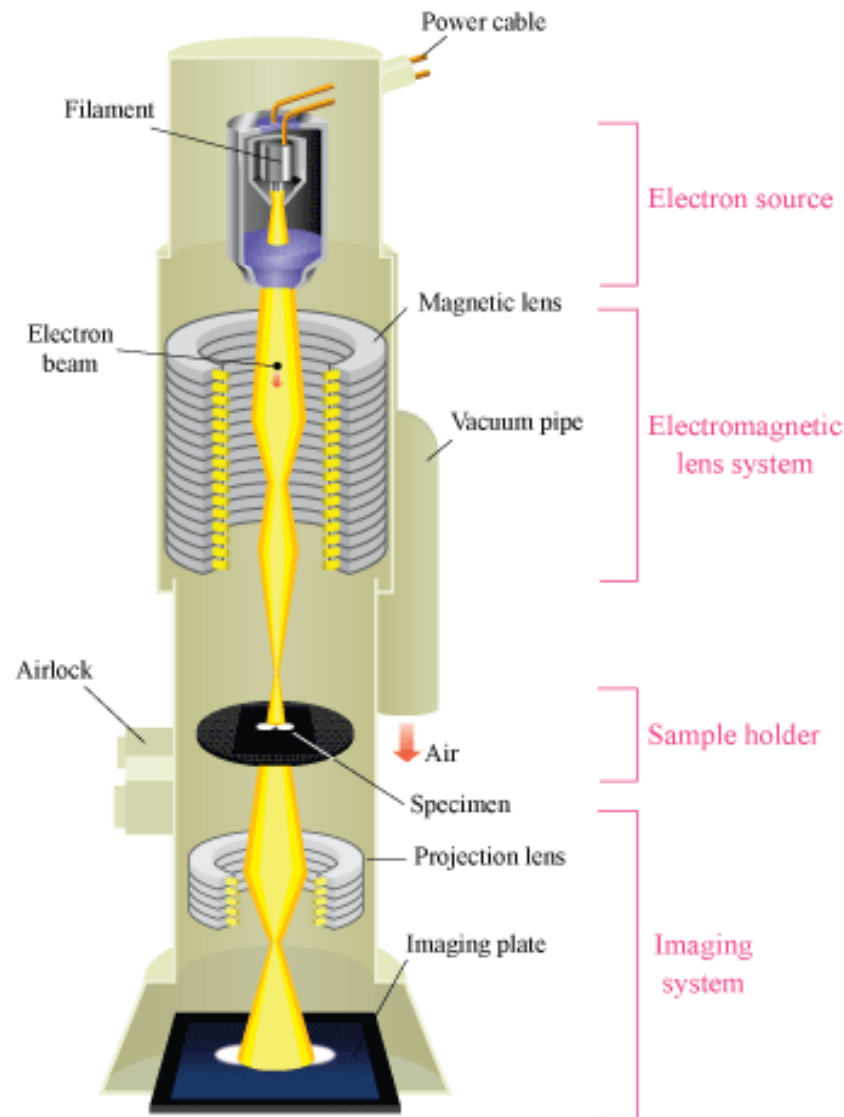


Figure 3.10: The schematic outline of HRTEM ("Basic principle of transmission electron microscope,").

The work principle of HRTEM is like a slide projector. A projector shines a beam of light which transmits through the slide. While, the HRTEM work in the same way except it shines a beam of electron through the sample. The electrons are accelerated several hundred kV under vacuum condition tightly focused by using electromagnetic lens and metal apertures. At this stage, only electrons with a small energy range are allowed to pass through the system. Thus, the electrons in the electron beam with a well-defined energy then hitting the sample on the sample holder. The loss and scattering of the electrons by individual parts of the sample is then refocused by

objective lens. The other objective lens enlarged the image and projected it onto the phosphorescent screen for viewing.

High resolution TEM is a tool that provides the images that show the structures at the atomic scale. That means it is able to identify features on the size of 2\AA (2.10^{-10} m). Therefore, it shows the arrangement of atom in a crystal, interfaces between crystal or defects in a crystal. To understand the different imaging modes it is necessary to understand the imaging system of a low resolution TEM. In a low resolution TEM, a very thin specimen is irradiated by an electron beam. Magnetic lenses, solenoids are used to manipulate the electron beam. So that, the electrons will travel along the symmetry axis of the lenses

In order to obtain high resolution images containing lattice fringes, the interference of the unscattered and scattered beam is used. The electrons can be described as a wavefront. By using HRTEM, the spacing between lattice fringes can be measured. The image below is an example of HRTEM image. The image exhibits the bright strips known as lattice fringes which can appear in one or more directions. If the specimen is very thin, this fringe can be interpreted as the projection of the tunnels between columns of atoms. While, the dark strips represent the atoms themselves.

During sample preparation, the graphene/ZnO-1.0 sample was dispersed in the highly concentrated ethanol (99% concentration). Then, the sample was sonicated for 15 minutes. Finally, it was dried up for 10 to 15 minutes in the fume hood by using drop casting technique on the copper grid. This sample needs to be prepared at least one day before the measurement in order to ensure the sample is fully dry. This needs to be emphasized to prevent the electrical contact while the reading is measured. This also becomes the main reason we used high concentrated ethanol as a solvent to disperse the nanocomposite sample.

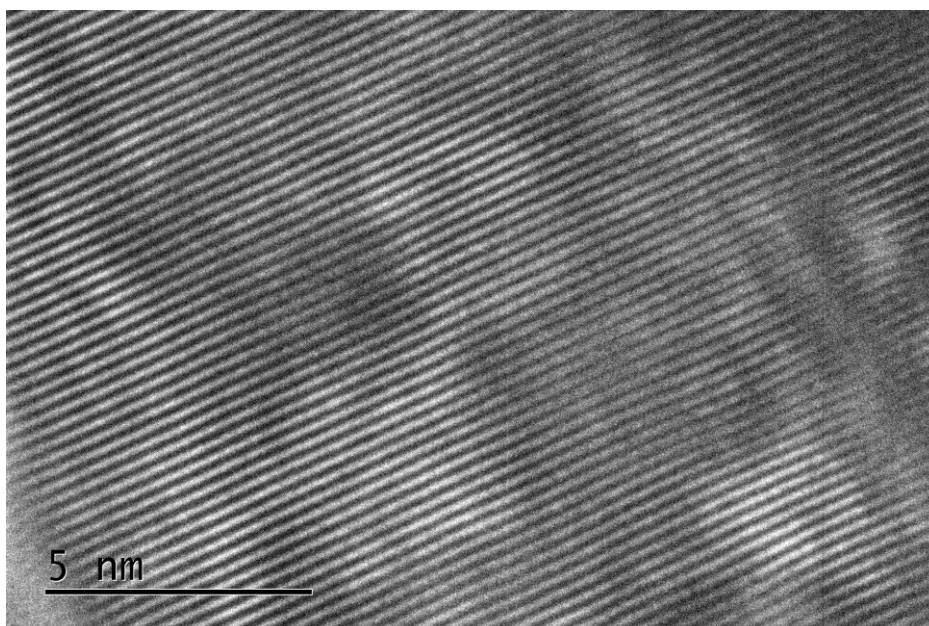


Figure 3.11: Figure shows bright and dark strips deduced from HRTEM image.

3.3.4 Composition obtained by X-ray Photoelectron spectroscopy (XPS)

X-ray photoelectron spectroscopy (XPS) is a quantitative spectroscopic technique that measures the elemental composition, empirical formula, chemical state and electronic state of the elements that exist within a material. XPS spectra are obtained by irradiating a material with a beam of X-rays while simultaneously measuring the kinetic energy and number of electrons that escape from the top 1 to 10 nm of the material being analyzed. XPS requires ultra-high vacuum (UHV) conditions. In brief, XPS serve as a unique probe to impurities and its chemical formation on your sample surfaces identifying the defects and contamination of your products.

The energy of electromagnetic wave was formulated by Einstein on the basis on the experiment performed by Hertz. Einstein quantized the energy as photon energy, because the energy depends on the frequency of waves. Once, the wave frequency is selected, the energy of electrons is determined.

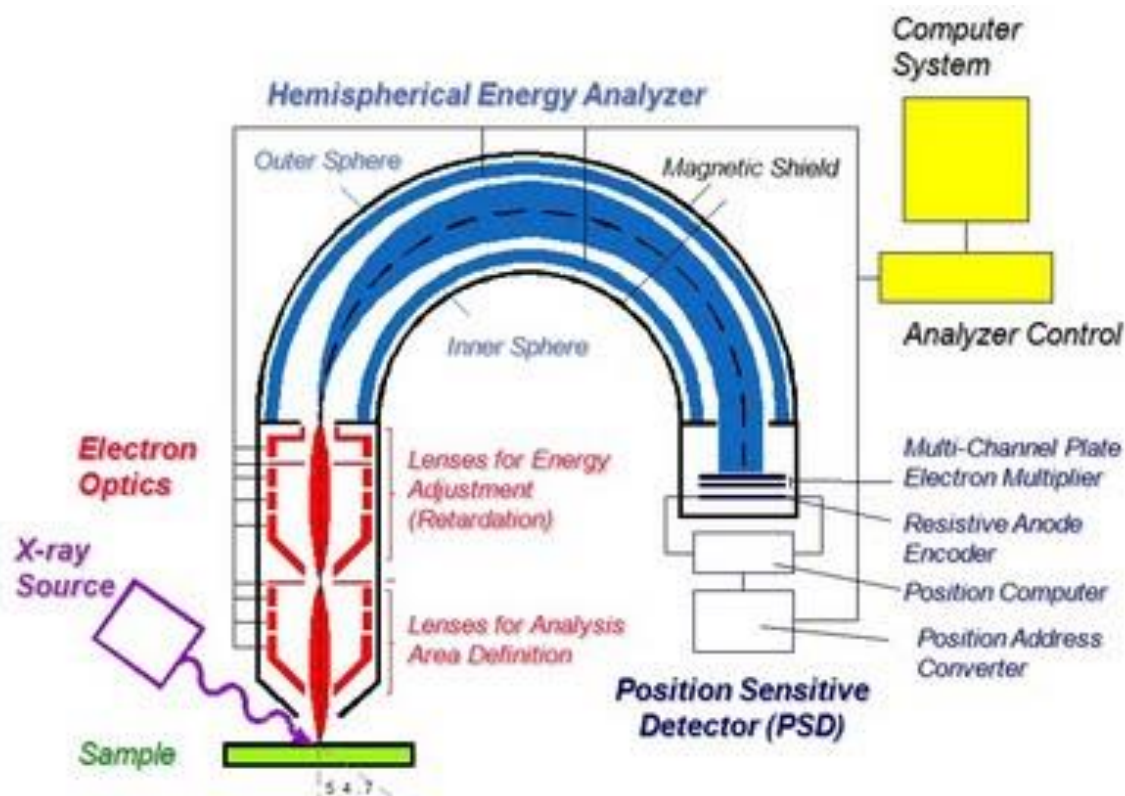


Figure 3.12: The schematic principle of X-ray photoelectron spectroscopy ("Material Surface Analysis with X-Ray Photoelectron Spectroscopy (XPS)," May 10, 2011).

In principle, electrons ejected from the surface are energy filtered via a hemispherical analyzer (HSA) before the intensity for a defined energy is recorded by a detector. Since core level electrons in solid-state atoms are quantized, the resulting energy spectra exhibit resonance peaks characteristic of the electronic structure for atoms at the sample surface. While the x-rays may penetrate deep into the sample, the escape depth of the ejected electrons is limited. That is, for energies around 1400 eV, ejected electrons from depths greater than 10nm have a low probability of leaving the surface without undergoing an energy loss event, and therefore contribute to the background signal rather than well-defined primary photoelectric peaks. The energies of the photoelectric lines are well-defined in terms of the binding energy of the electronic states of atoms. Further, the chemical environments of the atom at the surface result in well-defined energy shifts to the peak energies.

During sample preparation, the sample was dispersed in the highly concentrated ethanol (99% concentration). Then, the sample was sonicated for 15 minutes. Finally, it was dried up for 10 to 15 minutes in the fume hood by using drop cast technique on glass substrate with dimension 2 cm x 2 cm. This sample needs to be prepared at least one day before the measurement in order to ensure the sample is fully dry. This needs to be emphasized to prevent the electrical contact while the reading is measured.

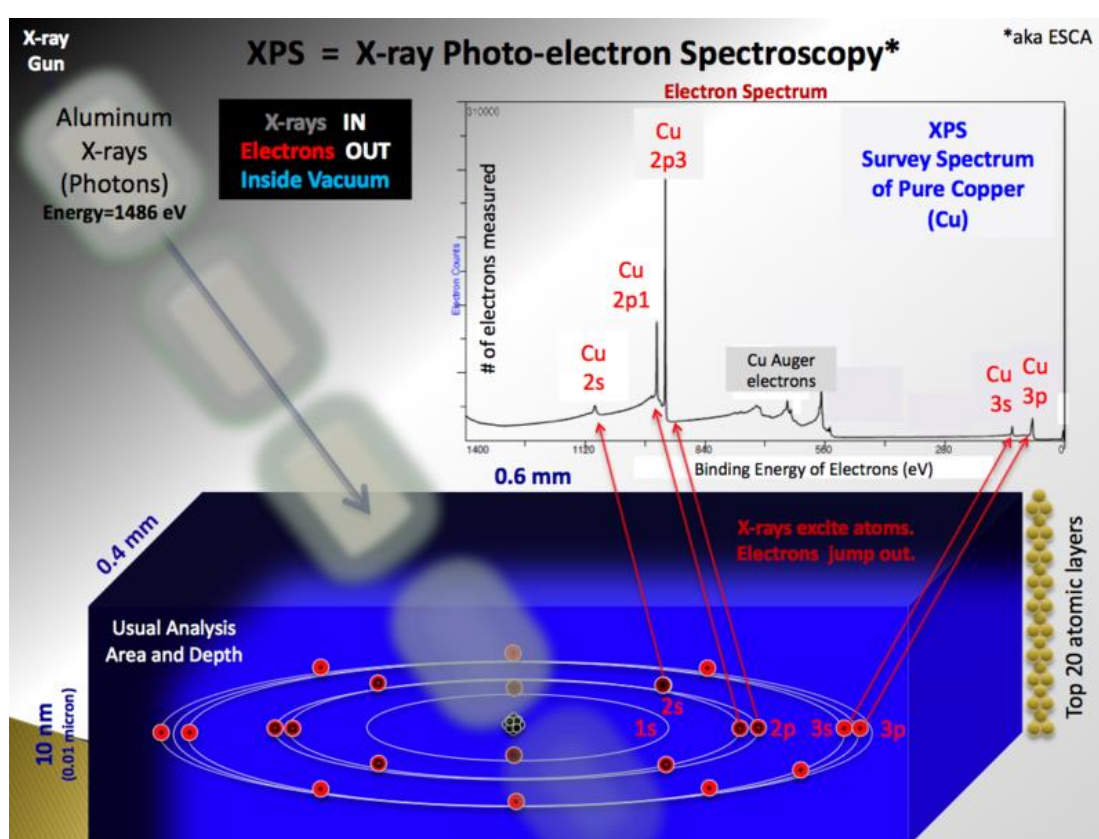


Figure 3.13: Rough schematic of XPS physics - "Photoelectric Effect. XPS spectral lines are identified by the shell from which the electron was ejected (1s, 2s, 2p, etc.) (Bvcrist., 10 June 2010).

3.3.5 Structural characteristics determined by Raman spectroscopy

Raman Spectroscopy is a method of determining modes of molecular motions. Raman effects is based on molecular deformations in electric field that obtained by molecular polarizability α . As the laser beam is considered as an oscillating

electromagnetic wave with the electrical vector E , thus the interaction with the sample induces the electric dipole moment, $P = \alpha E$ which referred to deformed molecules. The deformation of the molecules causes vibrational of molecules with certain characteristic frequency ν_m . A Raman microscope typically consists of four components begin with a standard optical microscope, an excitation laser, a monochromator, and a sensitive detector such as a charge-coupled device (CCD) or photomultiplier tube (PMT) (Figure 3.14). It is predominantly applicable to the qualitative and quantitative analyses of covalently bonded molecules. It relies on Raman scattering of monochromatic light from a laser beam in the visible, near to ultraviolet or near infrared region. The laser interacts with molecular vibration or phonons in the system, resulting the laser photon being shifted at higher or lower energy level as shown in Figure 3.15. This shift in energy level gives the information about the vibrational, rotational and other low frequency of the system that is being measured.

A sample is usually illuminated with a laser beam. Then the scattered light from illuminated spot is collected by a lens and is sent via a monochromator to obtain Raman spectra of the sample. Wavelengths are almost identical to laser line due to elastic Rayleigh scattering that filtered out and the rest of the scattered light is dispersed onto a detector.

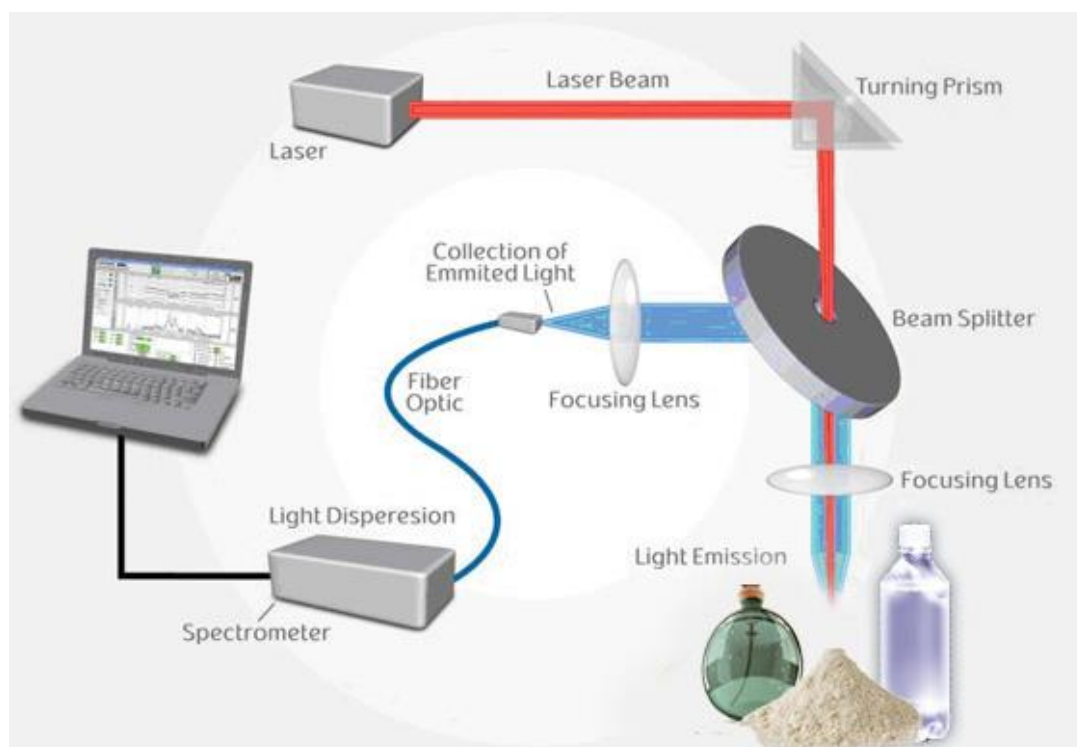


Figure 3.14: Schematic diagram of Raman spectroscopy ("Technology Methods," 2011).

The Raman spectroscopy gives advantages for microscopic analysis. Because it is a scattering technique, sample does not need to be fixed or sectioned. Raman spectra can be collected from a very small volume ($< 1 \mu\text{m}$ in diameter), these spectra allow the identification of species present in that volume. Water does not generally interfere with Raman spectral analysis. Thus, Raman spectroscopy is suitable for the microscopic examination of minerals, materials such as polymers and ceramics, cells, proteins and forensic trace evidence.

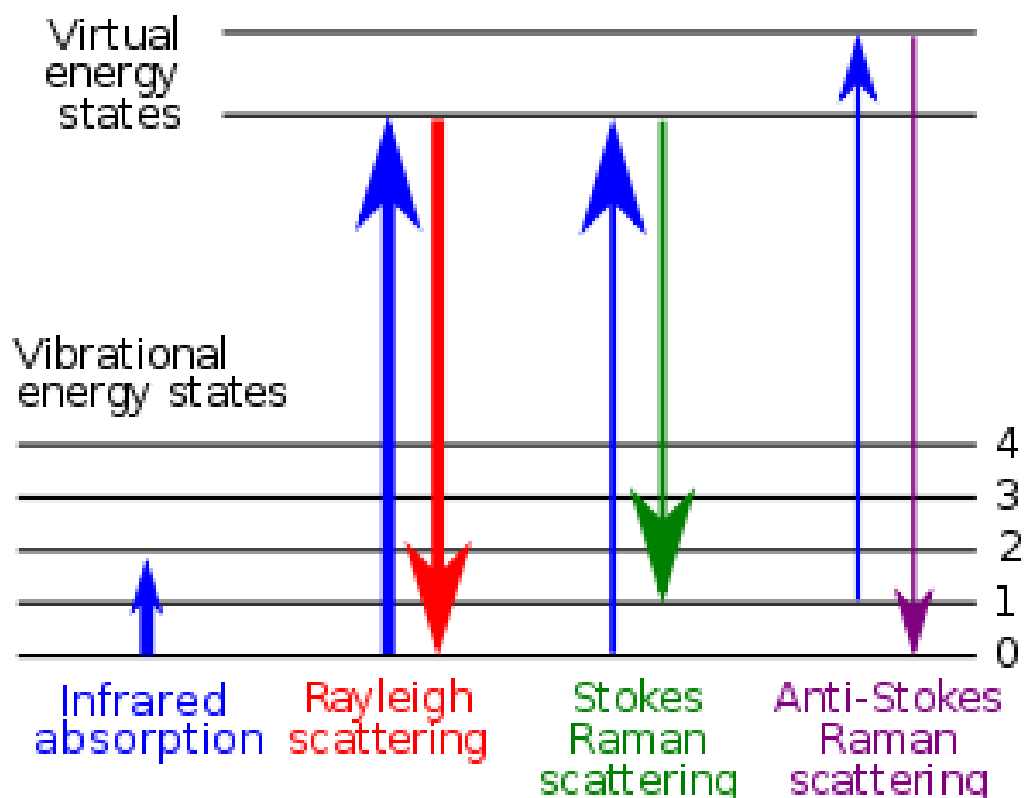


Figure 3.15: Energy level diagram show the states involved in Raman signal(Moxfyre, 18 September 2009).

During sample preparation, the sample was dispersed in the highly concentrated ethanol (99% concentration). Then, the sample was sonicated for 15 minutes. Finally, it was dried up for 10 to 15 minutes in the fume hood by using drop cast technique on the corning glass or silicon dioxide substrate. This sample needs to be prepared at least one day before the measurement in order to ensure the sample is fully dry. This needs to be emphasized to prevent the electrical contact while the reading is measured.

Raman spectra of samples were obtained with a Renishaw inVia Raman microscope with 514 nm laser as excitation source. The incident laser beam was spotted on the top of sample that dropped cast on the corning glass or silicon dioxide substrates. Figure 3.16 displays the spot of the sample that was exposed to laser beam before Raman spectra was obtained. The cross sign displays the laser beam. Raman spectra were obtained in the range frequency of $100\text{--}3000\text{ cm}^{-1}$.

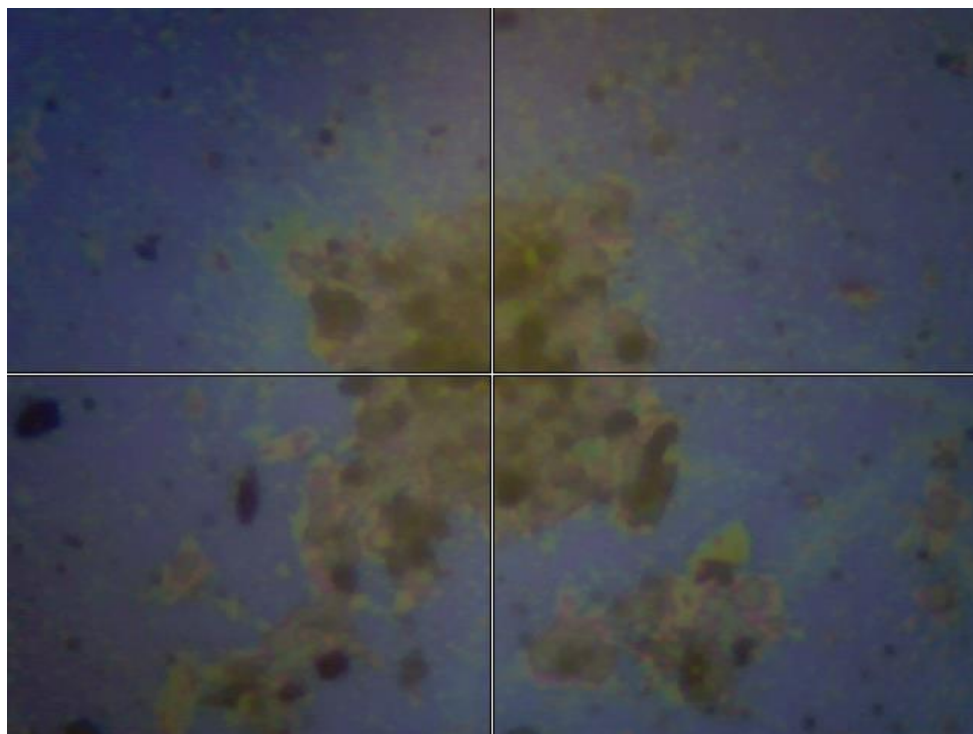


Figure 3.16: Figure shows laser beams that were spotted on the top surface of sample.



Figure 3.17: Real image of Renishaw inVia Raman microscope.

3.3.6 Optical absorption properties by Ultra violet visible spectroscopy (UV-vis)

A UV-Visible spectroscopy is used to characterize the samples optically with known amount of light at specific wavelength passed through the samples. The UV-Visible spectroscopy consists of a source of radiation, monochromator and optical geometry, sample compartment, detector and measuring system (Figure 3.18).

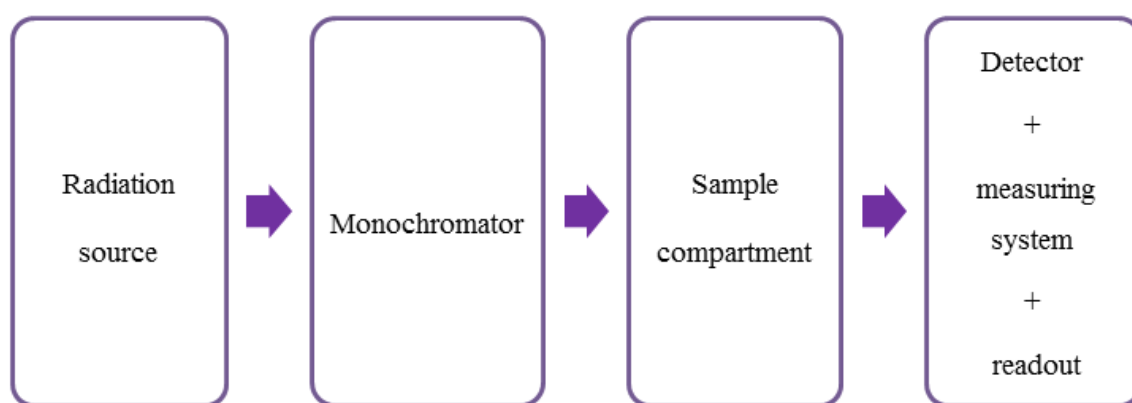


Figure 3.18: Basic components of UV-visible spectroscopy.

When the known amount of the light with the specific wavelength emitted from light source, it will pass through the samples and be collected as the final results which showed the optical properties of the samples. There will be a difference between the amount of light emitted by the light source and the amount of light collected, which depends on the material that was tested. It is because different materials will collect different amounts of light passed through it since it has a specific absorbance capacity with certain wavelength. The data can be used to calculate absorption in arbitrary units and optical transparency spectrum percentage of materials. But, in the current study, only absorption spectrum was measured. In order to measure the absorbance spectrum, the solution was put in the quartz container with the dimension of $1 \times 1 \times 4.5 \text{ cm}^3$. Once measuring the light beam from the source passed through the width of the container.

During sample preparation, the powder sample was dispersed in concentrated ethanol (99% concentration). Then, the sample was sonicated for 30 minutes to get a homogeneous solution. After that, five to eight drops of solution was added into deionized water (DIW) for the characterization. The baseline measurement spectrum was taken by using DIW since the solutions involved were suspended in the deionized water. Thus all the solution spectra were referenced to deionized water. For all the measurements were run by using Thermoscientific Evolution 300 UV-visible spectroscopy and Shimadzu UV-VIS spectrophotometer. The measurements were performed in spectral region of 190 nm to 900 nm. Figure 3.19 shows a schematic diagram of device operation.

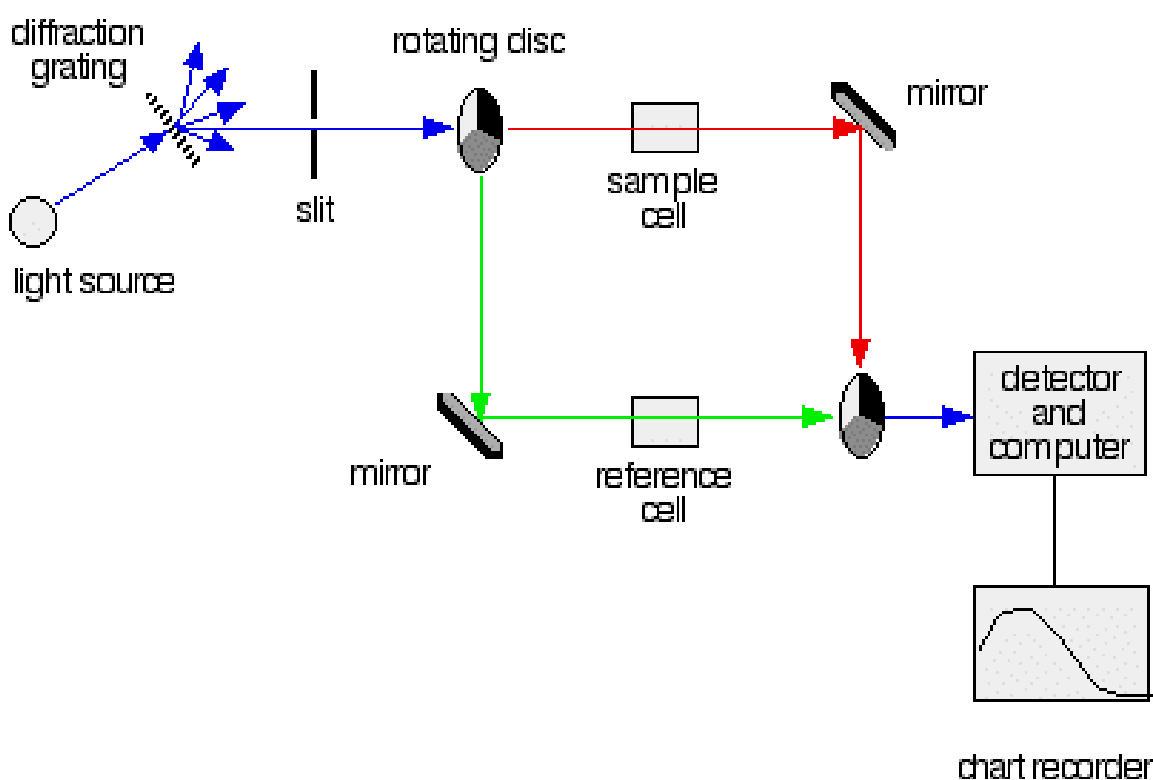


Figure 3.19: The schematic diagram of device operation (Clark, 2006).



Figure 3.20: Real image of UltraViolet (UV-vis) spectroscopy (Evolution 300, Thermo Fisher Scientific, Pittsburgh, PA).

3.3.7 Photoluminescence (PL) spectroscopy

The photoluminescence (PL) spectroscopy is a powerful tool to investigate the electronic structure, intrinsic and extrinsic of semiconducting or semi-insulating materials. Light source in PL operating system is directed onto a sample, where it absorbs and imparts the excess energy into the material which known as photo-excitation. These excitations eventually relax and the electrons return to the ground state. If radiative relaxation occurs, the emitted light is called PL. This light can be collected and analyzed to give information about the photo-excited material. The energy of the emitted light (PL) relates to the difference in energy level between two electron states involved in the transition between the excited state and the equilibrium state. The PL intensity gives a direct measure of the relative rates of radiative and nonradiative recombination. The PL is very much dependent on the nature of the optical excitation. The excitation energy selects the initial photoexcited state and governs the penetration

depth of the incident light. The PL signal also often depends on the density of photoexcited electrons. In order to control this parameter, the intensity of the incident beam can be adjusted accordingly.

The instrumentation that is required for PL to work is modest including an optical source and an optical power meter or spectrophotometer. A typical PL set-up is shown in Figure 3.21. First of all, an excited wavelength is selected by first monochromator then luminescence is observed through a second monochromator, which normally positioned at 90° to the incident light in order to minimize the intensity of scattered light reaching the detector. When the light from the laser beam hits the sample, photoluminescence occurs and light is emitted from the sample at wavelengths dependent on the composition of the sample. This sample is oriented such that the reflected laser beam and the PL emission propagate in different directions. Then, the emitted light is directed into a fibre optic cable and then into a spectrometer. A filter may be placed in front of the fibre input to filter off any incident laser light. Inside the spectrometer, a diffraction grating diffracts different wavelengths in different directions towards an array of photo-detectors. The photo-detectors measured the intensity of each wavelength component. The digital information is then interpreted by the computer for displaying a PL spectrum. The spectrum indicates the relative intensities of the light of various wavelengths entering the detector. The whole process must be carried out in the dark.

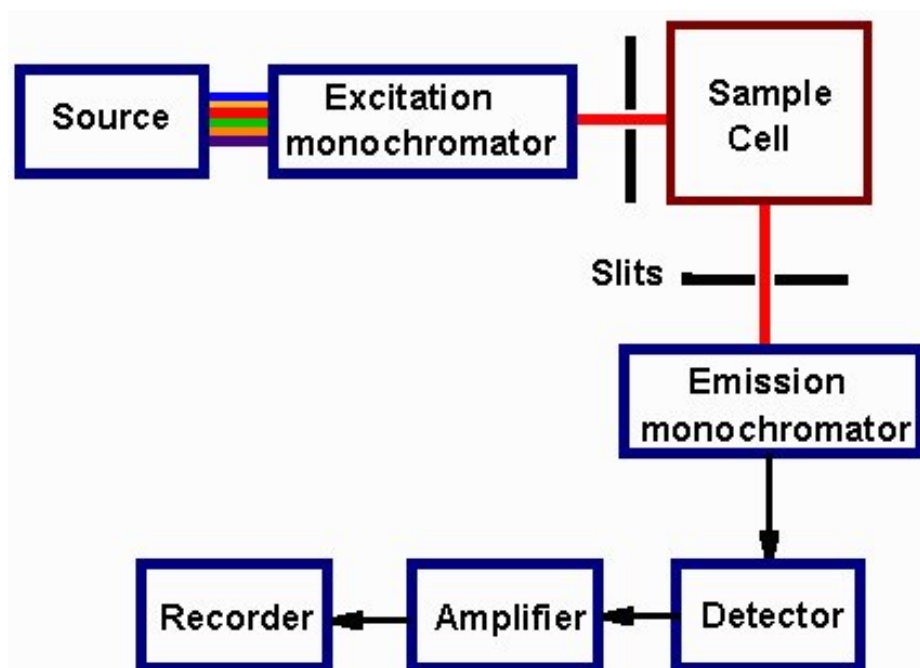


Figure 3.21: Typical experimental set-up for PL measurements ("Molecular Fluorescence Spectroscopy,").

As the measurement does not rely on electrical excitation or detection, sample preparation is not that critical. This feature makes PL particularly suitable for material systems exhibiting poor conductivity or undeveloped contact/junction technology. The measurement of the continuous wave PL intensity and spectrum is fast and straightforward. On the other hand, investigating transient PL is more challenging, especially if recombination processes are fast. Instrumentation for time-resolved detection, such as single photon counting, can be quite expensive and complex. Even so, PL is one of the only techniques available for investigating fast transient behavior in materials.

During sample preparation, the sample was dispersed in the highly concentrated ethanol (99% concentration). Then, the sample was sonicated for 15 minutes. Finally, it was dried up for 10 to 15 minutes in the fume hood by using drop cast technique on the corning glass or silicon dioxide substrate. This sample needs to be prepared at least one day before the measurement in order to ensure the sample is fully dry. The

photoluminescence (PL) spectra were recorded on a Renishaw fluorescence spectrophotometer with a 325 nm excitation line. These measurements were performed in order to study the optical properties of pure ZnO and FG/ZnO nanocomposites.



Figure 3.22: Real image of Renishaw inVia PL microscope with laser excited at 325 nm.

3.3.8 Thermal behavior properties determined by Thermogravimetric analysis (TGA)

TGA is an essential tool in which the mass of a material is measured as a function of temperature and time, under controlled atmosphere. It is ideally used to characterize materials that exhibit weight loss or gain due to decomposition, oxidation, or dehydration. Measurements are primarily used to determine the composition of multicomponent systems and to predict their thermal stability of materials. A typical operating range for the furnace is ambient to 1500 °C, with heating rates up to 200 °C/min. Thus, TGA is able to provide information about the moisture and volatile content of

materials, thermal stability, degradation characteristics, lifetime breakdown, sintering behavior and reaction kinetics of the materials.

A TGA consists of a sample pan that is supported by a precision balance which is placed in a furnace and is heated or cooled during the experimental process. The mass of a substance is monitored during the experiment. The substance is heated under flow of nitrogen environment with constant heat rate while the weight change during this process is measured. Figure 3.23 shows the schematic principle of TGA measurement.

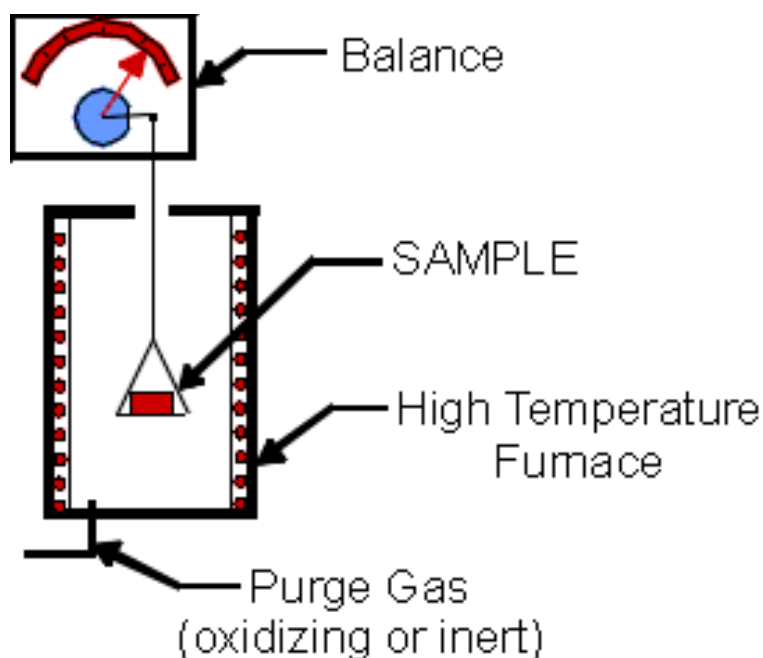


Figure 3.23: The schematic principle of TGA measurement (Skoog).

In this case, TGA is utilized to study the thermal stability of the synthesized decomposition of materials. Thermal stability is defined by the resistance of a material to permanent change in the properties caused solely by heat. In TGA, a continuous graph of mass change against temperature is obtained when a substance is heated at a uniform rate or kept at constant temperature. A plot of mass change versus temperature (T) is referred to as the thermogravimetric curve as shown in Figure 3.24.

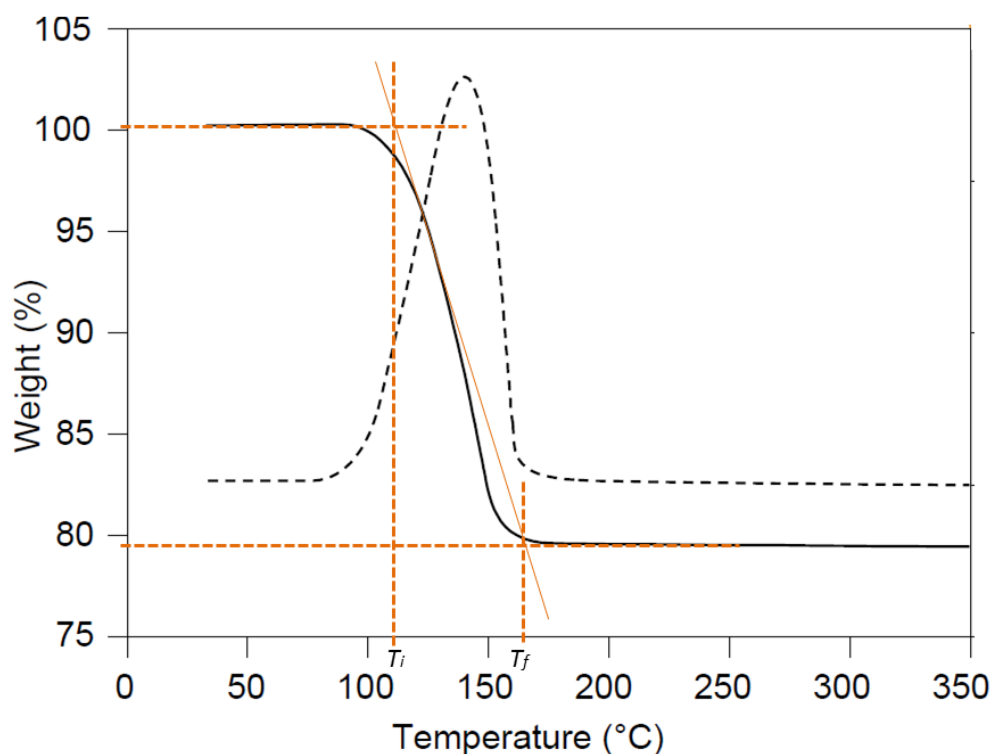


Figure 3.24: TG curve of weight (%) versus temperature (°C).

In a TG curve of single stage decomposition, there are two characteristic temperatures; the initial T_i and the final temperature T_f . T_i is defined as the lowest temperature at which the onset of a mass change can be detected by thermobalance operating under particular conditions while T_f as the final temperature at which the particular decomposition appear to be complete. The difference $T_f - T_i$ is termed as reaction interval. In a dynamic thermogravimetry a sample is subjected to continuous increase in temperature usually linear with time whereas in isothermal or static thermogravimetry the sample is maintained at a constant temperature for a period of time during which any change in mass is noted. The TG curves of a pure compound are characteristics of that compound. Using TG curve we can relate the mass changes to the stoichiometry involved. This can often lead us directly to the quantitative analysis of samples whose quantitative composition is known.

In current study, 5.0 mg of each powder samples were putted in the pan that located in the TGA furnace before the measurement. The TG curves were measured by

using TA instruments Q500 over the temperature range of 20-1000 °C with a scan rate 20 °C/min under nitrogen atmosphere.

CHAPTER 4

RESULTS AND DISCUSSIONS

4.1 Introduction and Overview

This chapter presents the characterizations and discussion of graphene/zinc oxide nanocomposites synthesized from the previous chapter. There are significant changes in the structure of nanocomposite in the present of different types of solution as the starting material in the synthesis process. In this chapter, the characterizations and discussion have been divided into two parts based on the different of starting material which are graphene oxide (GO) and functionalized graphene oxide (FGO) solutions.

The main focus of this chapter is to introduce the two different structures of graphene/zinc oxide nanocomposite that were obtained through same condition of hydrothermal but in different the starting material solution used. By using graphene oxide solution as starting material, the graphene/zinc oxide nanorod-like was obtained. Whereas, by replacing the functionalized graphene oxide as the starting material, the different structure of nanoflower-like zinc oxide decorated graphene sheets were obtained. The structural and morphological evolutions of the nanocomposites were studied by Field Emission Scanning Electron Microscope (FESEM), High Resolution Transmission Electron Microscope (HRTEM) and Raman Spectroscopy. For optical properties, the UV-Visible Spectroscopy (UV-vis) and photoluminescence (PL) were carried out, while the crystallinity and thermal behavior of nanocomposites were investigated through X-ray Diffraction (XRD) and Thermogravimetric analysis (TGA) respectively.

4.2 Nanorod-like Graphene/zinc Oxide Nanocomposite

4.2.1 Field emission scanning electron microscope (FESEM)

The variation of surface images of the graphene/zinc oxide nanorod-like nanocomposites is shown in Figure 4.1. The as-synthesized samples were prepared on silicon dioxide for the FESEM measurements.

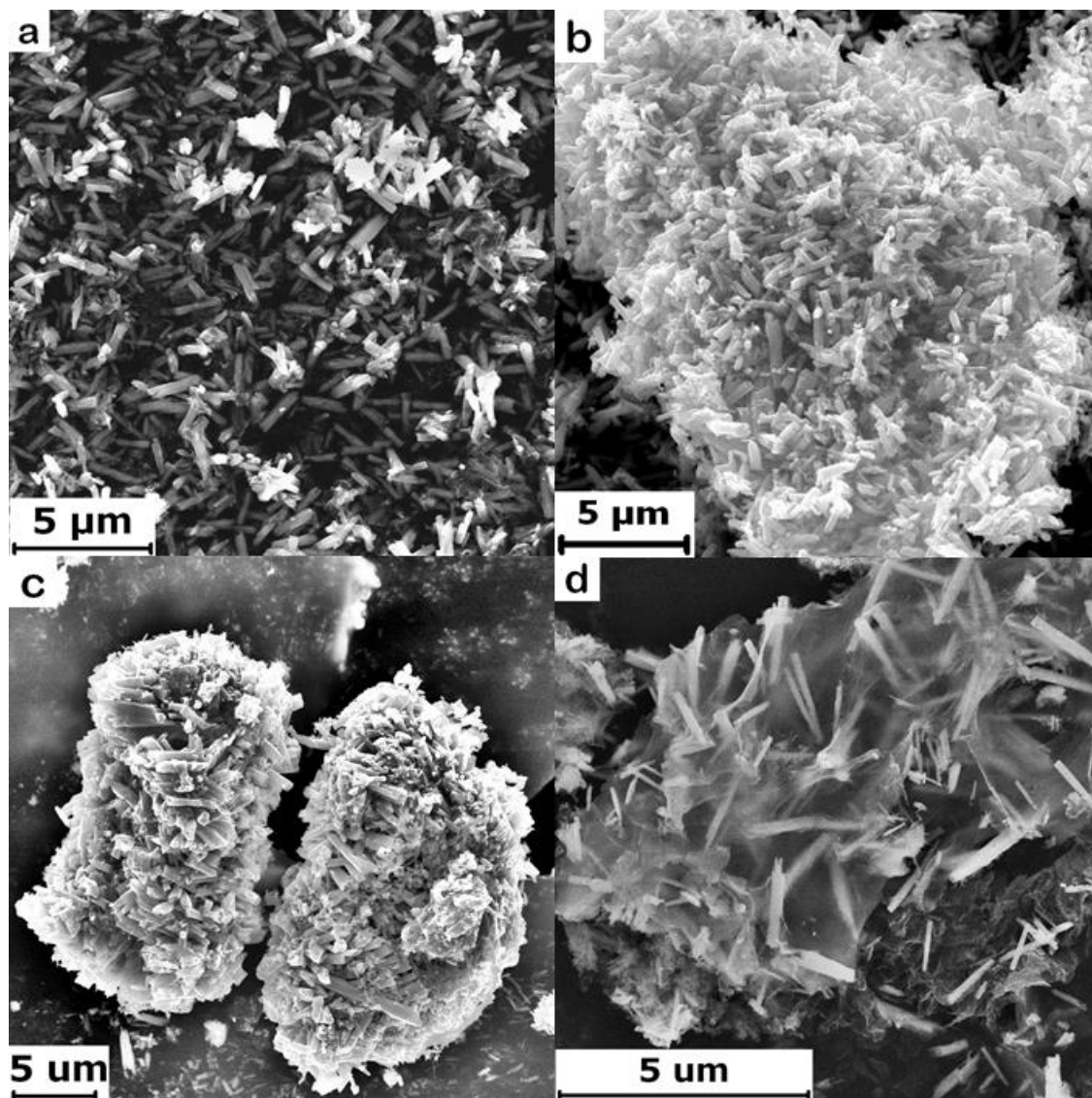


Figure 4.1: FESEM micrographs of pure ZnO (a), and ZnO/rGO composites with different concentrations of GO by 0.2 mg/ml (b), 0.6 mg/ml (c) and 1.0 mg/ml (d).

Figure 4.1 (a) shows in the absence of GO, ZnO appears in non-uniform shape with an average diameter and length of 90 nm and 3 μm respectively. The diameter and length of the ZnO rods were determined by using iSolution Lite software.

In the present of GO solution, after hydrothermal treatment the ZnO rod-like appears on the surface of reduced GO with similar morphological features but different level of density of ZnO rods. It was depending on the initial concentration of GO used. By increasing GO concentration from 0.2 mg/ml to 1.0 mg/ml, the density of ZnO nanorods decreased due to the same concentration of zinc ions complex (0.1 M) is diluted on GO sheets as the concentration of GO increased. At the highest GO solution concentration of 1.0 mg/ml, the graphene sheet is visibly adhered with narrow size of ZnO nanorods on both sides of the translucent sheets (Figure 4.1d). On the other hand, at the lower concentration of GO solution, the graphene sheet is fully enveloped by ZnO nanorods (Y.-L. Chen et al., 2011) (Figure 4.1b and 4.1c). These results indicate the formation of ZnO/graphene composites with tunable density.

4.2.2 High Resolution Transmission Electron Microscopy (HRTEM)

The highly dense distribution of ZnO nanorod that is fully decorated on the graphene sheets is supported by X-ray diffraction results. The shape and sizes of nanocomposite are also characterized by TEM as shown in Figure 4.2 (a) and (b).

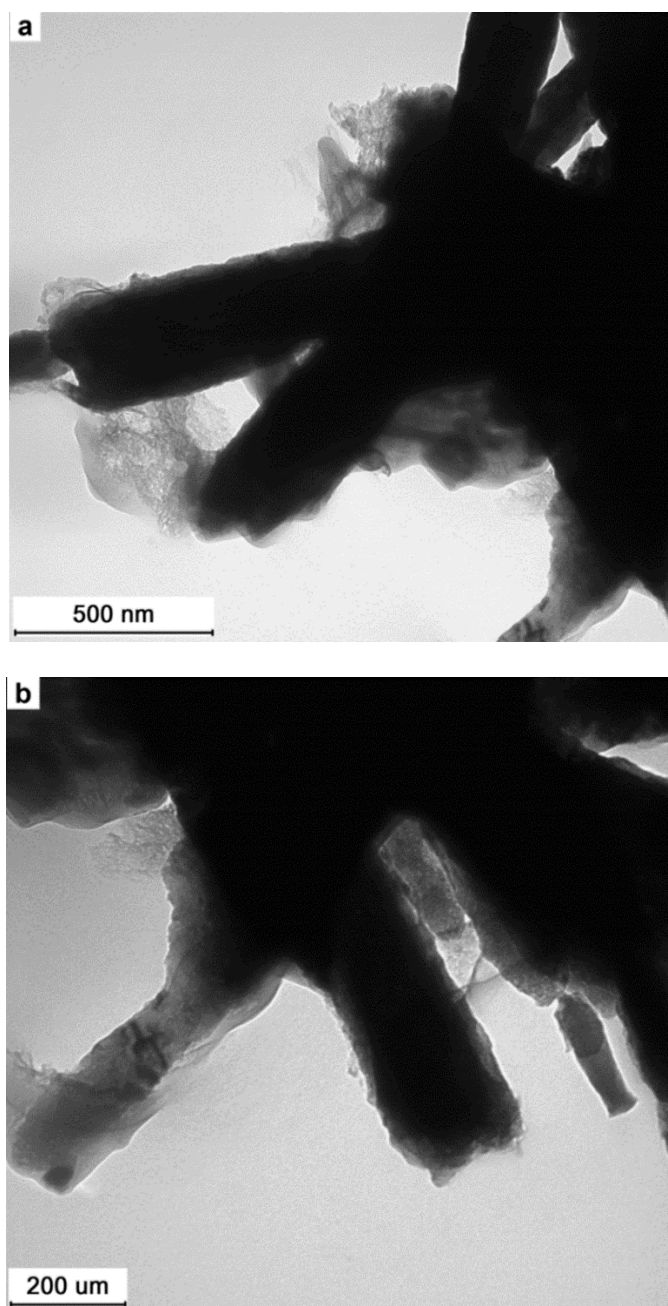


Figure 4.2: Images (a) and (b) show the rod-like shape of graphene/ZnO-1.0 nanocomposite at different magnification.

The TEM images show the ZnO that grown on the surface of graphene sheets were rod-like shapes with diameter of 50 to 200 nm with an average of 90 nm and similar average of length compared to pure ZnO rods. The transparent sheet that covers the rod-like ZnO represented graphene sheets.

The HRTEM was carried out to study the atomic arrangement in nanoscale of rod-like ZnO that was successfully synthesized.

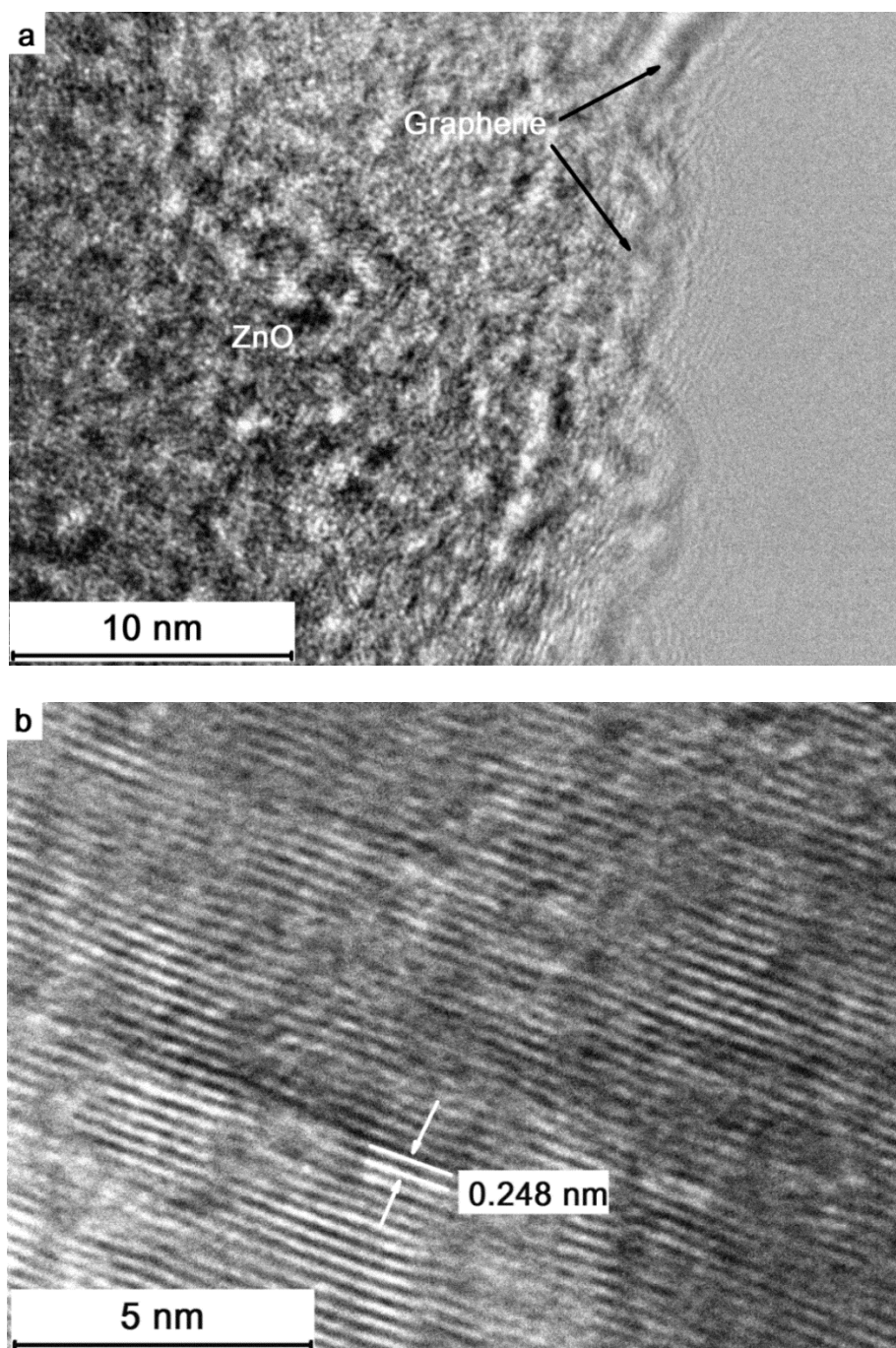


Figure 4.3: HRTEM of rod-like graphene/ZnO-1.0 nanocomposite (a) and image of high magnification (b).

Figure 4.3 displays the HRTEM image of rod-like graphene/ZnO-1.0 nanocomposite at high magnification. According to Figure 4.3 (a), it is observed that the surfaces of graphene sheets are decorated densely by ZnO rods. The HRTEM observation also exhibits the lattice spacing characteristic of graphene and rod-like ZnO particles, which confirms the homogeneous distribution of ZnO on the graphene sheets.

Figure 4.3 (b) reveals the highly crystalline features of ZnO rod on the reduced graphene sheets. The fringes with lattice spacing of 0.248 nm can be indexed to as the (101) plane of hexagonal ZnO.

4.2.3 X-ray diffraction (XRD)

XRD was employed to characterize the crystal structure of as-prepared GO and graphene/ZnO nanocomposite. The starting material GO was obtained from the oxidized graphite flake through simplified Hummer's method (Huang, Lim, Chia, Yarmo, & Muhamad, 2011) in order to exfoliate the GO sheets. In Figure 4.4, the XRD pattern of the GO is similar to the GO reported by other methods (Hassan et al., 2009). As shown in 4.4 (a), the graphite flakes exhibit the sharp diffraction peak at 26.7° contributed from the highly crystalline of graphene stacks. Whereas, the GO shows disappearance of the sharp graphite (002) peak at 26.7° and the appearance of a new lower intensity peak centered at 11.1° , corresponds to a d-spacing of 8.29 Å, which is attributed to the (001) reflection of GO. This result suggests the complete oxidation of graphite (S. Zhang et al., 2011) and the distance between the carbon sheets is increased due to the insertion of the inter-planar groups. Consequently, the GO sheets' thickness is increased because of the presence of covalently bound oxygen atoms and the displacement of the sp^3 -hybridized carbon atoms above and below the surface of the original graphene sheets (Hassan, et al., 2009).

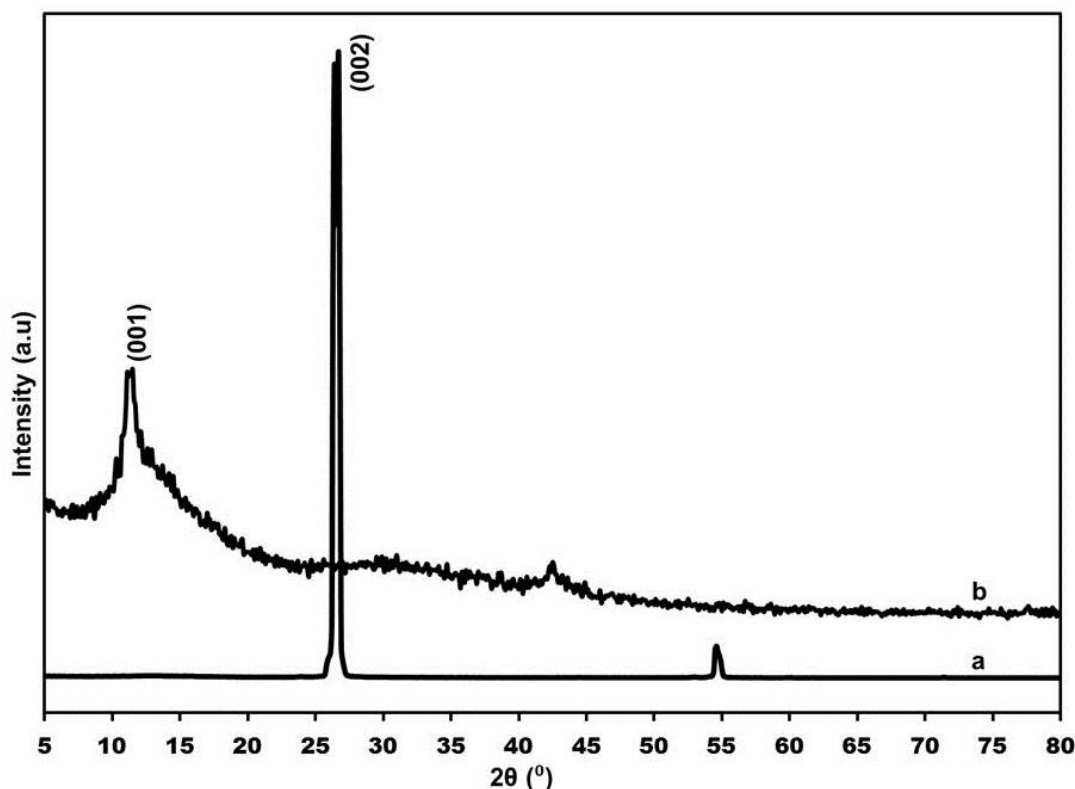


Figure 4.4: XRD patterns of graphite flake (a) and GO (b).

The XRD patterns of pure ZnO and three samples of graphene/ZnO nanocomposite shown in Figure 4.5 disclose sharp peaks indicating that all the samples were highly crystalline (B. Li & Cao, 2011). The reflection peaks at 31.7° , 34.4° , 36.2° , 47.5° , 56.6° , 62.8° , 66.1° , 67.8° and 69.0° are consistent with the hexagonal ZnO reflection peaks (JCPDS file no. 01-089-0510). No other reflection peaks, including the (001) GO reflections are observed, indicating the formation of high purity of the ZnO. As the concentration of GO increases, the intensity of the reflection peaks increased. The absence of the graphite (002) reflection peak at 26.7° indicates that the surface of the graphene sheets was fully covered with ZnO nanoparticles for all the samples (Y.-L. Chen, et al., 2011).

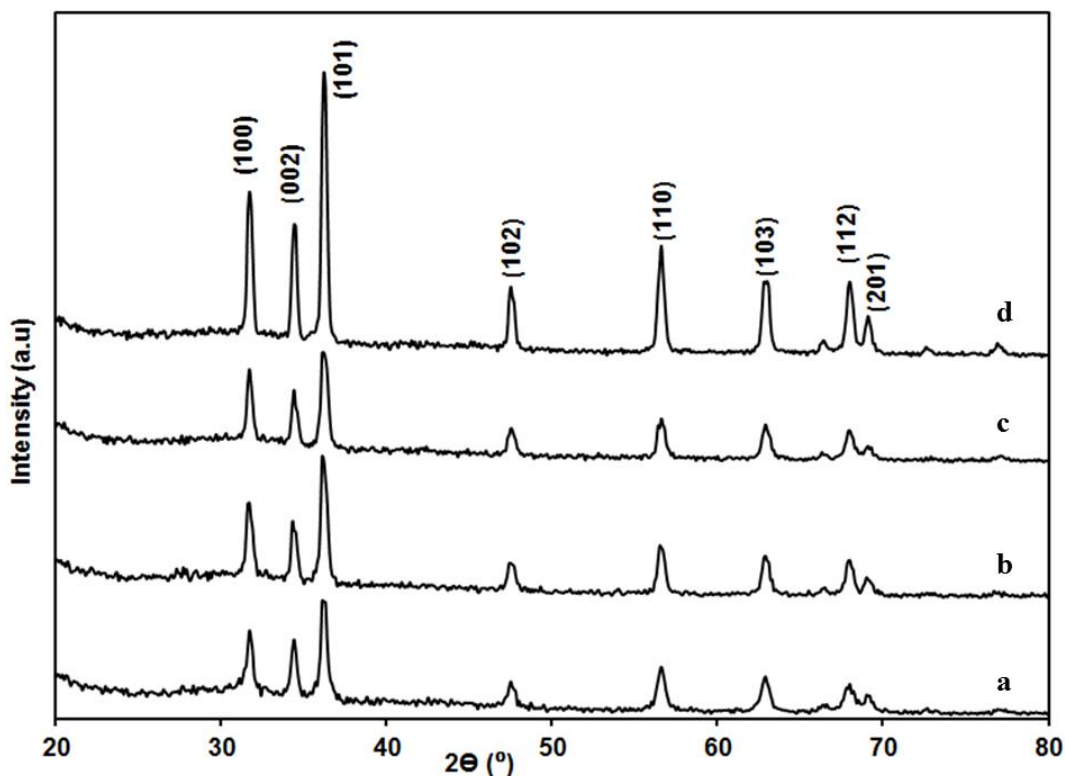


Figure 4.5: XRD pattern of pure ZnO (a), ZnO/graphene with 0.2 mg/ml GO (b), 0.6 mg/ml GO (c) and 1.0 mg/ml GO (d).

4.2.4 Ultraviolet-Visible Spectroscopy (UV-vis)

Figure 4.6 shows the UV-Vis absorption spectra of the as-synthesized GO and rGO. The GO sample has an absorption peak at 227 nm with sharp peak. The sharp peak represent $\pi \rightarrow \pi^*$ transition of aromatic C-C bonds (Kumar, 2003). After hydrothermal treatment, the rGO showed red-shift to higher wavelength at 264 nm. This is evident for the partial restoration of electronic conjugation network within the aromatic carbon structure.

While figure 4.7 displays the absorption spectra of ZnO and graphene/ZnO nanocomposites. The ZnO sample shows a strong absorption peak at 368 nm. The absorption spectrum of the nano-composites has two main areas of interest. Firstly, the absorption attributed to the carbon skeleton has shifted from the GO absorption at 227 nm to the absorption assigned to the π -plasmon of graphitic bond structure at 266 nm

(X. Wang et al., 2008). The shift provides evidence for the reduction of surface functional groups on the rGO sheets by hydrothermal treatment. Secondly, all the graphene/ZnO nanocomposites have absorption contributed by ZnO particles at 368 nm. With increasing GO concentration, the relative intensity of the carbon related absorption (peak at 266 nm) becomes stronger, indicating relatively to higher content of graphene.

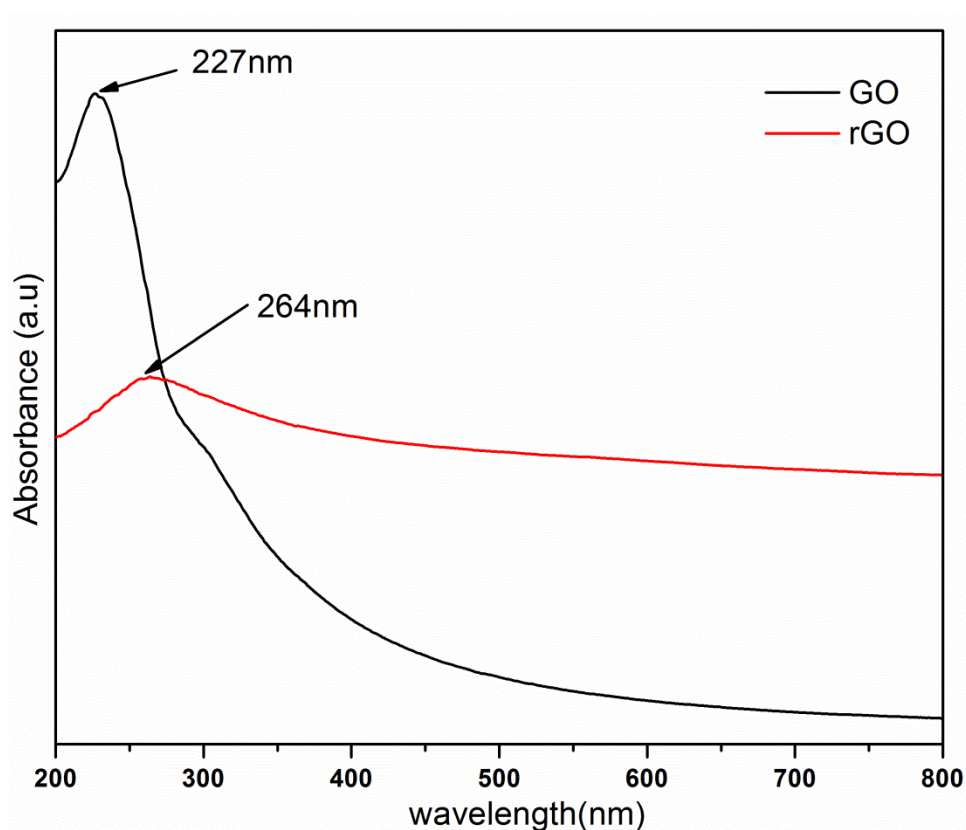


Figure 4.6: UV-vis spectra of GO (black line) and reduced GO (red line) after hydrothermal treatment.

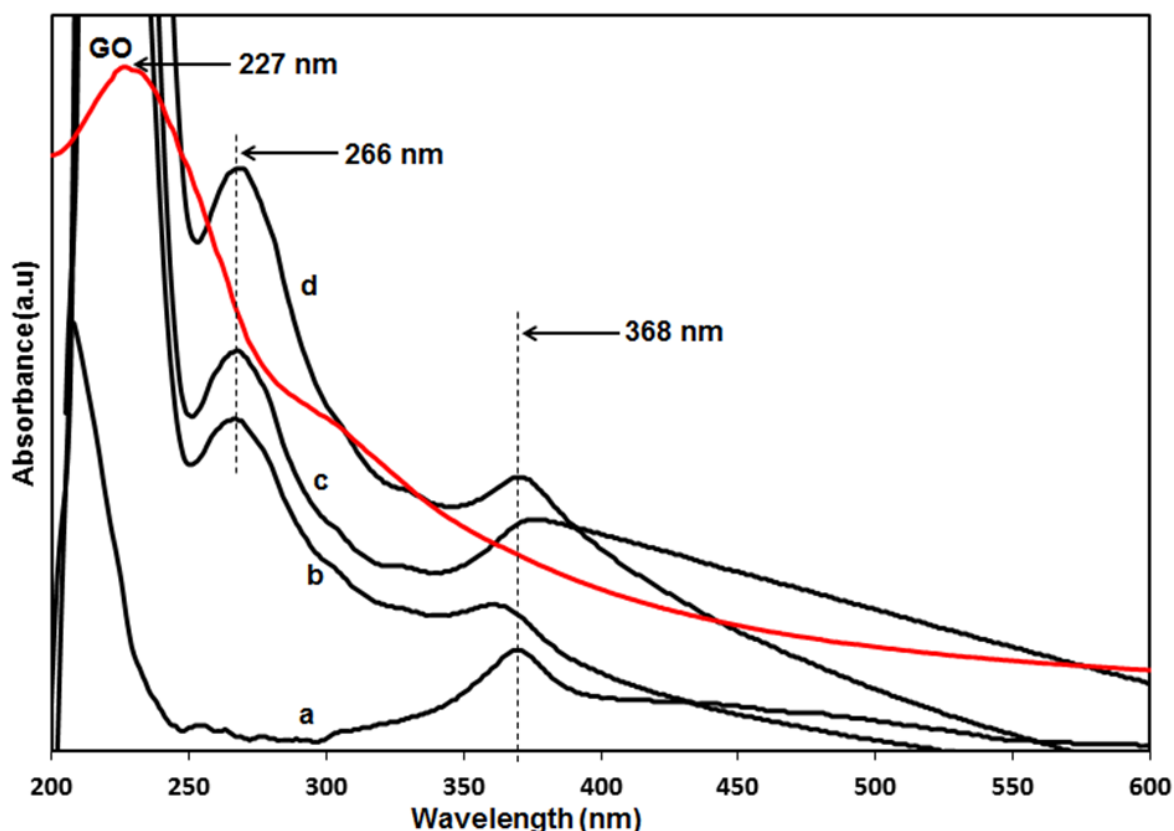


Figure 4.7: UV-vis spectra of (a) pure ZnO and composites with different concentrations of GO at (b) 0.2 mg/ml, (c) 0.6 mg/ml and (d) 1.0 mg/ml. The red line represent absorption peak for GO solution.

4.2.5 Thermogravimetric analysis (TGA)

In Figure 4.8 (a), TGA curve shows the mass loss of ZnO over the measured temperature range is very low, indicating the highly purity of the sample. There is a significant weight loss at 120 °C because of the loss of water absorbed on the surface. The TGA curve for GO shows there is a mass loss at 175 and 200 °C caused by the removal of oxygen-containing groups (Stankovich, et al., 2007). The weight loss of graphene at these temperatures is less than GO, suggesting that it is more thermally stable than GO. This observation strengthens the hypothesis that the hydrothermal process has significantly reduced the oxygenic functional groups on the surface of GO. As for the graphene/ZnO nanocomposites, there is a mass loss at >800 °C regardless of the concentration of GO used. This mass loss is due to the decomposition of the ZnO deposited on the graphene surface. It is well known that ZnO has a lower decomposition

temperature when it is heated in the presence of a catalyst such as carbon. In this case, graphene acted as a catalyst to reduce the thermal decomposition temperature of ZnO from 1900 °C to approximately 800 °C, which is similar to the reported value (Lv et al., 2010; Yousefi, Muhamad, & Zak, 2011). Based on the fact, it is expected that all the nanocomposites would diminish at 800 °C. However, graphene/ZnO prepared at the concentration of 0.2 mg/ml of GO solution, only experienced a total mass of 35 wt%, while the nanocomposites prepared at the concentration of 0.6 mg/ml and 1.0 mg/ml of GO solution had 55 wt% and 95 wt% of total mass losses, respectively. The remaining white powder for all the nanocomposites was confirmed to be ZnO by the XRD analysis (results are not shown). These results indicate the presence of free ZnO nanorods in the samples of nanocomposites that were not attached with graphene sheets. From the TGA results, we conclude that the graphene/ZnO nanocomposites formed using 1.0 mg/ml of GO solution had the highest amount of ZnO attached to the rGO sheets as the remaining ZnO in the crucible is less than 5 wt%.

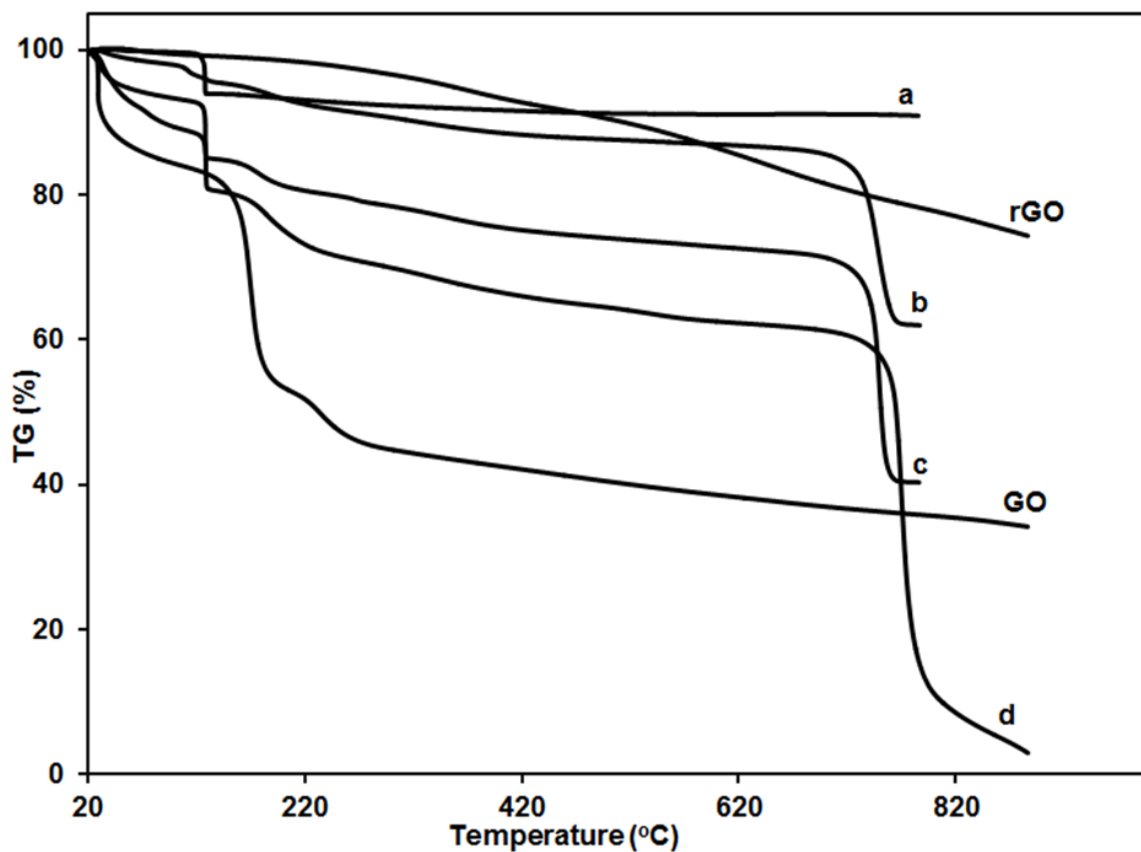


Figure 4.8: TG curves of (a) pure ZnO, and composites with different concentrations of GO at (b) 0.2 mg/ml, (c) 0.6 mg/ml and (d) 1.0 mg/ml.

4.2.6 Schematic for the synthesis process of nanorod-like graphene/ZnO nanocomposite (G/ZnO)

The schematic for the synthesis of graphene/zinc oxide nanorod-like nanocomposite is shown in the Figure 4.9.

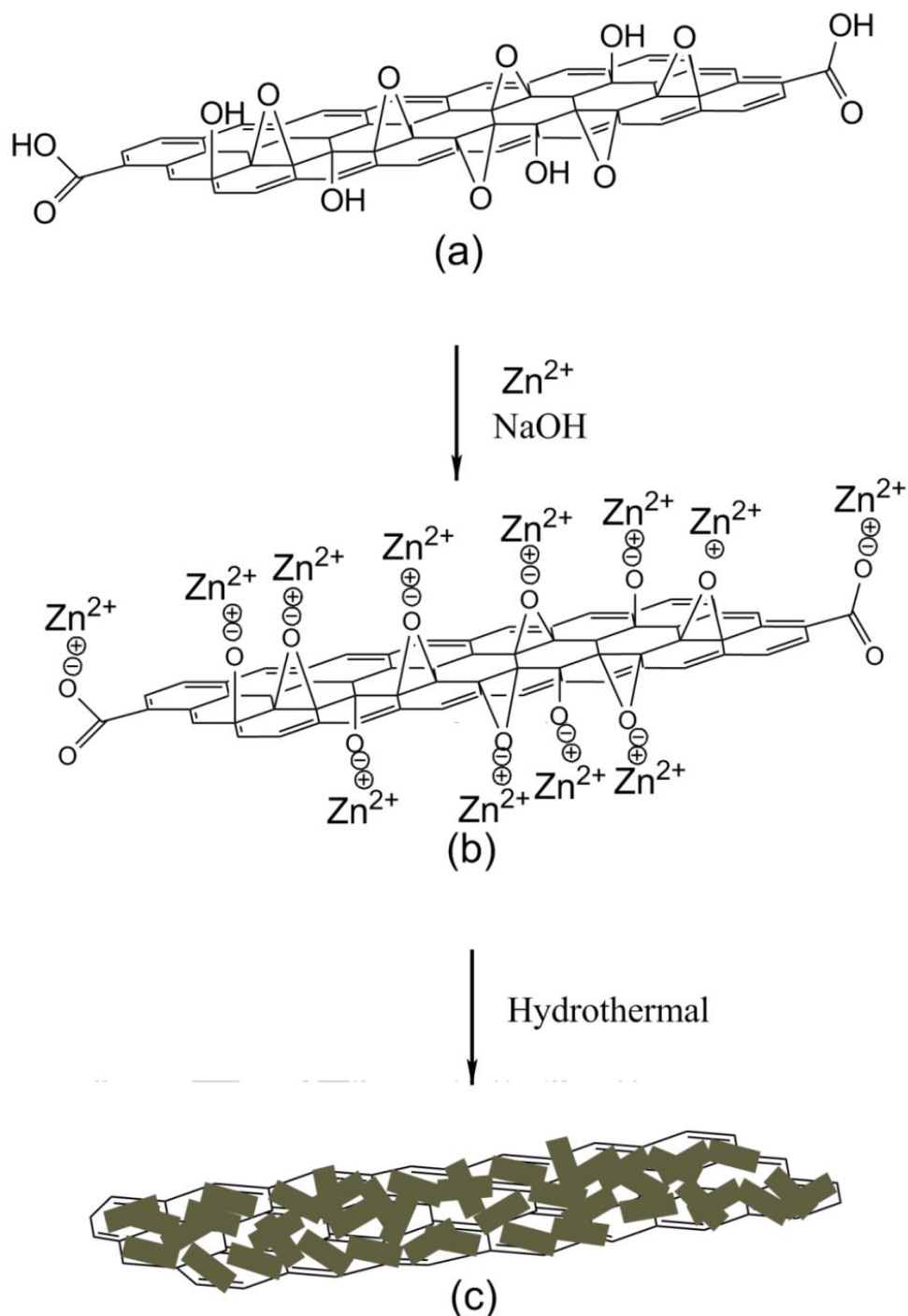


Figure 4.9: Schematic for the formation process of graphene/ZnO nanorod-like composite starting with GO in deionized water (a), after added zinc ions complex (b) and after hydrothermal treatment (c).

Figure 4.9 (a) shows the active group of $\text{C}=\text{O}$, $-\text{C}-\text{O}-\text{C}$ and $-\text{C}-\text{OH}$ that are attached to the surface of graphene oxide. These are advantages of GO solution to exist with large surface area and strong ion exchange capacity. This makes it possible for the formation of ZnO particles on the surface of GO. The GO also would be reduced during

the reaction since it consumes the same groups for the reaction. For the next stage, the NaOH is dropped to make heterogeneous nucleation to take place. So that, after it undergone hydrothermal treatment, the ZnO nanoparticles are finally formed on the surface area of the graphene sheets since Zn^{2+} ions have already bonded with carbons before. At the same time, the GO sheets also reduce itself to become graphene sheets during the reaction since it consumes the same group of reaction. This can be observed in the FESEM images (Figure 4.1).

4.3 Flower-like Functionalized Graphene/zinc Oxide (FG/ZnO) Nanocomposite

In this part, the starting material of the synthesis of the nanocomposite was replaced by functionalized graphene oxide (FGO). The FGO was chosen because of it is highly dispersible in water. Therefore, it can remain soluble in water and does not form aggregation. In order to get FGO, the GO was modified by introducing it with hydrophilic silane functional group from the N-(trimethoxysilylpropyl) ethylenediamine triaceticacid trisodium salt. These functional groups were subsequently fabricated to graphene oxide sheets and make it more stable in the water in term of solubility.

4.3.1 Parameter

Optimum parameter was obtained from the previous part of the synthesis of nanorod-like graphene/ZnO nanocomposite. The optimum concentration at 1.0 mg/ml was used for the synthesis of nanoflower-like functionalized graphene/ZnO nanocomposite. The other conditions for preparation were remaining constant.

4.3.2 Experiment results

The surface morphology, structure and composition of samples were characterized by using X-ray diffractometer (XRD, Philips D5000) using Cu K α radiation ($\lambda = 1.4506 \text{ \AA}$), X-Ray photoelectron spectroscopy (XPS), field emission scanning electron microscope (FESEM, FEI Nova NanoSEM 400 operate at 10.0 kV), high-resolution transmission electron microscope (HRTEM, JOEL JEM 2100F) and Renishaw Raman spectrometer (Renishaw inVia Raman) with a 514 nm as excitation source. The optical properties were studied using a Shimadzu UV-VIS spectrophotometer over the spectral region of 190-900 nm. Photoluminescence (PL) spectra were recorded using a Renishaw florescence spectrophotometer with a 325 nm excitation line.

The prepared functionalized graphene (FG) and functionalized graphene/Zinc oxide (FG/ZnO) nanocomposite are shown in Figure 4.10.

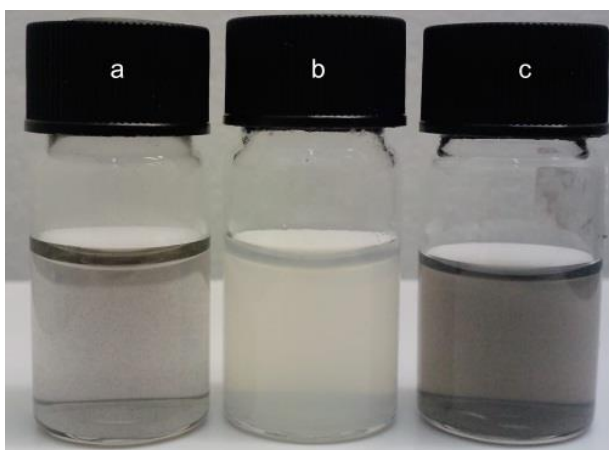


Figure 4.10: Figure shows the FG (a), star-like ZnO (b) and FG/ZnO-1.0 nanocomposite (c) that dispersed in the deionized water straight away after hydrothermal treatment.

The star-like ZnO (b) that was prepared at pH 10 displays a good dispersion in the deionized water. While the FG and nanocomposite showed some floating particles in the deionized water suggesting the appearance of hydrophobic characteristics of the

graphene sheet after hydrothermal treatment. The change of color from golden brown to black was observed for FG (a) and FG/ZnO-1.0 nanocomposite (c) after reduction by the hydrothermal method.

4.3.2.1 X-Ray Diffractometer (XRD)

Figure 4.11 shows the XRD patterns of FG, ZnO and FG/ZnO-1.0 nanocomposite respectively. All the diffraction peaks of nanocomposite are matched with the standard data for hexagonal-structured ZnO (JPCDS file no. 01-089-0510) (Figure 4.11c). The appearance of a broad diffraction peak at 25.1° for rFG suggests a complete reduction of FGO and exfoliation of graphene layers (Hassan, et al., 2009; Yan et al., 2010) (Figure 4.11a). This phenomenon is attributed to the removal of oxygen functional groups after the hydrothermal process. The weak diffraction peak at 25.1° in the nanocomposite indicates the complete reduction as experienced in FG pattern. In addition, we noted that the relative intensity of the nanocomposite is higher than the relative intensity of standard ZnO, which indicates that the prepared nanoflower-like ZnO grew along the (002) crystal plane direction.

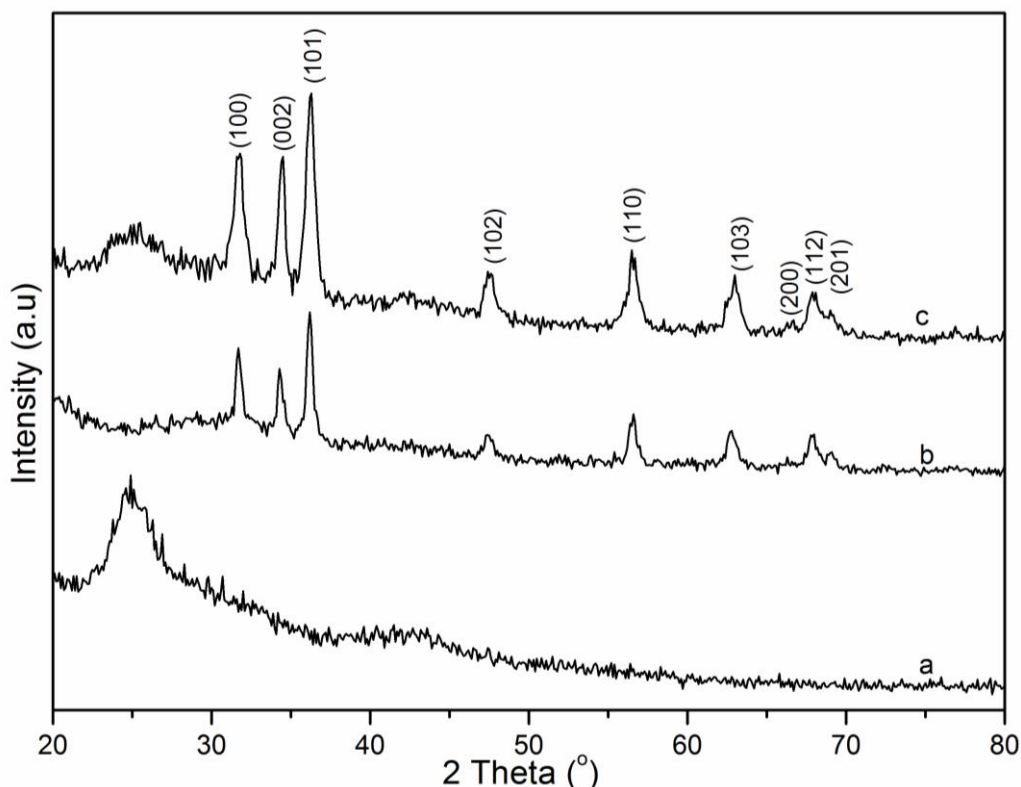


Figure 4.11: XRD patterns of FG (a), ZnO (b) and FG/ZnO-1.0 nanocomposite (c).

4.3.2.2 X-Ray Photoelectron Spectra (XPS)

Further evidence for the composition of the rFG/ZnO nanocomposite was obtained by the X-ray photoelectron spectra (XPS). The XPS peaks were deconvoluted by using Gaussian components, after a Shirley background subtraction. In the C_{1s} XPS spectra of GO (Figure 4.12), it clearly shows a considerable degree of oxidation with three main components that correspond to carbon atoms in different functional groups: the nonoxygenated ring C appeared at 284.1 eV, the C-O epoxy at 286.3 eV and the carboxylate carbon C=O appeared at 287.8 eV. The small peak at 289 eV indicates to C-OH group.

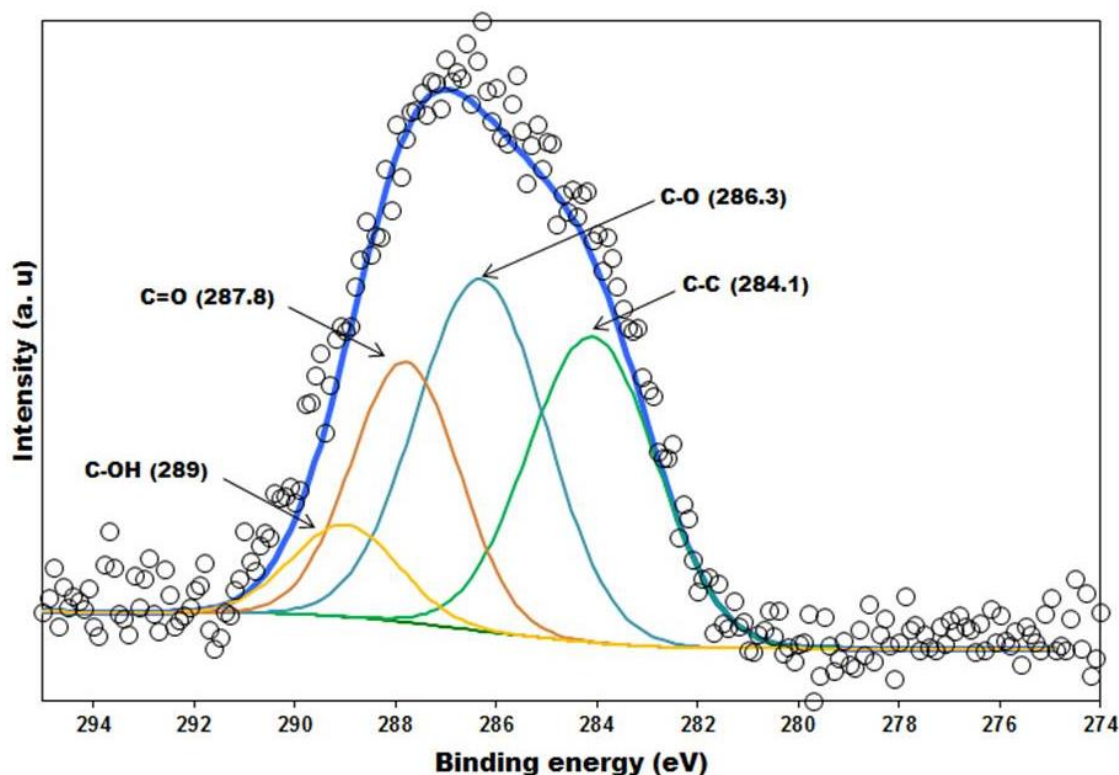


Figure 4.12: Figure shows XPS of graphene oxide (GO) as-prepared by simplified Hummer's method.

After hydrothermal treatment for 24 hours at temperature 180 °C, the nonoxygenated C-C become prominent as shown in the Figure 4.13 of XPS spectra of reduced functionalized graphene. The low intensity peak of C-O and C=O groups are observed in FG because of reduction during hydrothermal treatment.

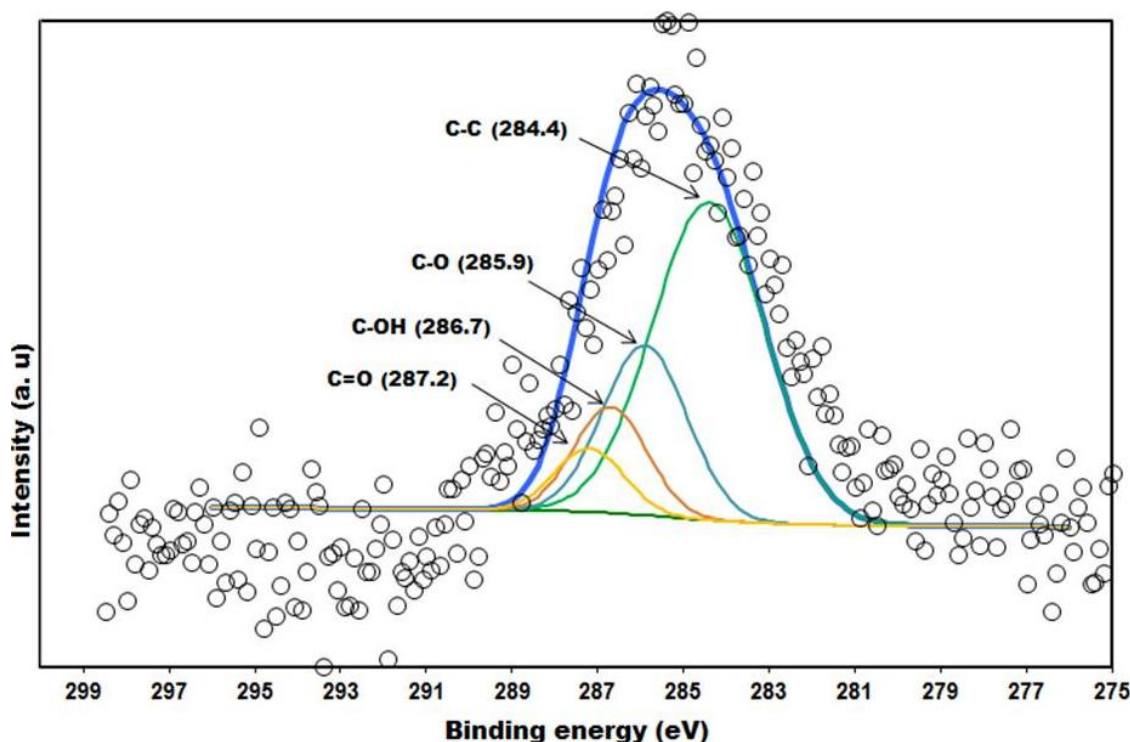


Figure 4.13: XPS of functionalized graphene (FG) after hydrothermal treatment.

For the FG/ZnO-1.0 nanocomposite, the binding energy of the C-Zn, C-C or C=C bonds and carbonyl functional groups were evaluated about 281.8 eV, 284.5 eV and 286.2 eV respectively. The XPS spectrum shows the nonoxygenated C-C are prominent which attributed to the interaction between zinc ions with the rich carboxyl group from N-(trimethoxysilylpropyl) ethylenediamine triacetic acid sodium salt that had taken place (Figure 4.14). Presence of the C-Zn functional groups provided formation of Zn–O–C carbonaceous bonds in the functionalized graphene–ZnO nanocomposites, consistent with the results reported by Liu et al. (X. Liu et al., 2005).

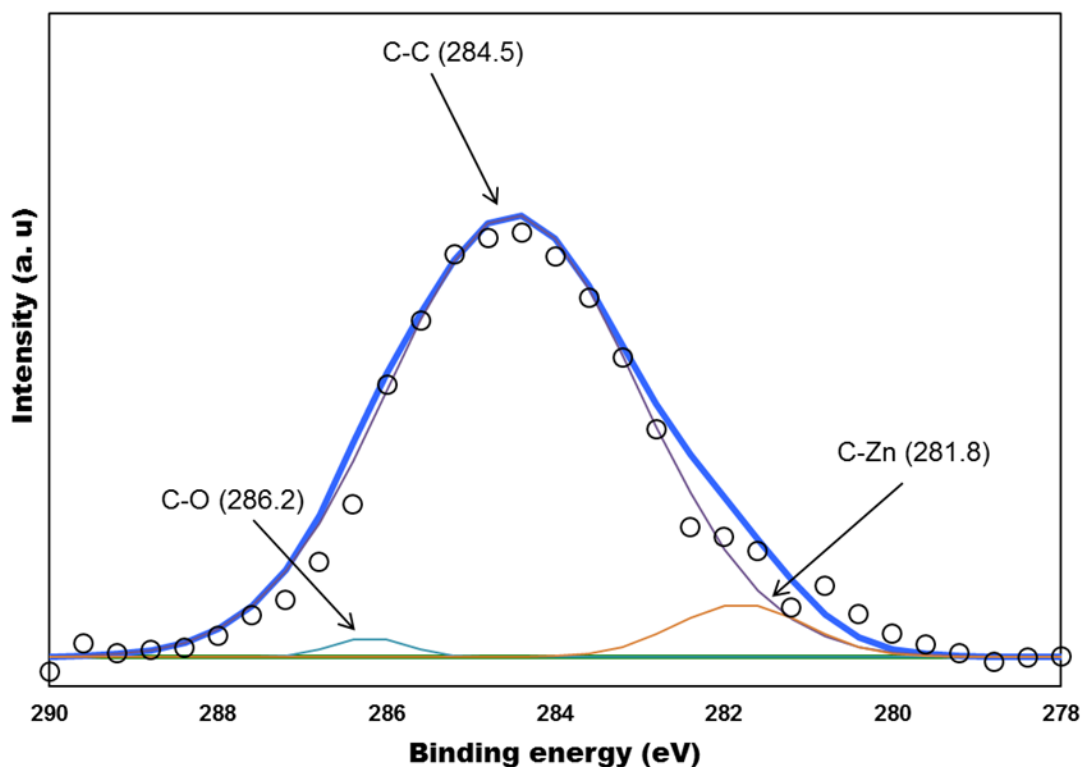


Figure 4.14: XPS of FG/ZnO-1.0 nanocomposite.

4.3.2.3 Field Emission Scanning Electron Microscope (FESEM)

Before we started to prepare the combination of composites, we studied the morphology and structure of pure ZnO first. This can be made by synthesizing the ZnO at different pH conditions since the growth of ZnO are strong depending on the pH value. The morphologies and microstructures of the obtained ZnO and nanocomposite products were characterized by FESEM observation after hydrothermal treatment. The panoramic FESEM images of pure ZnO powder exhibit a highly dense growth of ZnO with different architecture at different pH value. These architectures were obtained after hydrothermal treatment. It is because of the growth and morphology of ZnO is influenced by pH of the solution after undergone the hydrothermal treatment. At different pH value ranging from 9 to 12, the changes of ZnO morphology can be clearly observed. A baton-like shape of ZnO particles are observed at pH 9 (Figure 4.15a). A star-like shape of ZnO particles having diameter in the range 1 to 2 μm are observed at

pH 10 (Figure 4.15b). At pH 11, the thin flower-like ZnO are observed with the diameter 5 μm (Figure 4.15c). As the pH increases to high pH value, the structure of ZnO tends to become rod-like shape with smaller diameters (Figure 4.15d).

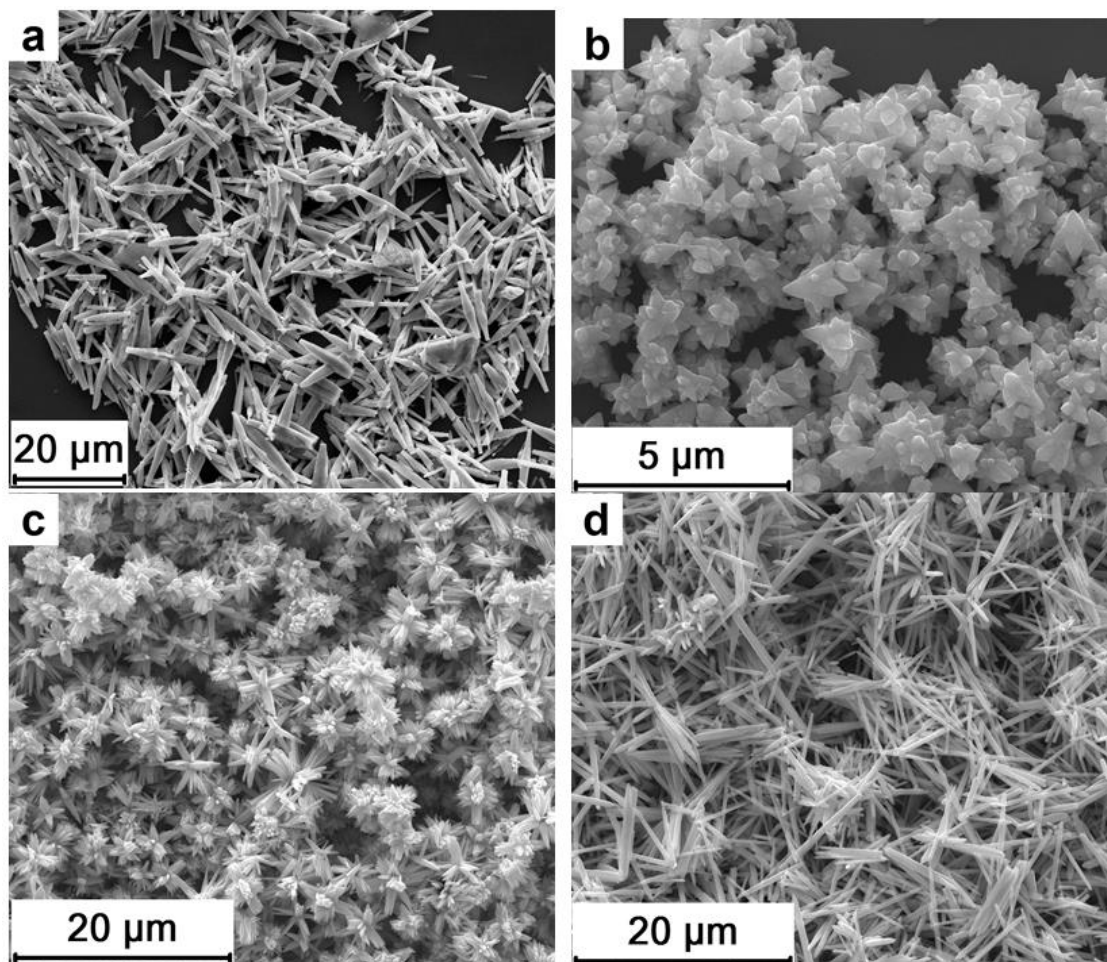


Figure 4.15: FESEM images of ZnO pH 9 (a), ZnO pH 10 (b), ZnO pH 11 (c) and ZnO pH 12 (d).

The chemical composition of the synthesized ZnO powder was examined by mapping analysis. From the mapping analysis of ZnO particles at pH 9 clearly proves that it is pure ZnO with no impurities (Figure 4.16).

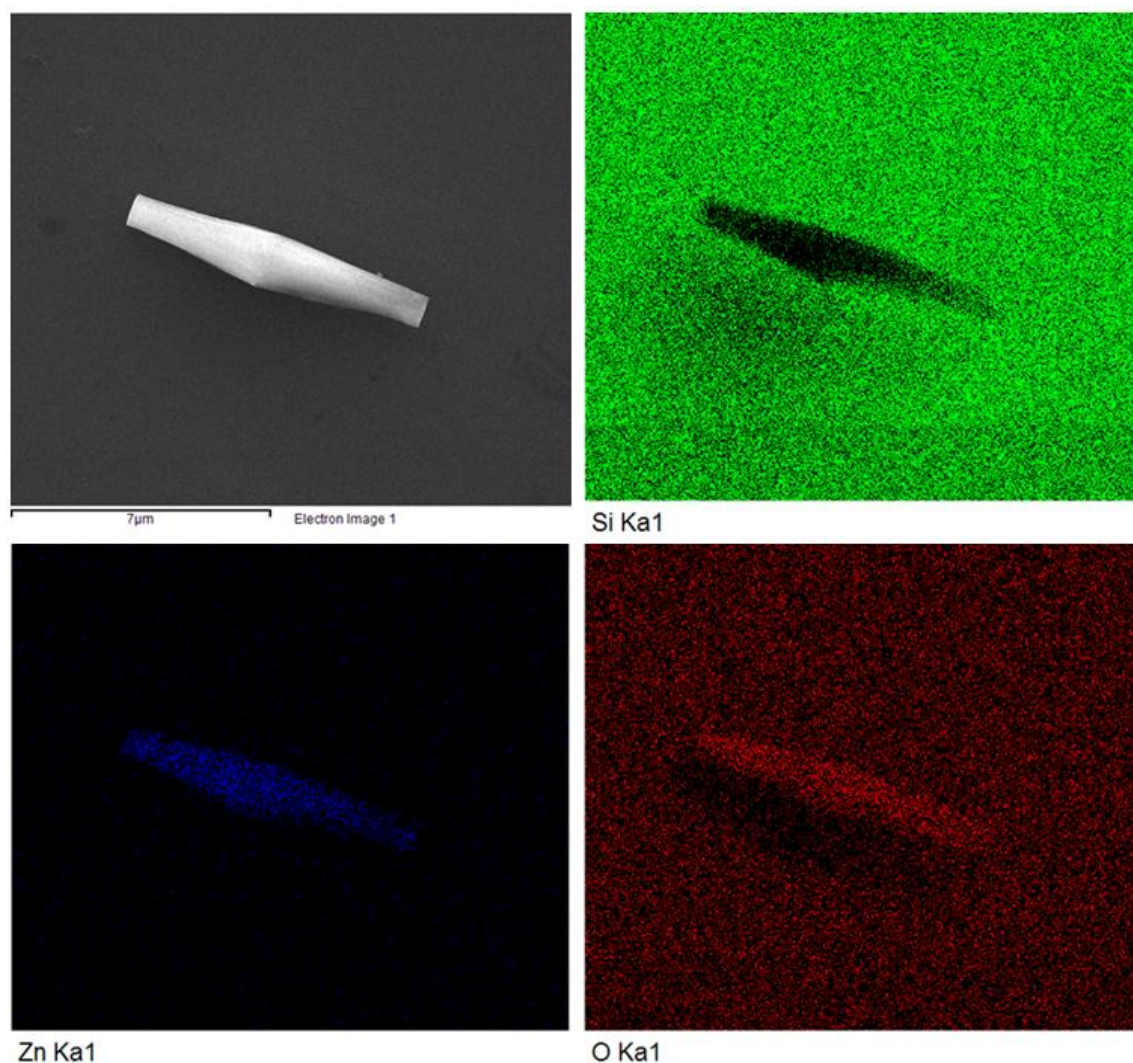


Figure 4.16: Figure shows the mapping analysis of pure baton-like ZnO at pH 9.

The green colour of mapping analysis represents the silicon composition since silicon dioxide was used as substrate. As displays, there is no green colour appeared in the tested sample. Whereas, the blue colour that represents the composition of zinc revealed in this sample. Also, we can observe the red colour that represents the composition of oxygen is dominant on the sample and substrate. These results indicate the pure ZnO was successfully synthesized via the simple hydrothermal method.

As demonstrated in many colloidal experiment (Everett, 1988) for the preparation of colloidal suspensions of graphene sheets without help of stabilizers or surfactant have been reported. The colloidal stability of an electrostatically stabilized dispersion is strongly dependent on pH, the electrolyte concentration and the content of

dispersed particles (D. Li, 2008). Therefore, by controlling these parameters, we now find that, the chemically converted graphene sheets are able to form stable colloid via electrostatic stabilization. The remaining metal salts and acids in the starting material of GO critically can neutralize the charges on the GO sheets, thus destabilize the resulting dispersion.

In order to maintain maximal charges density on the GO sheets, the basic conditions with pH 10 is needed (S. Park & Ruoff, 2009). The ammonia solution can be used to adjust the pH of the solution, and then it can be easily removed after the graphene sheets are processed into composites. By adjusting the pH of the solution to pH 10 can convert neutral carboxylic groups to negatively charge which is carboxylate groups. These negatively charge group will repel each other and do not form agglomeration (D. Li, 2008). It was suggested that, these carboxylic groups interact with the Zn ions and consequently form a complex through electrostatic interaction. Finally, the Zn ions will totally transform into ZnO on the FGO sheets form flower-like ZnO nanostructures. Moreover, the Zn ions with pH 10 are resulting to the smallest diameter (~500 nm) of ZnO nanoflower that can be grown on the FGO sheets.

The FESEM of flower-like rFG/ZnO nanocomposite shows random distribution of ZnO particles decorated on the graphene sheets, where they are found on the both sides of the rFG sheets (Figure 4.17). At a higher magnification, the particles looked flower-like and have an average size of 0.5 μm , which is smaller than that of pure ZnO (Figure 4.15b). This proves that the shape and size of ZnO particles are dependent on the presence of FGO. The surface of FGO contains unreacted hydroxyl groups attached to the hexagonal basal plane and large number of functionalized carboxylic groups from N-(trimethoxysilylpropyl) ethylenediamine triacetic acid sodium salt. These carboxylic groups interact with the zinc cations and form a complex through electrostatic

interaction. In the hydrothermal condition, zinc ions are formed on the surface of FGO with flower-like nanostructures.

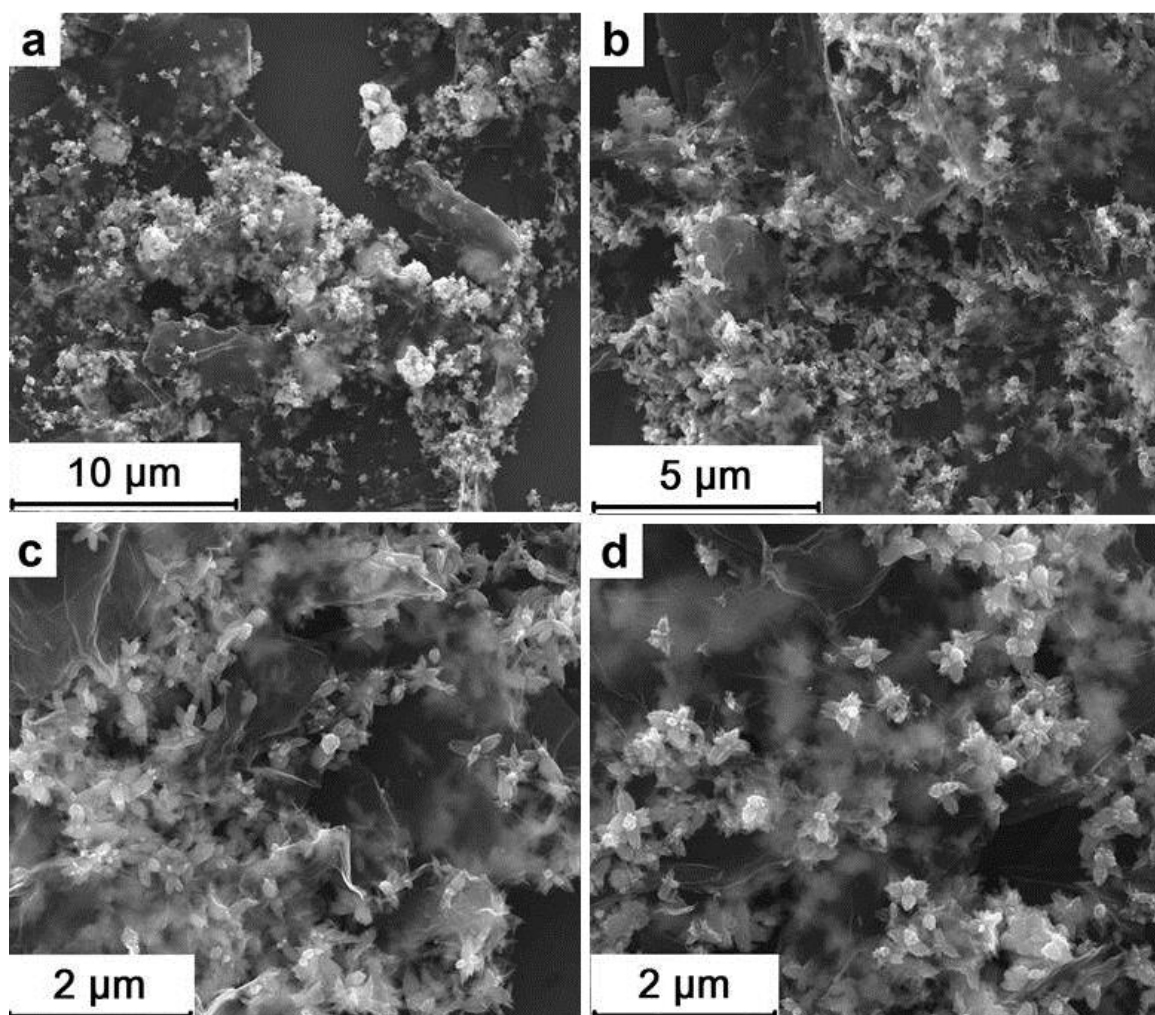


Figure 4.17: FESEM images of nanoflower-like FG/ZnO-1.0 nanocomposite with 10 000 (a), 20 000 (b), 40 000 (c) and 80 000 (d) magnification power.

Usually, there are two interactions that involved during reaction process between FGO sheets, electrostatic interactions and van der Waals interactions. If the electrostatic repulsion is dominant, then the coagulation will take place and well-dispersed in the system. On the contrary, if Van der Waals dominates, the irreversible coagulation of exfoliation FGO will occur during the reaction. At lower concentration of FGO-mixed with 0.1 M of zinc ions during initial reaction stage, resulting in coagulation of the exfoliated FGO. The coagulation of FGO occurs during the hydrothermal reaction due

to negatively charges on reduced FGO are partially or fully neutralized by zinc ions. As a result, fewer FG sheets present in the resultant composites as shown in FESEM images (Figure 4.17 a-b). With the increment of the concentration of FGO solution up to 1.0 mg/ml, the electrostatic repulsion interaction between the charged FGO gradually increases and finally overcomes the Van der Waals interaction. Therefore, the well distribution of ZnO on the FG sheets can finally be obtained as shown in Figure 4.17d.

4.3.2.4 Transmission Electron Microscope (TEM)

To further analyze the morphology features of ZnO grown on FG sheets, we employed the TEM observation for FG/ZnO-1.0 nanocomposite. The TEM images clearly display the flower-like ZnO were growth on the both side FG sheets. This indicates that even after a long time sonication during the preparation of TEM specimen, ZnO particles are still attached on the FG sheets with a high density (Figure 4.17c), suggesting a strong interaction between ZnO particles and FG sheets. Further study by magnifying the image exhibits a flower-like petal with a length of 467.76 nm and diameter of 126 nm (Figure 4.18d).

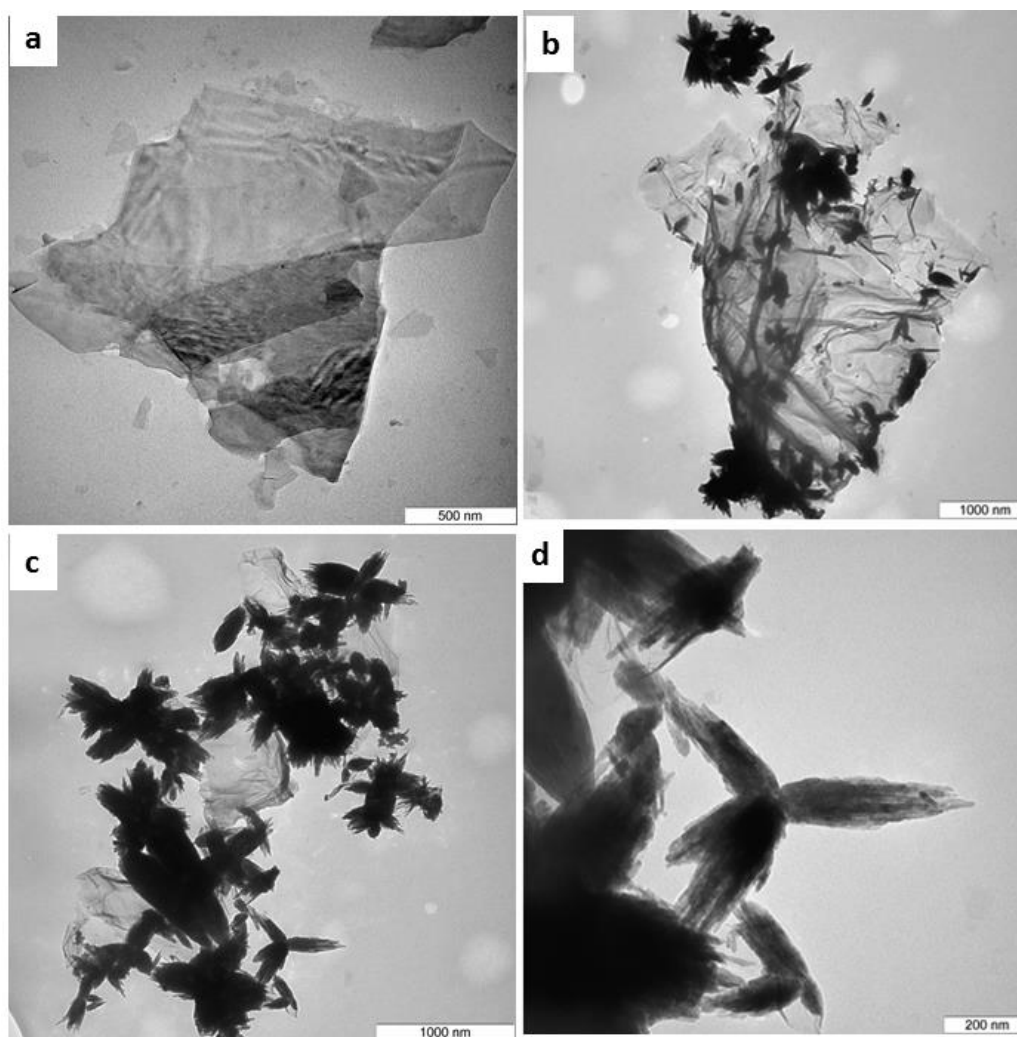


Figure 4.18: TEM images of FGO and rFG/ZnO-1.0 nanocomposite.

4.3.2.5 High Resolution Transmission Electron Microscope (HRTEM)

The high resolution transmission electron microscope (HRTEM) analysis was performed on the as-synthesis flower-like ZnO/rFG nanocomposite to determine their atomic arrangement in nanometer domain. Fig. 4.19 shows the lattice fringes with an interplanar distance of 0.281 nm that can be assigned to the (100) plane of the hexagonal ZnO (J. Wu, et al., 2010).

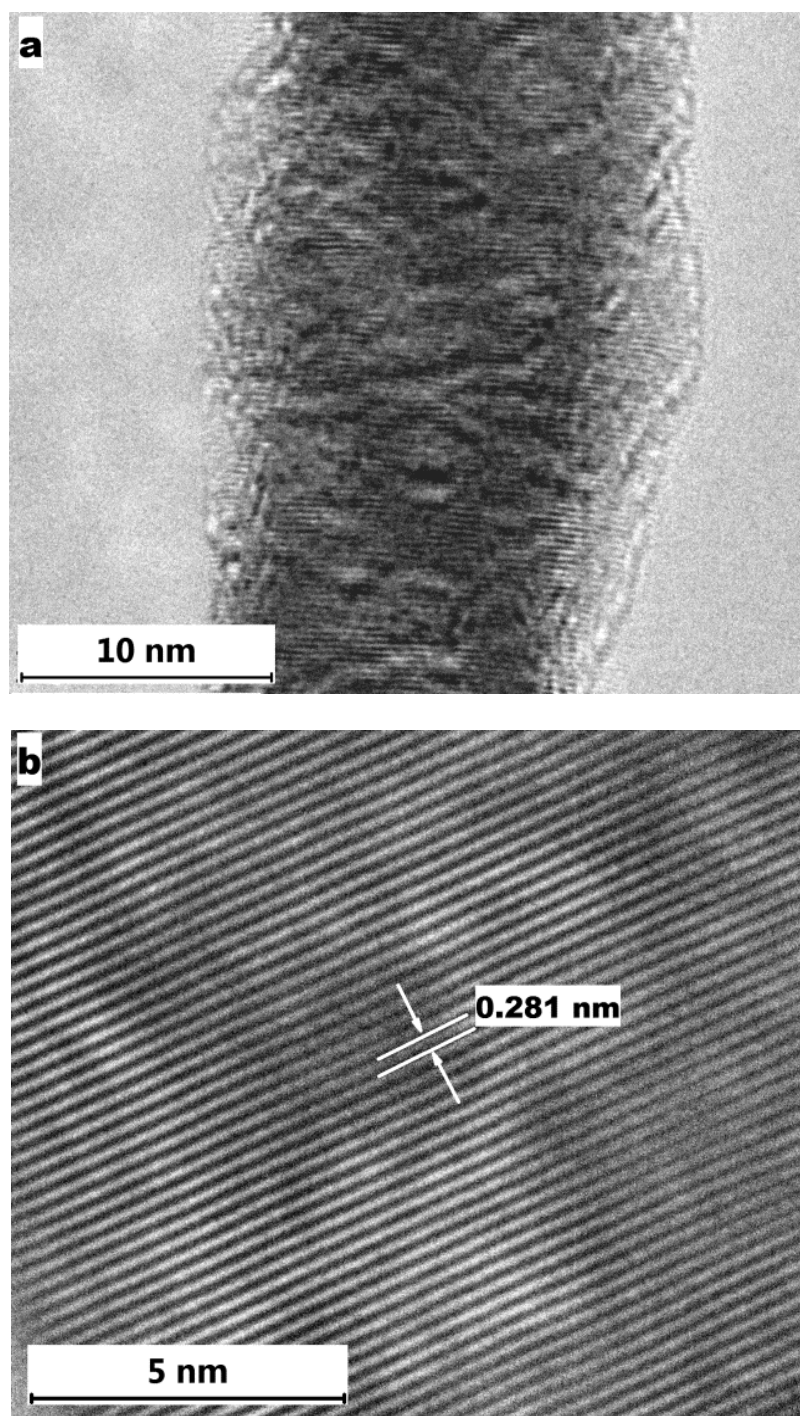


Fig. 4.19: HRTEM image of flower-like FG/ZnO nanocomposite (a) and HRTEM of nanocomposite at higher magnification (b).

4.3.2.6 Raman Spectroscopy

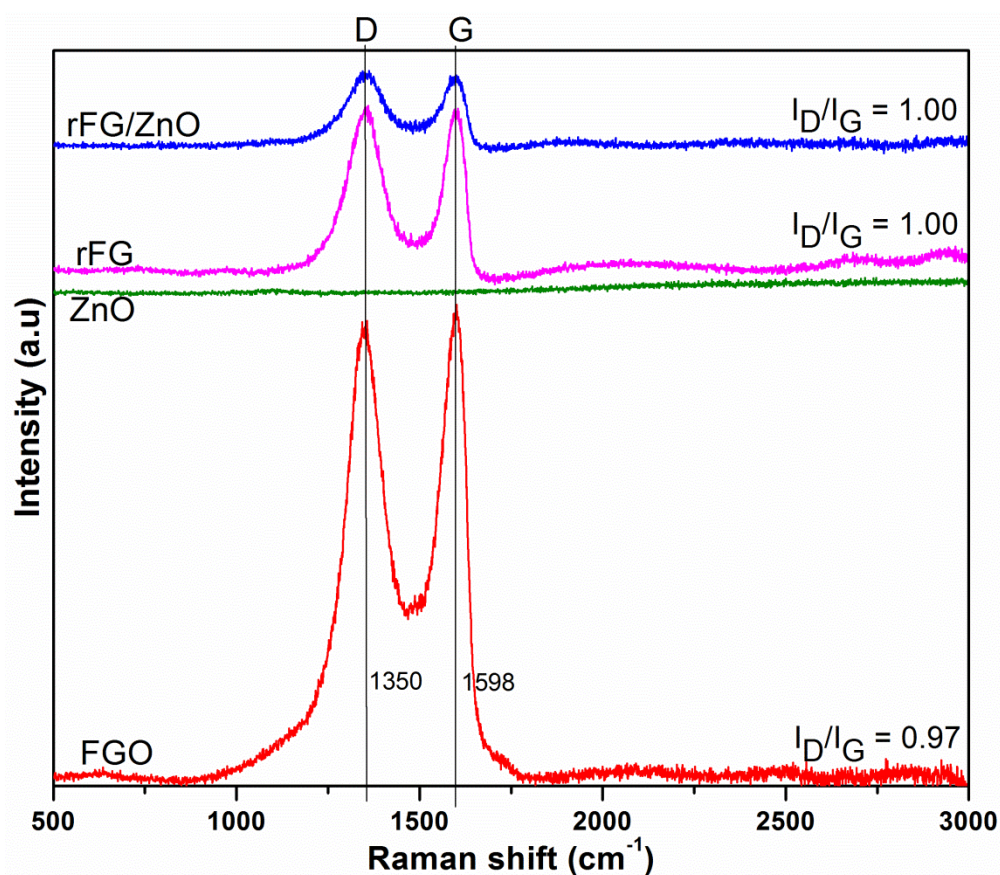


Figure 4.20: Raman spectra of FGO, FG, ZnO and nanocomposites.

Figure 4.20 displays the Raman spectra of FGO, FG, ZnO and FG/ZnO-1.0 nanocomposites respectively. The Raman spectra of FGO are dominated by two intensity peaks of carbon materials at 1357 cm^{-1} and $\sim 1600\text{ cm}^{-1}$. The peaks are referred as D-band corresponds to the breathing mode of k-point phonon of A_{1g} symmetry and G-band assigned to the E_{2g} phonon of sp^2 bonds of carbon atom, respectively. These D and G-band are the defect-related after reaction process. The intensity of the G-band indicates the increases number of layers as proven by FGO. After the reduction to FG, the D-band shifted to 1350 cm^{-1} but G-band slightly shifted to lower frequency region (1598 cm^{-1}), confirming the reduction occurred (Kudin et al., 2007). It should be noticed that no obvious peaks contributed from ZnO particles are observed in the composites, which due to the lower amount and concentration of zinc ions used. The Raman spectra

of the composites show interesting observations. From the spectra, we can see that the D-band and G-band are shifted to the lower frequency region as the concentration of FGO increases. These can be related to the composition of ZnO in the composite that helped the reduction of FGO due to its chemical interaction between FGO sheets before the reduction process. The second-order band (2D-band) is observed in the region of 2700 cm^{-1} (Graf et al., 2007; Pimenta et al., 2007). The 2D-band is distinguished by the layer of graphene either bi- or few-layer sheets. But this Raman spectra, it is noticed that there is no significant peak that appears at that region. The ratio of the intensities of the D and G band (I_D/I_G) is related to the in-plane crystallite size of few layer graphene sheets (Pimenta, et al., 2007). According to the Raman spectra of the composites, the intensity ratio of the D peak to G peak is increased as compared to the FGO. This suggests the decrease in average size of sp^2 domain upon the reduction of FGO to FG (Xiang, Yu, & Jaroniec, 2011; K. Zhou, Zhu, Yang, Jiang, & Li, 2011).

4.3.2.7 Fourier transformed infrared spectra (FTIR)

The FTIR spectra of GO, FGO and FG samples are presented in figure 4.21. The characteristic peaks of GO, including O-H stretching at 3400 cm^{-1} , C-OH deformation at 1400 cm^{-1} and the peak around 1020 cm^{-1} are due to C-O (C-OH and C-O-C merged), which were clearly observed in the spectrum. Functionalization with N-(trimethoxysilylpropyl) ethylenediamine triacetic acid sodium salt forms new chemical bonds on GO thus, several new peaks appeared in spectrum of FGO as compared to GO. The appearance of two new bands at 2925 and 2858 cm^{-1} are assigned to the stretching vibration of the N-(trimethoxysilylpropyl) ethylenediamine triacetic acid sodium salt methylene groups. The increased intensity of the broad peak at 2925 and 2858 cm^{-1} in FGO is due to the increased number of ionized carboxyl groups. The band at 1218 cm^{-1} is associated with the C-N vibration of N-(trimethoxysilylpropyl) ethylenediamine

triacetic acid sodium salt silane molecules. The peak intensity of C-OH and C-O-C groups at 1400 and 1020 cm^{-1} , respectively were decreased in the FGO suggesting the reaction of N-(trimethoxysilylpropyl) ethylenediamine triacetic acid sodium salt with GO. The successful formation of Si-O-C bonds between GO and N-(trimethoxysilylpropyl) ethylenediamine triacetic acid sodium salt is confirmed by the appearance of a peak at 694 cm^{-1} . A low intense peak at 923 cm^{-1} is observed because of the presence of unreacted Si-OH groups, which have completely disappeared after hydrothermal reduction forming a new peak of Si-O-Si at 1025 cm^{-1} which suggests the self-condensation of Si-OH groups.

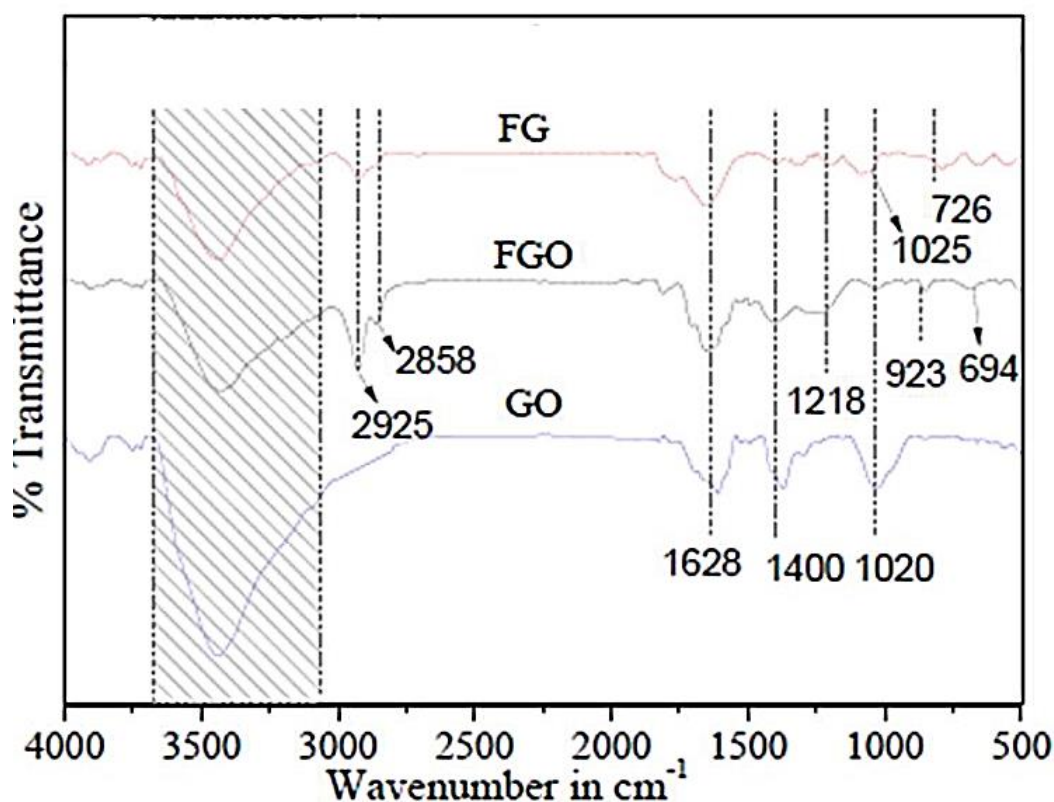


Figure 4.21: FTIR of GO, FGO and FG samples.

4.3.2.8 Ultraviolet visible spectroscopy

Optical absorbance spectroscopy measurement was performed by using Shimadzu UV-VIS spectrophotometer. For UV-visible measurements, the samples were

dispersed in deionized water by sonication for 5 to 10 minutes. Figure 4.22 shows the UV-vis absorbance spectra of the FGO and FG in the wavelength between 199-800 nm.

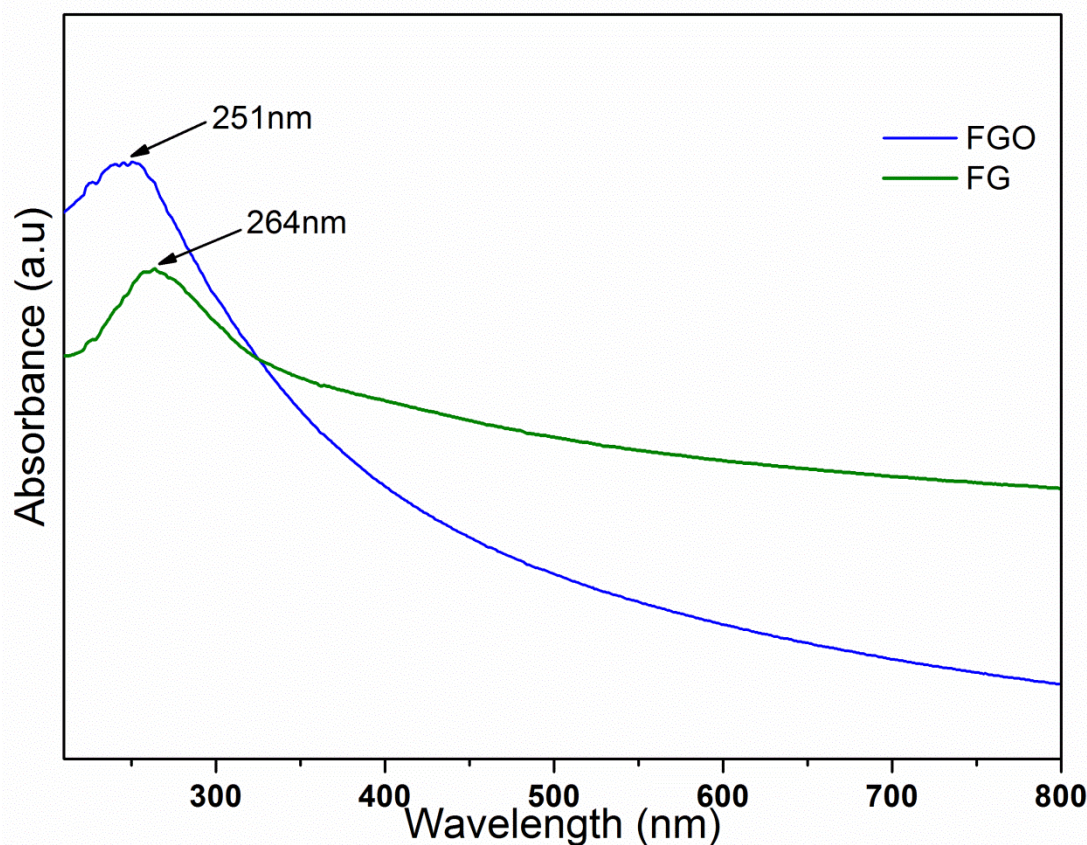


Figure 4.22: UV-Vis spectra of FGO (blue line) and FG (green line) after hydrothermal reduction.

It can be seen that the broad peak of FGO appeared at 251 nm indicates that exfoliation of graphite during oxidation process. It implies there are few stack of FGO layers in comparison with GO in the first part of synthesis. The absorbance peak of FG exhibits the red shift to 264 nm suggesting the excitation of π -plasmon of graphitic structure (X. Wang, et al., 2008). The red shift is an indication of the reduction process for FGO to FG which is completed.

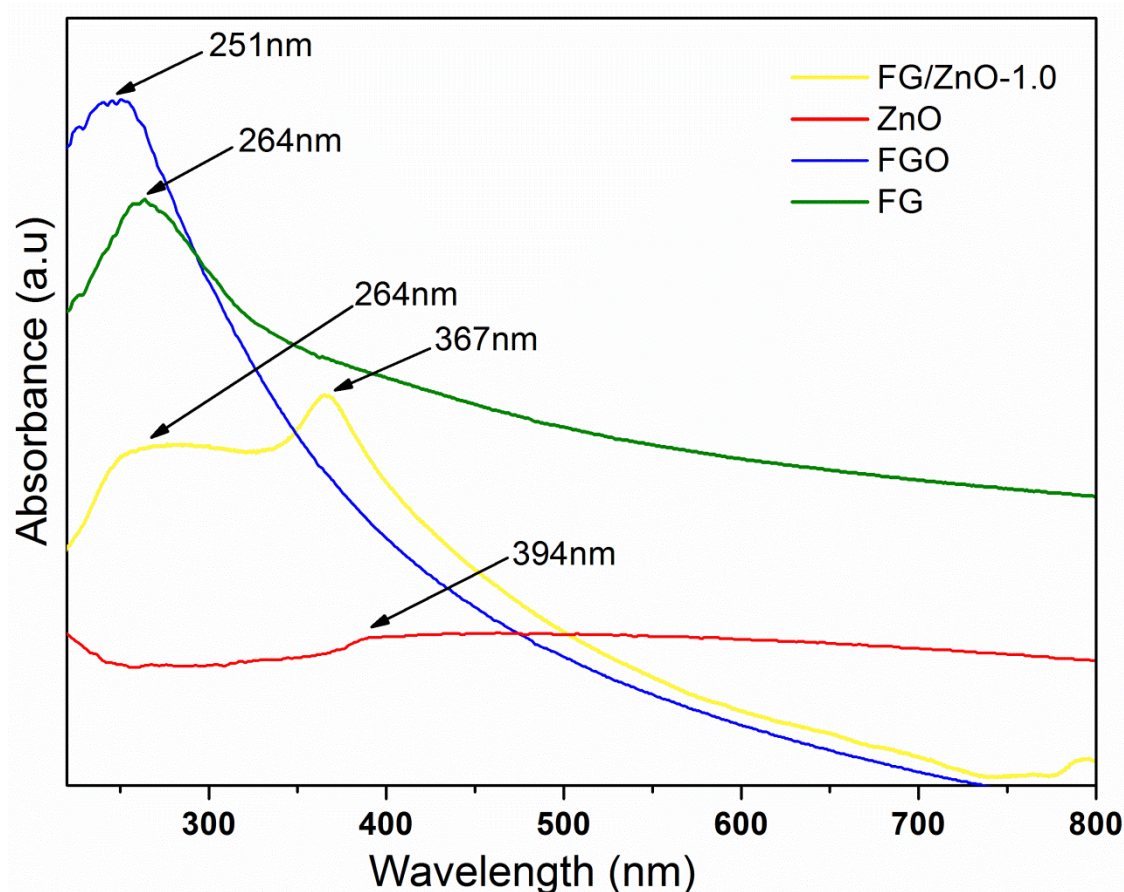


Figure 4.23: UV-visible spectra of FGO, FG, pure ZnO and FG/ZnO-1.0 nanocomposite.

The present of characteristic absorption peak at 394 nm indicates the presence of ZnO nanostructures as shown in Figure 4.23. The ZnO spectra displays no peak appeared at UV region, it suggests that the purity of ZnO is successfully synthesized. The UV-visible spectra for the composites show the appearance of two characteristic absorption peaks contributed from reduced FG and ZnO nanostructure. We observed the absorption peak at 264 nm which is consistent to the absorption peak of FG. However, the absorption peak that contributed from ZnO was shifted to 367 nm. This difference in the absorption spectra can be explained by their structure. It is possibly due to a stronger coupling between FG sheets and ZnO flower-like since it was distributed uniformly on the FG sheets (J. Wu, et al., 2010) as shown in FESEM results. Therefore, it leads to an obvious blue-shift in the absorption spectra.

4.3.2.9 Photoluminescence spectra

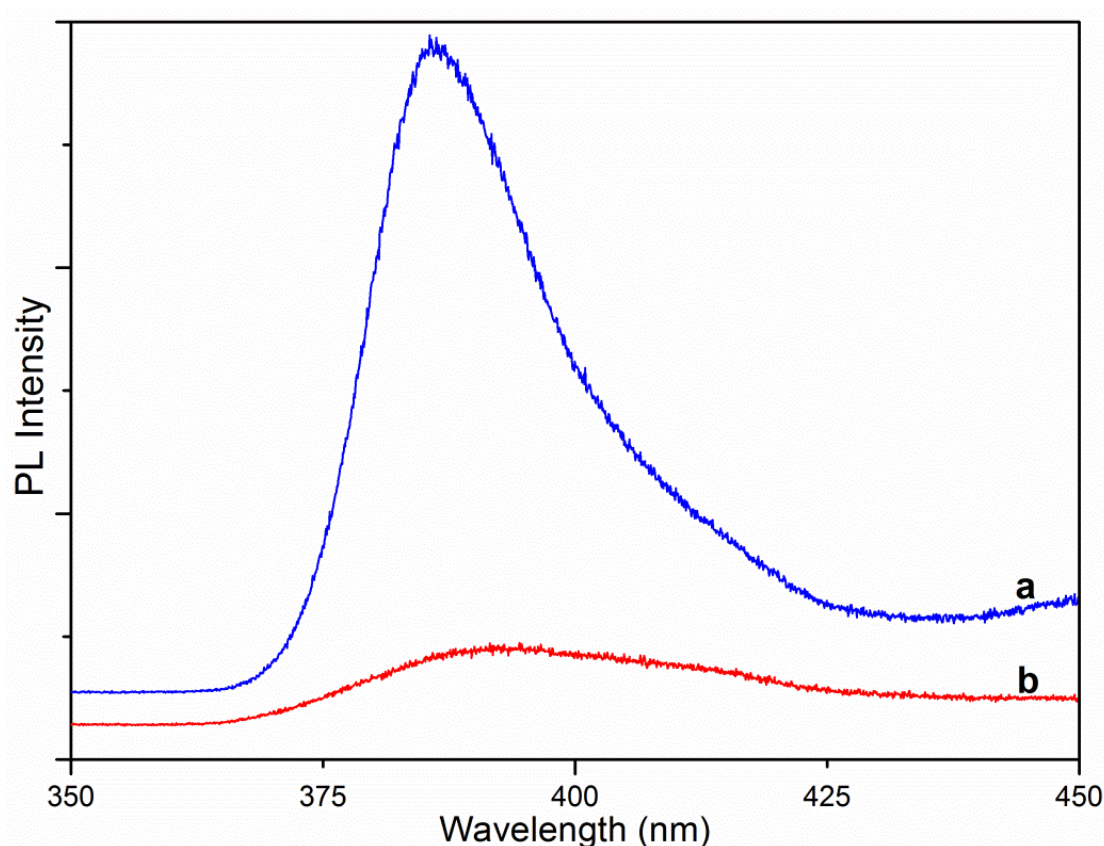


Figure 4.24: PL spectra of as-prepared samples under 325 nm UV irradiation: pure ZnO (a); FG/ZnO-1.0 flower-like nanocomposite (b).

Figure 4.24 shows the PL spectra for pure ZnO and nanocomposite. The samples in powder formed were dispersed in ethanol and dropped cast on the corning glass for the PL measurements. The photo emission of pure ZnO was appeared in ultraviolet region which centered at 385 nm as reported (X. Zhou, Shi, & Zhou). The emission intensity spectra of the nanocomposite decreases in comparison to pure ZnO due to the excitonic emission (Georgekutty, Seery, & Pillai, 2008). According to the literature (Jincheng Liu et al., 2010), the present of reduced FG increases the effectiveness of photoelectron transfer from ZnO to FG, thus impede the recombination of photo induced electrons and holes. Therefore, FG sheets reconstructed in aspect to upstanding the conductivity that served as an acceptor of photoemission from ZnO which gives a

better absorption capacity for catalytic system. Furthermore, this combination plays important factor in accepting the photo electron of ZnO to improve the degradation of MB dye (K. Zhou, et al., 2011).

4.3.3 Schematic for the synthesis of functionalized graphene oxide (FGO)

The stable and homogeneous aqueous suspension of FGO was prepared by introducing GO with highly hydrophilic silylating agent N-(trimethoxysilylpropyl) ethylenediamine triacetic acid sodium salt as shown in the Figure 4.25.

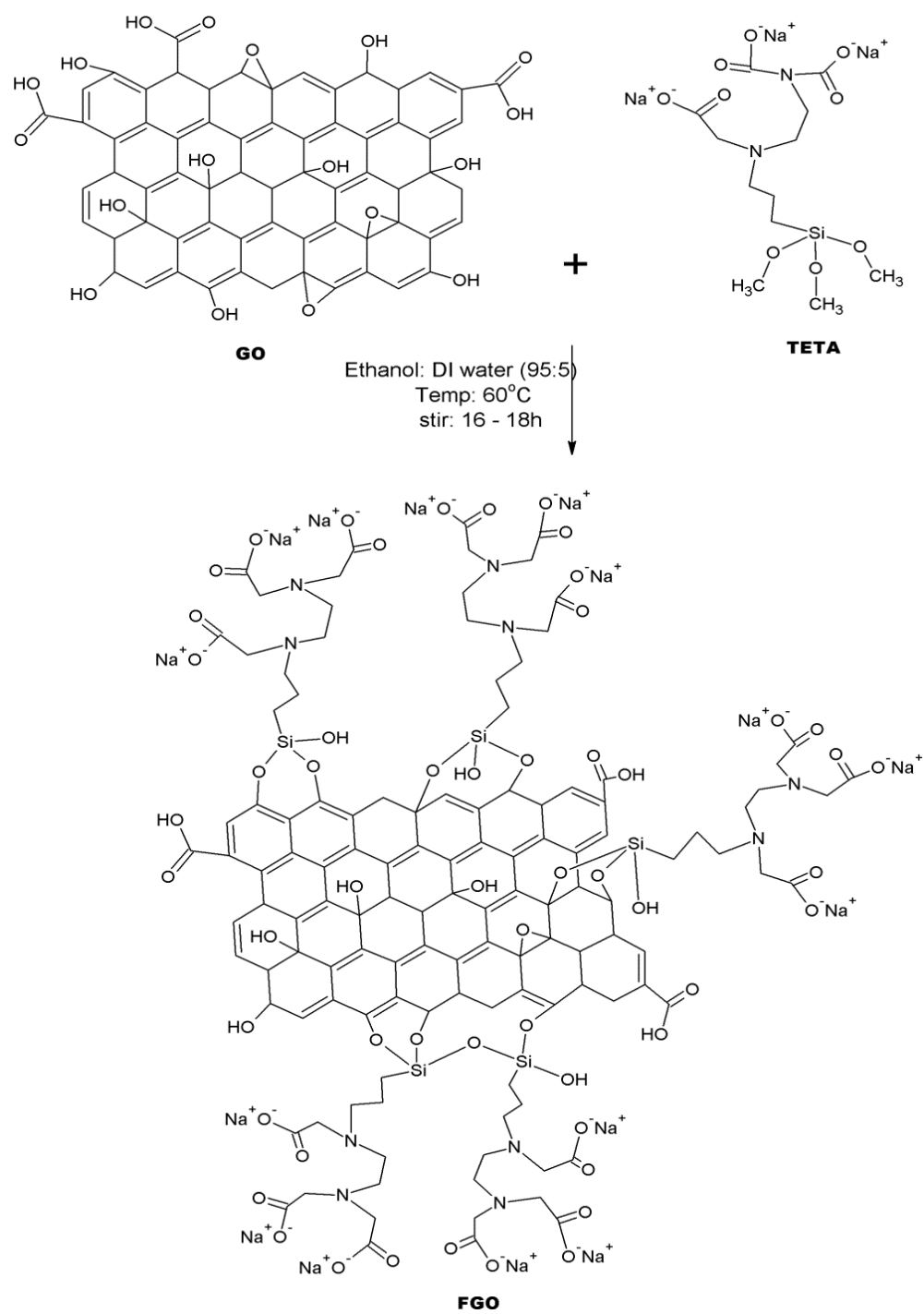


Figure 4.25: Schematic for the preparation of functionalized graphene oxide (FGO).

4.3.4 Schematic for the synthesis of nanoflower-like functionalized graphene/ZnO nanocomposite (FG/ZnO)

The general method for the preparation of the FG/ZnO nanocomposite is shown in Figure 4.26.

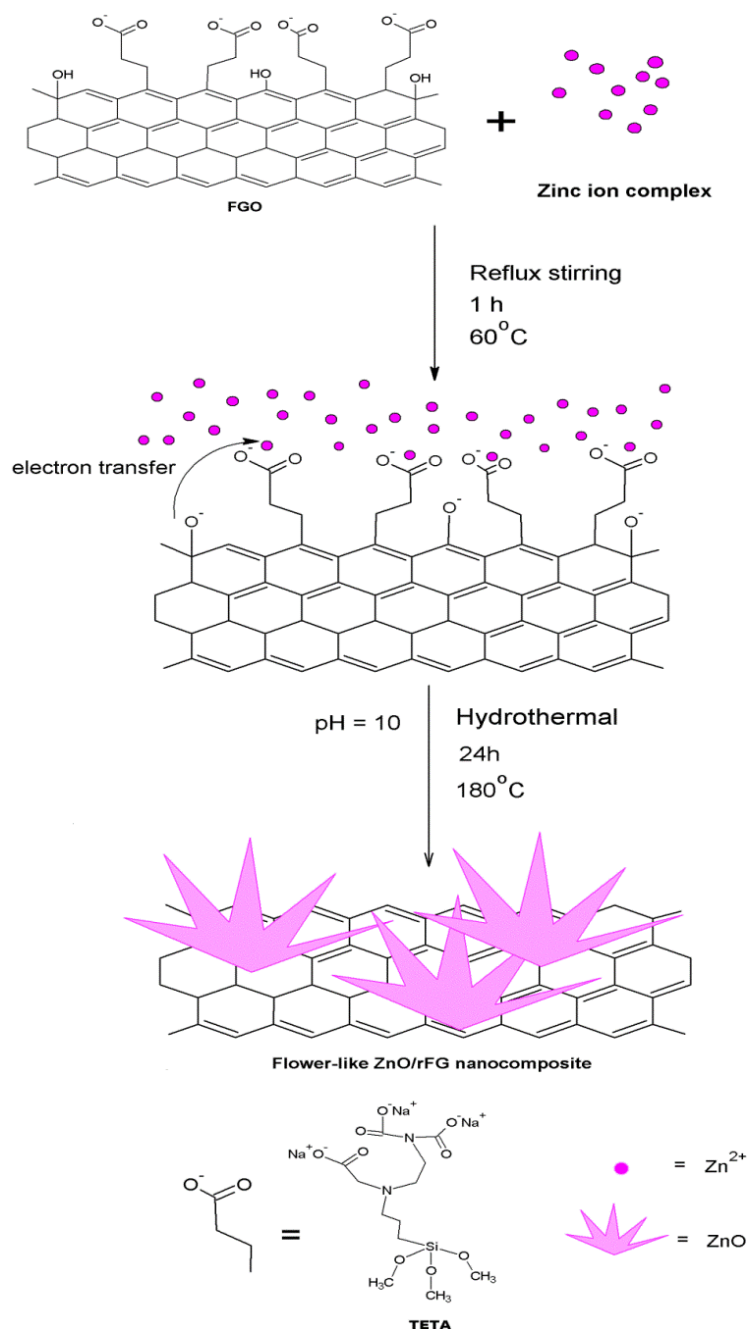


Figure 4.26: Schematic for the preparation of the nanoflower-like functionalized graphene/ZnO nanocomposite.

The surface of FGO contains unreacted hydroxyl group that attached to the hexagonal basal plane and large number of functionalized carboxylic group from N-(trimethoxysilylpropyl) ethylenediamine triacetic acid sodium salt. These carboxylic groups interact with the Zn ions and consequently form a complex through electrostatic interaction. At the same hydrothermal condition as previous synthesis, Zn ions are reduced on the surface of functionalized graphene oxide to form flower-like ZnO nanostructures. At the same time, the FGO sheet itself also reduced to reduce functionalized graphene sheets.

CHAPTER 5

CONCLUSION AND SUGGESTIONS FOR FUTURE RESEARCH

5.1 Conclusion

Graphene/ZnO nanocomposites were successfully synthesized via a simple hydrothermal technique. The nanorod-like graphene/ZnO nanocomposites were synthesized by using graphene oxide (GO) solution while the nanoflower-like graphene/ZnO nanocomposites were synthesized by using functionalized graphene oxide (FGO) solution as the starting material. This dissertation also includes the successful synthesized of ZnO and graphene by using the same technique.

The effect of concentrations of GO on as starting material on the formation of graphene/ZnO nanocomposites were studied via various characterization techniques. The structural and physical properties of graphene/ZnO nanocomposites were confirmed in the XRD analysis, which reflection peaks of ZnO are found to be consistent with the hexagonal ZnO reflection peaks (JCPDS file no. 01-089-0510). Besides, the optical result through UV-Visible absorption spectroscopy showed that the reduction GO after hydrothermal treatment. This was deduced by the right-shifting of the peak at 227 nm to 266 nm for the rod-like graphene/ZnO samples. The formation of the rod-like graphene/ZnO nanocomposites were confirmed by FESEM images strongly support the homogeneous combination of graphene/ZnO nanocomposites. The atomic crystallographic structure of graphene/ZnO nanocomposites were obtained by HRTEM. The atomic structure of rod-like ZnO exhibits lattice spacing of 0.248 nm can be indexed to as the (101) plane of hexagonal ZnO (Figure 4.3).

The nanoflower-like graphene/ZnO nanocomposites were successfully synthesized by using functionalized graphene oxide (FGO) solution. The structural properties of nanoflower-like graphene/ZnO nanocomposites were confirmed in the

XRD analysis, which all the diffraction peaks of nanocomposites are match with the standard data for hexagonal-structure ZnO reflection peaks (JCPDS file no. 01-089-0510). The complete reduction of FGO and exfoliation graphene layers was confirmed by appearance of a broad peak at 25.1° . This result is also supported by the UV-vis spectra. The optical result through UV-Visible absorption spectroscopy showed that the reduction FGO after hydrothermal treatment which deduced by the shifting peak at 227 nm to 264 nm. These represent the partial restoration of pi-conjugation network. Moreover, the reduction of FGO in the flower-like graphene/ZnO is displayed by the increasing the intensity ratio of the D peak to G peak in comparison to the FGO. This suggests the decrease in average size of sp^2 domain upon the reduction of FGO to FG. The FESEM images strongly support the homogeneous combination of graphene/ZnO nanocomposites, which are clearly exhibits the flower-like ZnO that distributed on the graphene sheets. Then, the TEM imaging confirmed the presents of ZnO and graphene in the nanocomposite. According to the TEM result for the graphene/ZnO-1.0 image exhibits a flower-like petal with a length of 467.76 nm and diameter of 126 nm (Figure 4.18d). The atomic crystallographic structure of graphene/ZnO nanocomposites were obtained by HRTEM. The atomic structure of the flower-like ZnO exhibits an interplanar distance of 0.281 nm that can be assigned to the (100) plane of the hexagonal ZnO (shown in Figure 4.19). Finally, the XPS results also confirmed the formation of nanocomposite by showing the nonoxygenated C-C are prominent due to the interaction of zinc ions with the carboxylic group from N-(trimethoxysilylpropyl) ethylenediamine triacetic acid sodium salt (shown in Figure 4.14).

It is found that the morphology and optical properties of the nanocomposites depend strongly on starting material. Different concentrations of starting material

contribute to the different characteristics of ZnO particles grown on the graphene sheets.

The composite with optimal parameter has uniform distribution.

5.2 Suggestion for future research

Most of the results presented in this dissertation including characterizations that and properties of nanocomposite that will be the target for further research. Further study will focus on only one class of substances, probably on the synthesis using FGO as initial material, and conduct a thorough research of their electric properties for potential application such as field-effect transistors (FETs), transparent electrodes, and ultrasensitive sensors.

REFERENCES

- Akhavan, O. (2011). Photocatalytic reduction of graphene oxides hybridized by ZnO nanoparticles in ethanol. *Carbon*, 49(1), 11-18.
- Basic principle of transmission electron microscope. from http://www.hk-phy.org/atomic_world/tem/tem02_e.html
- Berger, C., Song, Z., Li, T., Li, X., Ogbazghi, A. Y., Feng, R., et al. (2004). Ultrathin Epitaxial Graphite: 2D Electron Gas Properties and a Route toward Graphene-based Nanoelectronics. *The Journal of Physical Chemistry B*, 108(52), 19912-19916.
- Berger, C., Song, Z., Li, X., Wu, X., Brown, N., Naud, C., et al. (2006). Electronic Confinement and Coherence in Patterned Epitaxial Graphene. *Science*, 312(5777), 1191-1196.
- Billoski, T. V. (1992). *Introduction to Paleontology 2* (6th ed.). New York: Institutional Press.
- Bvcrist. (10 June 2010). This schematic depicts the process known as the "Photo-electric Effect" as it pertains to XPS., from http://upload.wikimedia.org/wikipedia/commons/thumb/0/07/XPS_PHYSICS.png/350px-XPS_PHYSICS.png
- Byrappa, K., & Yoshimura, M. (2001). 4 - Physical Chemistry of Hydrothermal Growth of Crystals *Handbook of Hydrothermal Technology* (pp. 161-197). Norwich, NY: William Andrew Publishing.
- Castro Neto, A. H., F. Guinea, and N. M. R. Peres,. (2006a). *Phys. World*, 19, 33.
- Chen, S., Zhu, J., Wu, X., Han, Q., & Wang, X. (2010). Graphene Oxide-MnO₂ Nanocomposites for Supercapacitors. *ACS Nano*, 4(5), 2822-2830.
- Chen, Y.-L., Hu, Z.-A., Chang, Y.-Q., Wang, H.-W., Zhang, Z.-Y., Yang, Y.-Y., et al. (2011). Zinc Oxide/Reduced Graphene Oxide Composites and Electrochemical Capacitance Enhanced by Homogeneous Incorporation of Reduced Graphene Oxide Sheets in Zinc Oxide Matrix. *The Journal of Physical Chemistry C*, 115(5), 2563-2571.
- Clark, J. (2006). A double beam UV-visible absorption spectrometer from <http://www.chemguide.co.uk/analysis/uvvisible/spectrometer.html>
- D. Li, M. B. M., S. Gilje, R. B. Kaner, G. G. Wallace. (2008). Processable aqueous dispersions of graphene nanosheets. *Nature Nanotechnology*, 3, 101-105.
- Dato, A., Radmilovic, V., Lee, Z., Phillips, J., & Frenklach, M. (2008). Substrate-Free Gas-Phase Synthesis of Graphene Sheets. *Nano Letters*, 8(7), 2012-2016.
- de Heer, W. A., Berger, C., Wu, X., First, P. N., Conrad, E. H., Li, X., et al. (2007). Epitaxial graphene. *Solid State Communications*, 143(1-2), 92-100.
- Everett, D. H. (1988). Basic Principles of Colloid Science. *The Royal Society of Chemistry, London*.
- Geim, A. K., & Novoselov, K. S. (2007). The rise of graphene. [10.1038/nmat1849]. *Nat Mater*, 6(3), 183-191.
- Georgekutty, R., Seery, M. K., & Pillai, S. C. (2008). A Highly Efficient Ag-ZnO Photocatalyst: Synthesis, Properties, and Mechanism. *The Journal of Physical Chemistry C*, 112(35), 13563-13570.
- Gilje, S., Han, S., Wang, M., Wang, K. L., & Kaner, R. B. (2007). A Chemical Route to Graphene for Device Applications. *Nano Letters*, 7(11), 3394-3398.
- Graf, D., Molitor, F., Ensslin, K., Stampfer, C., Jungen, A., Hierold, C., et al. (2007). Spatially Resolved Raman Spectroscopy of Single- and Few-Layer Graphene. *Nano Letters*, 7(2), 238-242.

- Guo, Y., Wang, H., He, C., Qiu, L., & Cao, X. (2009). Uniform Carbon-Coated ZnO Nanorods: Microwave-Assisted Preparation, Cytotoxicity, and Photocatalytic Activity. *Langmuir*, 25(8), 4678-4684.
- Guo, Z. P., Zhao, Z. W., Liu, H. K., & Dou, S. X. (2005). Electrochemical lithiation and de-lithiation of MWNT-. Sn/SnNi nanocomposites. *Carbon*, 43, 1392.
- Han, S. Y., Kim, I. Y., Jo, K. Y., & Hwang, S.-J. (2012). Solvothermal-Assisted Hybridization between Reduced Graphene Oxide and Lithium Metal Oxides: A Facile Route to Graphene-Based Composite Materials. *The Journal of Physical Chemistry C*, 116(13), 7269-7279.
- Hassan, H. M. A., Abdelsayed, V., Khder, A. E. R. S., AbouZeid, K. M., Turner, J., El-Shall, M. S., et al. (2009). Microwave synthesis of graphene sheets supporting metal nanocrystals in aqueous and organic media. *Journal of Materials Chemistry*, 19(23), 3832-3837.
- Huang, N. M., Lim, H. N., Chia, C. H., Yarmo, M. A., & Muhamad, M. R. (2011). Simple room-temperature preparation of high-yield large-area graphene oxide. *International Journal of Nanomedicine*, 2011:6, 3443 - 3448.
- Kroto, H. W., Heath, J. R., O'Brien, S. C., Curl, R. F., & Smalley, R. E. (1985). C60: Buckminsterfullerene. [10.1038/318162a0]. *Nature*, 318(6042), 162-163.
- Kudin, K. N., Ozbas, B., Schniepp, H. C., Prud'homme, R. K., Aksay, I. A., & Car, R. (2007). Raman Spectra of Graphite Oxide and Functionalized Graphene Sheets. *Nano Letters*, 8(1), 36-41.
- Kumar, A. J., H.; Pasricha, R.; Mandale, A. B.; Sastry, M., (2003). Phase transfer of silver nanoparticles from aqueous to organic solutions using fatty amine molecules. *Journal of Colloid and Interface Science*(264), 396-401.
- Li, B., & Cao, H. (2011). ZnO@graphene composite with enhanced performance for the removal of dye from water. *Journal of Materials Chemistry*, 21(10), 3346-3349.
- Li, X., Wang, X., Zhang, L., Lee, S., & Dai, H. (2008). Chemically Derived, Ultrasmooth Graphene Nanoribbon Semiconductors. *Science*, 319(5867), 1229-1232.
- Liu, J., Bai, H., Wang, Y., Liu, Z., Zhang, X., & Sun, D. D. (2010). Self-Assembling TiO₂ Nanorods on Large Graphene Oxide Sheets at a Two-Phase Interface and Their Anti-Recombination in Photocatalytic Applications. *Advanced Functional Materials*, 20(23), 4175-4181.
- Liu, J., Li, Y., Ding, R., Jiang, J., Hu, Y., Ji, X., et al. (2009). Carbon/ZnO Nanorod Array Electrode with Significantly Improved Lithium Storage Capability. *The Journal of Physical Chemistry C*, 113(13), 5336-5339.
- Liu, X., Ly, J., Han, S., Zhang, D., Requicha, A., Thompson, M. E., et al. (2005). Synthesis and electronic properties of individual single-walled carbon nanotube/polypyrrole composite nanocables. *advanced Materials*, 17, 2727-3732.
- Lv, H., Sang, D., Li, H., Du, X., Li, D., & Zou, G. (2010). Thermal Evaporation Synthesis and Properties of ZnO Nano/Microstructures Using Carbon Group Elements as the Reducing Agents. *Nanoscale Research Letters*, 5(3), 620-624.
- Material Surface Analysis with X-Ray Photoelectron Spectroscopy (XPS). (May 10, 2011). from <http://subato.blogspot.com/2011/05/material-surface-analysis-with-x-ray.html>
- Mofor, A. C., Bakin, A. S., Elshaer, A., Fuhrmann, D., Bertram, F., Hangleiter, A., et al. (2007). Vapour Transport Growth of ZnO Nanorods. *Appl. Phys. A*, 88(1), 17-20.
- Molecular Fluorescence Spectroscopy. 2013, from <http://www.chemistry.adelaide.edu.au/external/soc-rel/content/mol-fluo.htm>

- Moxfyre. (18 September 2009). Molecular energy levels and Raman effect. from <http://dictionary.sensagent.com/raman+spectroscopy/en-en/>
- Novoselov, K. S., Geim, A. K., Morozov, S. V., Jiang, D., Zhang, Y., Dubonos, S. V., et al. (2004). Electric Field Effect in Atomically Thin Carbon Films. *Science*, 306(5696), 666-669.
- Osawa, E., Kroto, H. W., Fowler, P. W., & Wasserman, E. (1993). The Evolution of the Football Structure for the C₆₀ Molecule: A Retrospective [and Discussion]. *Philosophical Transactions of the Royal Society of London. Series A: Physical and Engineering Sciences*, 343(1667), 1-8.
- Park, J., Eom, J., & Kwon, H. (2009). *Electrochem. Commun.*, 11, 596.
- Park, S., & Ruoff, R. S. (2009). Chemical methods for the production of graphenes. *Nature Nanotechnology*, 4, 217 - 224.
- Pimenta, M. A., Dresselhaus, G., Dresselhaus, M. S., Cancado, L. G., Jorio, A., & Saito, R. (2007). Studying disorder in graphite-based systems by Raman spectroscopy. *Physical Chemistry Chemical Physics*, 9(11), 1276-1290.
- Potts, J. R., Dreyer, D. R., Bielawski, C. W., & Ruoff, R. S. (2011). Graphene-based polymer nanocomposites. *Polymer*, 52(1), 5-25.
- Rao, A. B., et al. (2009). Royal Society of Chemistry.
- Riman, R. E., Suchanek, W. L., & Lencka, M. M. (2002). Hydrothermal crystallization of ceramics. *Annales de Chimie Science des Matériaux*, 27(6), 15-36.
- Roy, R. (1994). Accelerating the Kinetics of Low-Temperature Inorganic Syntheses. *Journal of Solid State Chemistry*, 111(1), 11-17.
- Skoog, H., and Nieman. Principles of Instrumental Analysis. from http://radchem.nevada.edu/classes/chem455/lecture_22_thermal_methods.htm
- Stankovich, S., Dikin, D. A., Piner, R. D., Kohlhaas, K. A., Kleinhammes, A., Jia, Y., et al. (2007). Synthesis of graphene-based nanosheets via chemical reduction of exfoliated graphite oxide. *Carbon*, 45(7), 1558-1565.
- Sunagawa, I., Tsukamoto, K., Maiwa, K., & Onuma, K. (1995). Growth and perfection of crystals from aqueous solution: Case studies on barium nitrate and K-alum. *Progress in Crystal Growth and Characterization of Materials*, 30(2-3), 153-190.
- Technology Methods. (2011). from <http://laser-detect.com/technology-methods/>
- Vázquez de Parga, A. L., Calleja, F., Borca, B., Passeggi, M. C. G., Jr., Hinarejos, J. J., Guinea, F., et al. (2008). Periodically Rippled Graphene: Growth and Spatially Resolved Electronic Structure. *Physical Review Letters*, 100(5), 056807.
- Wang, D. H., Choi, D. W., Li, J., Yang, Z. G., Nie, Z. M., Kou, R., et al. (2009). Self-assembled TiO₂-graphene Hybrid Nanostructures for Enhanced Li-ion Insertion. *ACS Nano*, 3(4), 907-914.
- Wang, G. X., Ahn, J. H., Lindsay, M. J., Sun, L., Bradhurst, D. H., Dou, S. X., et al. (2001). Physical and electrochemical characterisation of LiNi_{0.8}Co_{0.2}O₂ thin-film electrodes deposited by laser ablation. *Journal of Power Sources*, 298-302.
- Wang, X., Zhi, L., Tsao, N., Tomović, Ž., Li, J., & Müllen, K. (2008). Transparent Carbon Films as Electrodes in Organic Solar Cells. *Angewandte Chemie International Edition*, 47(16), 2990-2992.
- Watcharotone, S., Dikin, D. A., Stankovich, S., Piner, R., Jung, I., Dommett, G. H. B., et al. (2007). Graphene-Silica Composite Thin Films as Transparent Conductors. *Nano Letters*, 7(7), 1888-1892.
- Williams, G., & Kamat, P. V. (2009). Graphene-Semiconductor Nanocomposites: Excited-State Interactions between ZnO Nanoparticles and Graphene Oxide†. *Langmuir*, 25(24), 13869-13873.

- Wissler, M. (2006). Graphite and carbon powders for electrochemical applications. *J. Power Sources*, 156, 142–150.
- Wu, J., Shen, X., Jiang, L., Wang, K., & Chen, K. (2010). Solvothermal synthesis and characterization of sandwich-like graphene/ZnO nanocomposites. *Applied Surface Science*, 256(9), 2826-2830.
- Wu, Z.-S., Ren, W., Gao, L., Liu, B., Zhao, J., & Cheng, H.-M. (2010). Efficient synthesis of graphene nanoribbons sonochemically cut from graphene sheets. *Nano Research*, 3(1), 16-22.
- X-ray Diffraction. 2013, from <http://www.gnr.it/images/xrd.gif>
- Xiang, Q., Yu, J., & Jaroniec, M. (2011). Enhanced photocatalytic H₂-production activity of graphene-modified titania nanosheets. *Nanoscale*, 3(9), 3670-3678.
- Yan, J., Fan, Z., Wei, T., Qian, W., Zhang, M., & Wei, F. (2010). Fast and reversible surface redox reaction of graphene–MnO₂ composites as supercapacitor electrodes. *Carbon*, 48(13), 3825-3833.
- Yoshimura, M., Suchanek, W. L., & Byrappa, K. (2000). Soft Solution Processing: A Strategy for One-Step Processing of Advanced Inorganic Materials. *MRS Bulletin*, 25(09), 17-25.
- Yousefi, R., Muhamad, M. R., & Zak, A. K. (2011). The effect of source temperature on morphological and optical properties of ZnO nanowires grown using a modified thermal evaporation set-up. *Current Applied Physics*, 11(3), 767-770.
- Zhang, J., Xiong, Z., & Zhao, X. S. (2011). Graphene-metal-oxide composites for the degradation of dyes under visible light irradiation. *Journal of Materials Chemistry*, 21(11), 3634-3640.
- Zhang, S., Shao, Y., Liao, H., Engelhard, M. H., Yin, G., & Lin, Y. (2011). Polyelectrolyte-Induced Reduction of Exfoliated Graphite Oxide: A Facile Route to Synthesis of Soluble Graphene Nanosheets. *ACS Nano*, 5(3), 1785-1791.
- Zhou, K., Zhu, Y., Yang, X., Jiang, X., & Li, C. (2011). Preparation of graphene-TiO₂ composites with enhanced photocatalytic activity. *New Journal of Chemistry*, 35(2), 353-359.
- Zhou, X., Shi, T., & Zhou, H. Hydrothermal preparation of ZnO-reduced graphene oxide hybrid with high performance in photocatalytic degradation. *Applied Surface Science*(0).